A Time-Resolved Photophysical Study of Hybrid Organic-Inorganic Perovskite Photovoltaic Materials

THÈSE N^O 7713 (2017)

PRÉSENTÉE LE 1 SEPTEMBRE 2017
À LA FACULTÉ DES SCIENCES DE BASE
GROUPE DE DYNAMIQUE PHOTOCHIMIQUE
PROGRAMME DOCTORAL EN CHIMIE ET GÉNIE CHIMIQUE

ÉCOLE POLYTECHNIQUE FÉDÉRALE DE LAUSANNE

POUR L'OBTENTION DU GRADE DE DOCTEUR ÈS SCIENCES

PAR

Arun Aby PARAECATTIL

acceptée sur proposition du jury:

Prof. L. Helm, président du jury
Prof. J.-E. Moser, directeur de thèse
Dr J. Helbing, rapporteur
Dr C. Ponseca, rapporteur
Prof. A. Hagfeldt, rapporteur

(EPFL

ÉCOLE POLYTECHNIQUE
FÉDÉRALE DE LAUSANNE

Suisse
2017

Abstract

The search for new photovoltaic materials has been driven by the combined need to exploit sources of energy that are clean and sustainable, while simultaneously doing it in a cost effective manner. In this light, hybrid organic-inorganic perovskites have recently emerged as an extremely promising photonic material, and their application as a functional photovoltaic layer has resulted in power conversion efficiencies that rival long established silicon based technologies. Rapid progress in device efficiencies have occurred over the last years (22.1% being the current record). However, the simultaneous growth in basic studies of the material have not resulted in a conclusive understanding of the fundamental process that occur subsequent to photoexcitation. Hence, there is a pressing need to identify the pathways that currently limit device performance and provide direction for future work in materials and device engineering. Towards this goal, we investigate two perovskite compositions ($CH_3NH_3PbI_3$ and $(FAPbI_3)_{0.85}(MAPbBr_3)_{0.15}$) using time-resolved THz and electroabsorption spectroscopic techniques.

Chapter 1 and **2** provide a general introduction into the investigated system and the experimental techniques that have been used. In **chapter 3**, we detail time-resolved THz measurements and report on experimental evidence for carrier recombination through an indirect process, as well as a direct recombination pathway that is present at higher carrier densities. We calculate temperature dependent carrier mobilities (at THz frequencies) and bimolecular recombination constants, through which we identify phonon scattering as the

primary limiting mechanism for carrier transport, and temperature dependent bimolecular recombination. Analysis of the complex photoconductivity spectra using the Drude-Smith model revealed a large difference in carrier scattering between the two perovskite films that could be attributed to the significantly different morphologies.

In **chapter 4** we apply time-resolved electroabsorption spectroscopy (TREAS) to insulated $CH_3NH_3PbI_3$ layers and investigate the macroscopic carrier transport dynamics under an externally applied electric field. Transport within the 40 nm perovskite grain was discovered to be diminished by a factor ≈ 2 relative to the high frequency mobility obtained through THz spectroscopy. The averaged carrier mobility across the 280 nm film thickness was reduced by a factor ≈ 4, due to the presence of grain boundaries and defects. Preliminary investigations also identified spectral signatures associated with carrier accumulation at the perovskite interface and delayed extraction at the contacts.

Chapter 5 deals with complete solar cells formed using $(FAPbI_3)_{0.85}(MAPbBr_3)_{0.15}$ as the active layer and we report the first application of the TREAS technique to complete perovskite devices. Our results reveal that the improved morphology of the carrier results in film averaged mobilities that are near the intrinsic values obtained using THz spectroscopy. Analysis of transient absorption spectra revealed an electroabsorption signature, which can be correlated with the disassociation of a transient excitonic species to form free charge carriers.

Keywords: Ultrafast spectroscopy, THz spectroscopy, time-resolved electroabsorption spectroscopy, perovskite, photovoltaics

Résumé

La recherche de nouveaux matériaux photovoltaïques a été poussée par le besoin d'exploiter de nouvelles sources d'énergies propres et durables d'une manière rentable. Dans ce contexte, les pérovskites organométalliques hybrides ont récemment émergé en tant que matériel photonique très prometteur. Leur application comme couche photovoltaïque fonctionnelle a résulté en une efficacité des systèmes qui rivalisent avec les technologies basées sur la silicium utilisées jusqu'à présent. Un progrès rapide du rendement des systèmes a été observé ces dernières années (avec un record actuel à 22,1%). Cependant l'évolution simultanée des connaissances de base sur les matériaux n'a pas donné lieu à des avancées majeures dans la compréhension du processus fondamental qui suit la photo-excitation. Il y a par conséquent un grand besoin d'identifier les processus qui limitent la performance des systèmes et de trouver de nouvelles pistes pour l'ingénierie de matériaux et de systèmes plus performants.

Les chapitres 1 et 2 présentent une introduction générale du système étudié ainsi que des techniques expérimentales employées. Dans le chapitre 3 les mesures THz résolues en temps sont détaillées avant d'être appliquées à des résultats expérimentaux pourtant sur la recombinaison de porteurs de charge par un processus indirect puis sur une voie de recombinaison directe qui est présente à des fluences plus élevées. La mobilité des porteurs dépendante de la température (aux fréquences THz) et les constantes de recombinaison bi-moléculaire ont été calculées ; ce qui a permis dans un premier temps d'identifier la diffusion par les phonons comme le principal facteur limitant le transports des charges, puis dans un second temps de déterminer que la recombinaison bi-moléculaire dépendante de la température est contrôlée par la mobilité relative des porteurs de charge. L'analyse de spectres complexes de photoconductivité via le modèle

Drude-Smith a révélé d'importantes disparités dans la dispersion des porteurs entre les deux films pérovskites. Ces disparités ont pu être attribuées aux différences significatives de morphologie.

Au chapitre 4, la spectroscopie d'électro-absorption résolue en temps (TREAS) a été appliquée à des couches isolées de $CH_3NH_3PbI_3$ puis la dynamique de transport à longue distance de porteurs de charge sous l'effet d'un champ électrique a été étudiée. Il a été découvert que le transport dans les grains de pérovskite de 40 nm était diminué d'un facteur ≈ 2 par rapport à la mobilité à haute fréquence obtenue par spectroscopie THz (qui est proche des valeurs intrinsèques du matériau). La mobilité moyenne sur toute l'épaisseur du film de 280 nm a été réduite d'un facteur ≈ 4 en raison de la présence de piège aux joints de grains. Des recherches préliminaires ont également permis d'identifier des signatures spectrales associées à l'accumulation de porteurs à l'interface pérovskite et à une extraction retardée aux zones de contact. Enfin, le chapitre 5 traite des cellules solaires complètes formées en utilisant $(FAPbI_3)_{0,85}$ $(MAPbBr_3)_{0,15}$ comme couche active ; l'application de la technique TREAS pour étudier ces systèmes de pérovskite est présentée. Les résultats révèlent que la morphologie ainsi améliorée du film résulte en des mobilités moyennes des charges proches des valeurs intrinsèques obtenues en utilisant la spectroscopie THz. L'analyse des spectres d'absorption transitoire a révélé une signature d'électro-absorption qui peut être corrélée avec la dissociation d'une espèce excitonique transitoire.

Keywords: Spectroscopie ultrarapide, THz spectroscopie, spectroscopie d'electroabsorption résolue dans le temps, photovoltaïque, perovskite

Contents

Contents

1. Introduction

Humanity's ability to efficiently harness sources of energy over the last centuries has been a cornerstone in the progress of industries that now touch all areas of our lives, such as agriculture, transportation, communications, etc. However, over the last decades our individual energy demands have grown rapidly and in tandem with an ever rising global population. Our growing needs have occurred in parallel with the realization of the substantial health and climatic risks associated with the use of fossil fuels as our primary source of energy. In this light, one of the most pressing issues of our time is the implementation of sources of energy, that are not just clean and sustainable, but also capable of meeting our needs without excessive compromise. This paves the way for renewable energy sources (solar, wind, hydroelectric, etc.) that provide avenues to meet our demands in a manner that is both clean and sustainable. Among the options, solar energy harvested from the sun to produce electricity is an especially promising choice given the magnitude of solar radiation that strikes the earth every day. The photovoltaic effect discovered by A.E Becquerel[1] in 1839 serves as the basis for modern photovoltaic cells that directly convert solar radiation to electricity. The current commercial market for these photovoltaic cells are dominated by silicon based cells, which provide benefits of fairly high device efficiencies and longevity. The drawbacks of crystalline silicon as the active photovoltaic material are the requirements for a high purity material, which involves processing at high vacuum and elevated temperatures. This takes a considerable

amount of energy to produce, in addition to the financial costs associated with the demanding processing conditions. So, despite the dominance of silicon in the market, there are significant research efforts focused on developing new materials and device architectures that can compete with silicon in terms of efficiency and reliability, while reducing the energetic and financial costs associated with the fabrication of devices. Towards this goal, a wide range of alternative device architectures and functional materials that have significantly less challenging processing conditions have been studied.

One such architecture is the dye-sensitized solar cells (DSSCs), where a monolayer of dye molecules with a high extinction coefficient is adsorbed on a high surface area nanocrystalline TiO_2 scaffold. The dye act as the light absorber and electron injection into the TiO_2 allows for carrier separation. The electron is subsequently transported through the TiO_2 semiconductor to the extraction electrode. Another alternative is the thin film photovoltaic architecture that uses direct bandgap materials with high absorption coefficients, that consequently require significantly less material to achieve similar absorbance as silicon (as the latter is characterized by an indirect band gap). This thesis investigates hybrid organic-inorganic perovskites, a class of solution-processable semiconductor materials that have recently been demonstrated as an exceptional functional material for photovoltaic applications.[2-4] A more detailed description of perovskites and their application in photovoltaic devices will be provided over the course of chapter 1.

1.1 Semiconductors

Solids are characterized by a continuum of states formed by a large density of closely spaced electronic energy levels, rather than the discreet levels that characterize atoms and molecules. An energy gap (E_g) separates the lowest, unoccupied band of allowed states (referred to as the conduction band (CB)) and the highest, completely occupied band (called the valence band (VB)). The gap between energy levels is possessed by both semiconductors and insulators, with the possibility to make semiconductors conductive under certain conditions. The Fermi level (E_F) in the band picture (Figure 1.1) defines energy level for which there is a 50% probability of electronic occupation at a certain temperature (T), the probability distribution of a state being occupied is given by the Fermi-Dirac function in Eq. 1.1.
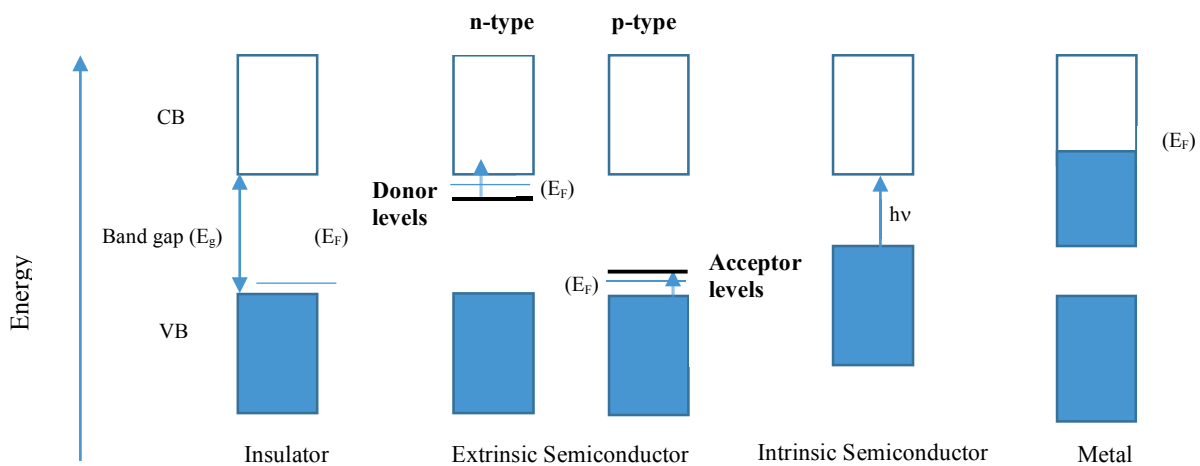
Figure 1.1 – Illustration of the band gap between the valence and conduction bands of semiconductors

$$f(E) = \frac{1}{1 + e^{(E - E_F)/kT}} \qquad \textbf{Eq. 1.1}$$

In intrinsic semiconductors, the Fermi energy lies in the middle of the forbidden bandgap. This implies that the VB is completely occupied and with no easily accessible states for conduction. In this case, with the occupation of states in the VB, the first empty states for the electron lie in the CB which is separated by a band gap of E_g. Hence, in the presence of an external electric field, acceleration of electrons is not possible, inhibiting the flow of charge carriers across the material.[5] Photoexcitation with a photon energy hv $\geq E_g$, can promote electrons from the VB to the CB. This results in the formation of partially filled bands that allows the crystal to become electrically conductive, through the motion of electrons in the CB or holes (electron vacancies) in the VB. In extrinsic semiconductors partial filling of the bands is accomplished by doping. They can either be n-doped where electrons are added to the CB due to donor impurities or p-doped where acceptor impurities result in the formation of holes in the VB. The density of charge carriers in semiconductors are generally small. In metals, the Fermi levels lie in the conduction band and electrons can access empty states that are closely spaced energetically, allowing them to become conductive.

Chapter 1
___

Origin of the Bandgap

We begin with the free electron model, although it does not explain the existence of a band gap, it does provide insight into the thermal and electrical conductivities of metals and its extension serves as the basis for a description of the band structure in a crystal. In the free electron picture, electrons are considered to be completely detached from their ionic cores and their only interaction involves scattering off these ionic cores. The electron energy is purely kinetic and given by:

$$E = \frac{p^2}{2m_0} \quad \text{and} \quad E = \frac{h^2 k^2}{2m_0} \qquad \textbf{Eq. 1.2}$$

Where m_0 is the rest mass of a free electron and p is electron momentum, with p = h / λ_e = ℏk, λ_e being the de Broglie wavelength of the electron and k the wave vector of the electron.

In order to explain the formation of the band gap we use an extension to the previous model, this extension is called the nearly free electron model. It takes into account the existence of a periodic lattice potential formed by the repeating units of atoms and allows for the existence of a band gap.[6] The potential originates from positively charged ion cores in a structure, that creates a periodic electromagnetic field. Free electrons in the form a traveling plane wave experience this field as a periodic perturbation. Bragg reflections of the electron wave by lattice planes formed in the periodic crystal structure, interfere in a constructive or destructive manner with the forward traveling wave. When the separation distance of the planes is comparable to the electron wavelength, the reflected waves interfere destructively with the forward travelling wave.[7] These

5

p, probability density
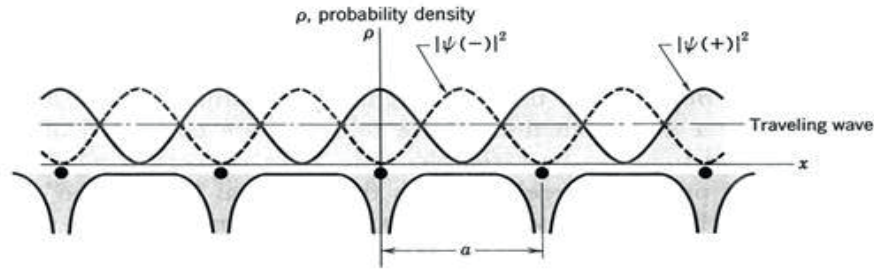
Figure 1.2 – Distribution of the probability density, (p), of the conduction band electrons in the lattice for the standing wave, $|\Psi(-)|$ and $|\Psi(+)|$ and the travelling wave. In the wavefunction $|\Psi(+)|$ electronic charge is preferentially distributed at the positive ion core and the average potential is lower relative to the average potential of the travelling wave. The wavefunction $|\Psi(-)|$ piles up electronic charge between the ions and removes it from the ion cores; thereby raising the average potential relative to that seen by the travelling wave. Figure reproduced from ref 6.

interferences give rise to standing waves which have their electron density peaking at different regions of the periodic lattice (Figure 1.2), and the difference between the potential energies of the standing waves and the traveling electron wave gives rise to the observed band gap.[5-7] The description of the band structure of a semiconductor is provided by the Bloch's theorem.

$$\psi_k(r) = u_k(r)\, e^{i\vec{k}\cdot\vec{r}} \qquad \textbf{Eq. 1.3}$$

Where the Bloch wave is determined by the product of the wavefunction of the electron $\exp^{(ik\cdot r)}$ and a function with the periodicity of the crystal lattice $u_k(r)$.

The E–k diagram near the VBM and CBM are shown in Figure 1.3, which displays a simplified view in one-dimension, for small k the bands can be considered parabolic. The band dispersions of the valence band, $E_{vb}(k)$, and conduction band, $E_{cb}(k)$, are given by Eq. 1.4.
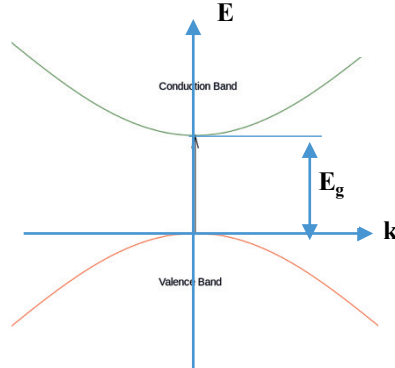
Figure 1.3 – Simplified view of the band edge structure of a direct gap semiconductor. k represents the projection of the $\vec{k}$ vector on the x axis. It is proportional to the carrier momentum p.

$$E_{VB}(k) = -(\frac{\hbar}{2m_h^*})k^2 \quad \textbf{and} \quad E_{CB}(k) = E_g + (\frac{\hbar^2}{2m_e^*})k^2 \quad \textbf{Eq. 1.4}$$

Where m* refers to the effective mass of electrons and holes in the CB and VB respectively.

Effective Mass

A characteristic of semiconductor crystals is the effective mass (m*) of electrons and holes in the bands they occupy. It serves to describe the response of the carriers' crystal momentum, $p = m^*v = \hbar k$ (where v is the velocity), to an applied external force, F, with respect to the periodic lattice potential. The result being that carriers are accelerated as if they had this effective mass rather than the free electron mass in vacuum (m_0). According to Eq. 1.4, we see that the coefficient of the E-k relationship determines the curvature of E versus k. Alternatively, the effective mass is defined by the curvature according to:

$$m^* = \hbar \left(\frac{\partial^2 E}{\partial k^2} \right)^{-1}$$ **Eq. 1.5**

Direct and indirect bandgap semiconductors

Semiconductors can be further differentiated based on the nature of the transition between the VBM to the CBM. They can be classed as either direct or indirect bandgap materials based on the overlap of the VBM and CBM in k space. For a direct band gap semiconductor, the VBM and CBM overlap in k space and a photon with energy $h\nu \geq E_g$ can excite electrons to the CB through a vertical transition (Figure 1.3a). Indirect band gap semiconductors, however, are characterized by an offset of the VBM and CBM in k space (Figure 1.3b). Since photons do not carry momentum they would not be sufficient for a VBM to CBM transition (momentum conservation). Unless, the photon couples with a phonon (lattice vibration), which can provide sufficient momentum to make up the
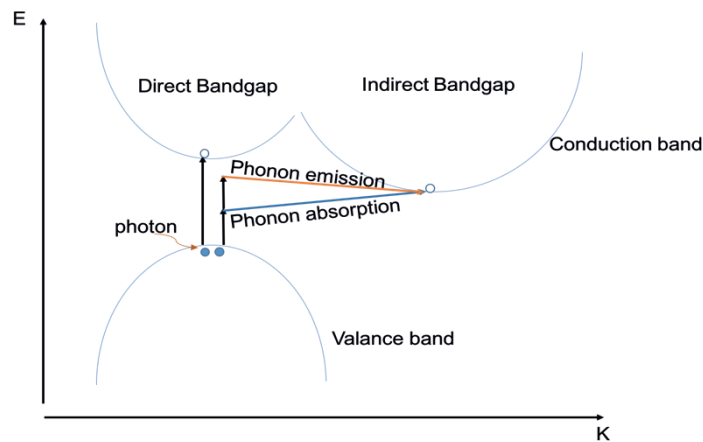
Figure 1.4- In the direct band gap the CBM occurs at the same point in k space as the highest point as the VBM, allowing for a direct optical transition to occur without a significant change in the k vector. The energy gap between the two bands can be determined by the threshold frequency for absorption (λ_{onset}). In the case of the indirect bandgap the transition involves both a photon and simultaneous coupling with a phonon (either through emission or absorption of a phonon). With the absorption onset being determined by the energy of the photon as well as that of the phonon involved in the transition.

offset in k space. Direct band gap semiconductors are usually characterized by large absorption coefficients for photon energies $h\nu > E_g$. Indirect band gap materials, on the other hand, have significantly lower absorption coefficients (probability wise). This arises due to the momentum offset that requires simultaneous coupling of a photon with a phonon in order for absorption to occur. The most well-known example of an indirect semiconductor are silicon and GaAs; this explains why fairly thick silicon crystals are needed in photovoltaic cells for complete absorption of the incident radiation.

1.2   Organic-inorganic perovskite photovoltaics

1.2.1 Background

Perovskites were discovered in 1839 by Gustav Rose,[8] who went on to name them after the Russian mineralogist Lev Perovski. The name initially referred to the mineral $CaTiO_3$ but was later extended to encompass materials that had a similar crystal structure and a
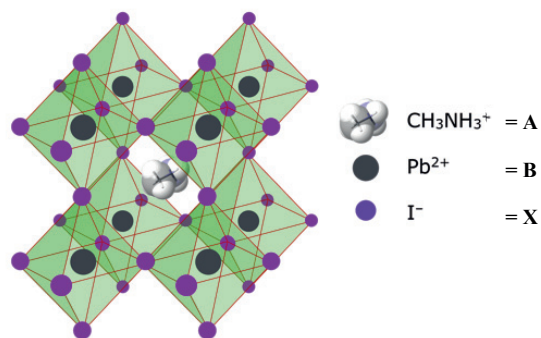
Figure 1.5 – Crystal structure of the perovskite - $CH_3NH_3PbI_3$. Where A = $CH_3NH_3^+$, B = Pb^{2+} and X = I^-

comparable ABX_3 stoichiometry, where A is a cation, B a metal cation and X an oxide or halide anion (Figure 1.5).

The first reports of hybrid organo-metallic perovskites (OMP) were by Webber et al.[9] in 1978, who studied compounds with the composition $CH_3NH_3PbX_3$ (X= Cl, Br & I). Their application as a photovoltaic material came much later and was initially demonstrated in 2009 by Kojima et al.[2] who made devices with $CH_3NH_3PbX_3$ (X = I & Br) with device efficiencies of 3.8% (X = I) and 3.1% (X = Br). The dye-sensitized solar cell architecture developed at the EPFL[10,11] served as the template for their first application, with the perovskite active layer replacing the conventional dye sensitizer on a mesoporus-TiO_2 (mp-TiO_2) scaffold. The initial iterations of perovskite based photovoltaic devices faced some significant hurdles, the foremost being that they rapidly decomposed in the liquid electrolyte that served as the redox mediator for the DSSCs.[12] The limitations of the liquid electrolyte were overcome by replacing it with the solid state hole transport material, spiro-MeOTAD[1], which had orginially been used for solid-state DSSCs.[13] In 2012, Kim et al.[3] reported OMP solar cells using spiro-MeOTAD as the hole transporter. Their work resulted in significant improvements in the power conversion efficiency (PCE) to 9.7% and devices which were markedly more stable than their liquid electrolyte counterparts. Work undertaken simultaneously by Lee et al.[4] showed that the perovskite could function in device architectures where the electron accepting mp-TiO_2 was replaced with insulating mp-Al_2O_3, achieving even higher PCEs of 10.7%. Their

---

[1] 2,2',7,7'-Tetrakis-(N,N-di-4-methoxyphenylamino)-9,9'-spirobifluorene

work also demonstrated that the perovskite's functions are significantly more comprehensive than the dyes that they replaced in the early devices.[12,14] The initial papers in 2012[3,4] that demonstrated the all-solid-state perovskite devices were extraordinary, in the sense that these seminal works already produced photovoltaic devices with power conversion efficiency's that surpassed solid-state DSSCs[15] and rivalled state-of-the-art liquid electrolyte DSSCs at the time.[16] The high device performances triggered a lot of research interest and the simple solution processing requirements for device fabrication meant a low entry barrier to the field. This has resulted in a substantial amount of research activity occurring over a very short time, literature publications around organometallic perovskites have risen exponentially since the handful in 2012 to over 1200 in 2015. Device efficiencies have steadily improved over the last four years as well, more than doubling to a current record efficiency of 22.1%.[17] The improvements in performance are mostly correlated with two parameters, substantial advances in morphological engineering of the film to improve carrier transport and tuning of the chemical composition to optimize material properties such as the optical band gap. In addition to their use as photovoltaic materials, their applications have grown to include use in water splitting,[18] light emitting diodes (LEDs),[19] OMP nanowire lasers[20] and photodetectors.[21]

1.2.2 Film fabrication and device architectures

The morphological quality of the OMP film is a critical parameter in determining the device efficiency, as it defines how well photogenerated electrons and holes are transported across the film to their respective extraction interfaces. Preparation methods for film formation have been extensively investigated and their optimization is ongoing. The established techniques are illustrated in Figure 1.6.[22] There are two primary film fabrication routes, the first of which is based on the deposition of the film from solution in either a one-step method[4] or a two-step method developed by Burshka et al.[23] (Figure1.6 a & b). The second is through vapor deposition[24-26] of the precursors which allows for high precision control of the film thickness and its composition (Figure 1.6d). These techniques, through control of the deposition parameters offer routes to control the formation of the perovskite crystals by affecting their nucleation and growth. In addition to the deposition method, morphological control can be achieved through engineering
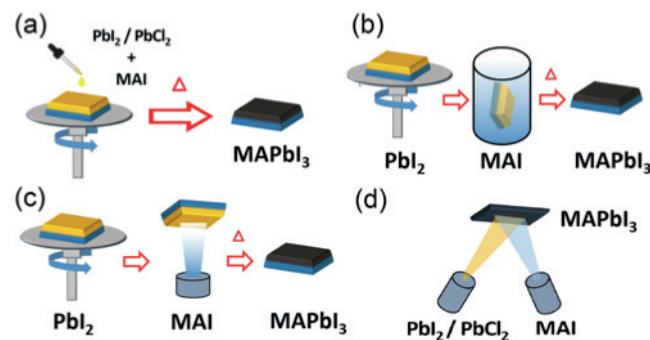
Figure 1.6 - Deposition methods for OMP perovskite thin films, including (a) single-step solution deposition, (b) two-step solution deposition, (c) two-step hybrid deposition, and (d) thermal vapor deposition. Taken from reference 22

with the solvents[27] and processing parameters[28-30] (such as annealing or anti-solvent addition during the spin coating process) used in the film formation process.[22,31]

Two of the most common device architectures are presented in Figure 1.7. As previously mentioned the OMP layer had initially been thought of as a replacement of the dyes that sensitized the mp-TiO$_2$ in the DSSC.[2,12] However, their ability to efficiently disassociate, as well as transport charge carriers after photoexcitation opened them up to a wider range of device architectures. Although the highest performing devices (PCE 21.1%) currently still use perovskite infiltrated mp-TiO$_2$,[32] these devices generally have a perovskite layer that "caps" the mp-TiO$_2$ (Figure 1.7a). The thickness of this capping layer ($\approx$ 500nm) is significant relative to the mp-TiO$_2$ ($\approx$ 150nm), making the device structure near to that of a completely planar device. The perovskite functions as the light absorber and subsequent to the absorption of a photon, photogenerated electrons and holes are transported to the electron transport (ETM) and hole transport (HTM) interfaces respectively. The OMP, being able to transport both charge carriers efficiently over
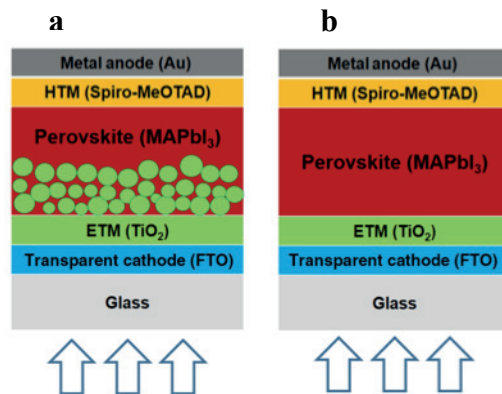
Figure 1.7 - Schematic diagrams of perovskite solar cells in the (a) n-i-p mesoscopic, (b) n-i-p planar. Adapted from reference 22

distances >1 um[33] means that being in high proximity to the carrier accepting interface is not a requirement. Hence, completely planar devices (Figure 1.7b) that use thin films of TiO_2 or SnO_2 as the ETM are also under study.[34,35] For the hole transport material (HTM), spiro-MeOTAD continues to be the material of choice for state-of-the-art devices.

1.2.3 Crystal structure and optical properties

The general schematic of the crystal structure of hybrid OMPs are presented in Figure 1.8.[36] The ideal perovskite has a simple cubic structure, where BX_6 (PbI_6 in Figure 1.8) corner sharing octahedra form three dimensional networks. The organic cation (A) ($CH_3NH_3^+$ in Figure 1.8) fills the interstitials between the octahedral. The $CH_3NH_3^+$ ions can rotate within their octahedral cages, with potentially significant consequences for the electronic structure that will be discussed later in the introduction. A key strength of OMPs is the ability to easily tune their chemical composition. This allows us to tailor the physical dimensions of the crystal, the morphology and the electronic transitions by altering the ions that constitute the perovskite material. By changing the molecular cation (A site) we can change the polarization, as well as break the three-dimensional crystal network. In 2001, Mitzi et al.[37] showed that 2-D sheets and 1-D rods of organo-metallic perovskites could be fabricated by introducing larger cations, and Wu et al. [38]
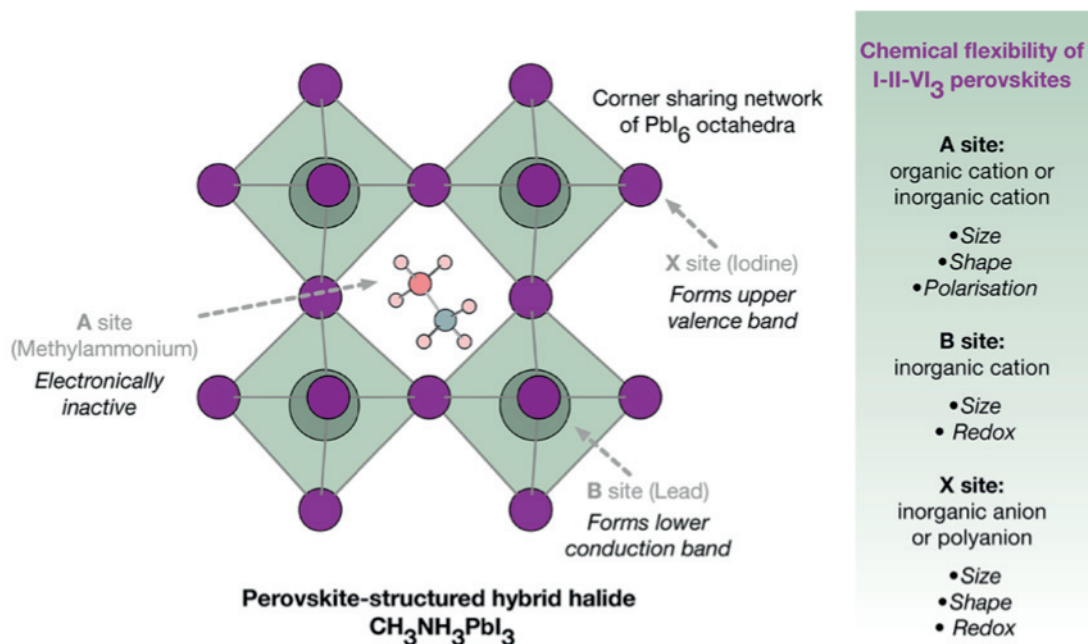
Figure 1.8 –. Schematic of the perovskite crystal structure with respect to the A, B, and X lattice sites. The redox chemistry of the component ions can be used to influence the valence and conduction band energies and orbital composition, and hence the stability of electrons and holes in the material. For larger molecular A sites layered perovskites are formed. Reproduced from reference 36.

demonstrated an increasing density of excitonic trap states on confining the crystals dimensions. The redox properties of the material are primarily governed by the metal cation and halide anions in the B and X sites respectively. Substitution of the halides that occupy the X sites can tune the bandgap in proportion to their electronegativity,[39] with the bandgaps increasing according to $Cl > Br > I$. Kulkarni et al.[40] demonstrated the ability to continuously tune the absorption onset by varying the halide concentration in the $CH_3NH_3PbI_{3-x}Br_x$ composition, for x between $0 < x < 3$, shifting the band gap from 1.55eV (x = 0) to 2.2eV (x = 3). Similar substitutions between Cl/Br have also been demonstrated,[41] substitution of the iodide by chloride ions are however not possible.

Initial demonstrations of $CH_3NH_3PbI_{3-x}Cl_x$, formed by vapor deposition showed high device efficiencies of 15%,[42] however later studies showed that the large mismatch between the size of I^- and Cl^- meant that a negligible amount of Cl^- remains in the film. The function of the chloride was primarily in aiding the formation of the perovskite crystals and improving the film morphology[43] (which would certainly be an important parameter in the perspective of device performance). Substitution of the B site has also been demonstrated as an avenue for tuning the optical absorption, alloying the OMP by partially replacing Pb by Sn can shift the band gap from $E_g = 1.55$ to $1.17 eV$.[44]

1.2.4 Electronic structure

The presence of heavy Pb and I atoms in OMPs is expected to give rise to relativistic effects, specifically enhanced Spin-Orbit Coupling (SOC). This was indeed identified through DFT calculations by Evans et al.[45]. Their work showed a significant SOC impact on the electronic structure of the OMP. Which resulted in a breaking of the degeneracy of the conduction band (CB) to form a triply degenerate CB which can be populated through direct transitions from a single valence band (VB). Further theoretical work by Zheng et al.[46] subsequently showed that the strong SOC effect due to the heavy elements combines with asymmetric fields in locally polarized domains resulting in a Rashba effect. The result in a shift of the CB in k space relative to the VB, forming an indirect transition between their minima (Figure 1.9b). The rotation of the $CH_3NH_3^+$ cations were shown to result in a breaking of the crystal symmetry, forming dynamic local polar distortions that contribute to the Rashba effect. [47-50]
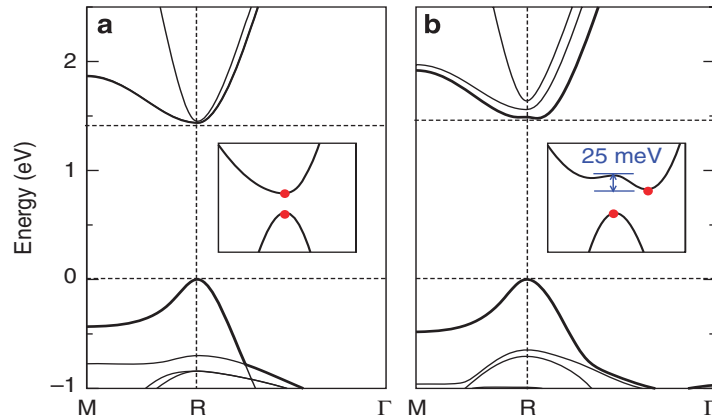
Figure 1.9 – Band structure of the fully relaxed $CH_3NH_3PbI_3$ crystal. The bands are shown for molecule orientations along (a) (111) and (b) (011) direction. The insets show a magnification of the bands (which have been shifted in energy for convenience) around the bandgap and highlight the changes in the VBM and CBM caused by the rotation of $CH_3NH_3^+$. Note that for the (011) orientation the bandgap becomes indirect. Taken from reference 50.

1.2.5 Carrier transport

The carrier transport properties of a material are a crucial consideration in the perspective of their suitability for application in photonic devices. The related observables of interest are carrier diffusion lengths, lifetimes, effective mass, mobilities and the scattering processes that limit carrier mobility. A large part of this thesis involves the investigation of carrier transport properties in OMP materials and a short review of relevant literature will be presented below.

Literature Review

Initial measurements of the carrier diffusion lengths found values that matched or exceeded the typical OMP film thickness in photovoltaic devices, meaning that photogenerated carriers could efficiently reach their accepting interfaces prior to loss through recombination. Xing et al.[51] found diffusion lengths of 100 nm for $CH_3NH_3PbI_3$ perovskites while Stranks et al.[33] established values > 1 μm for $CH_3NH_3PbI_{3-x}Cl_x$. As mentioned previously this is likely to be due to the improved morphology that Cl incorporation provides in the vapor deposition process, which manifests as significantly larger carrier diffusion lengths. Importantly, the studies also found that diffusion lengths were comparably long for both electrons and holes. Subsequent work by Li et al.[52] determined μm diffusion lengths (for both electrons and holes) for $CH_3NH_3PbI_3$ that were comparable to those of $CH_3NH_3PbI_{3-x}Cl_x$. Dong et al.[53] demonstrated diffusion lengths exceeding 175μm in solution grown single crystals of $CH_3NH_3PbI_3$. The long diffusion lengths are a result of high carrier mobilities (relative to organic semiconductors) and long carrier lifetimes. With Wehrenfennig et al.[54] and Marchioro et al.[55] demonstrating lifetimes of 4.9 μs and 15 μs in films of $CH_3NH_3PbI_{3-x}Cl_x$ and $CH_3NH_3PbI_3$.

SOC–GW calculations by Umari et al.[56] for the effective mass of electrons and holes gave values of $m_e^* = 0.19$ and $m_h^* = 0.25$. Other theoretical and experimental work produced carrier effective mass values that were in close agreement.[57,58] Interestingly the work by Umari et al. shows that the effective mass of electrons is lower than that of holes. Since carrier mobility is inversely proportional to the effective mass ($\mu = e\tau/m^*$, here τ is the scattering time of carriers), this would lead to electrons having a higher mobility.

Further theoretical work by Motta et al. using DFT simulations found hole mobilities of $1-5$ cm^2 V^{-1} s^{-1} and an electron mobilities between $5-10$ cm^2 V^{-1} s^{-1}. Hall measurements of the carrier mobility by Stoumpos et al.[59] revealed electron-hole averaged mobilities of 66 cm^2 V^{-1} s^{-1} for $CH_3NH_3PbI_3$ and values as high as 2320 cm^2 V^{-1} s^{-1} for $CH_3NH_3SnI_3$. Y. Chen et al.[60] also report Hall effect measurements of $CH_3NH_3PbI_3$ for polycrystalline films but they obtained a much lower value of 8 cm^2 V^{-1} s^{-1}.

Another method to directly probe charge carrier mobility is through the use of time resolved-THz spectroscopy (TR-THz), a review of the THz technique is provided in chapter 2. Using this technique Wehrenfennig et al.[54] measured carrier mobilities of 8 cm^2 V^{-1} s^{-1} to 11.6 cm^2 V^{-1} s^{-1} . The technique allows for the direct probing of charge carriers due to their interaction with radiation in the THz regime, however it does not make a distinction between electrons and holes, giving the sum of the individual carrier mobility instead. Ponseca et al.[61] used TR-THz to investigate OMP samples with and without mp-TiO_2 (which functions as an electron acceptor). The low mobility of electrons in TiO_2 (< 1 cm^2 V^{-1} s^{-1})[62] relative to the OMP allowed them to dis-entangle their calculated mobility value (20 cm^2 V^{-1} s^{-1}). Obtaining an electron mobility of 12.5 cm^2 V^{-1} s^{-1} and a hole mobility of 7.5 cm^2 V^{-1} s^{-1}, with electrons having a higher mobility of a factor ≈ 2.[61] In both the previous TR-THz studies the carrier generation efficiency ϕ is taken as unity (i.e. all absorbed photons form free charge carriers) and the observed photoconductivity were frequency averaged values over the accessible THz domain. The frequency resolved photoconductivity can also be obtained using the TR-THz technique, fitting the conductivity spectrum with an appropriate model provides an alternative means

to obtain the materials carrier mobility. La-o-vorakiat et al.[63] obtained mobility values by fitting their photoconductivity spectrum with the Drude-Smith model, finding a mobility of 260 $cm^2 V^{-1} s^{-1}$, notably the generation efficiency used in their calculations was $\phi = 0.05$ which is an exceptionally low value and significantly affects the calculated mobility values. Indeed, using a generation efficiency of $\phi = 1$ for their mobility calculation would result in a mobility of 13 $cm^2 V^{-1} s^{-1}$, in line with the reports of Wehrenfennig et al.[54] and Ponseca et al.[61]. Valverde-Chávez et al.[64] also measured high carrier mobilities of 800 $cm^2 V^{-1} s^{-1}$ using the TR-THz technique with a broadband THz probe. Unlike previous work, they measured single crystals of $CH_3NH_3PbI_3$ rather than solution processed polycrystalline films. Savenije et al.[65] used time resolved microwave conductivity (TR-MC) to measure a mobilities of 6.2 $cm^2 V^{-1} s^{-1}$ and also monitored the dependence of carrier mobility on temperature, obtaining a relationship of $\mu \propto T^{-1.6}$ indicating phonon limited carrier mobility.

1.2.6 Defects and morphology

The presence of defects can play a significant role in the performance of a photovoltaic device, due to their detrimental effect on carrier mobilities and lifetimes. In a crystalline semiconductor, defects can manifest in three primary forms, point defects, linear defects and planar defects. Point defects can arise from extrinsic impurity atoms in the crystal structure or native point defects that can be vacancies of a positive and a negative ion, which are called Schottky defects or a vacancy caused by the movement of an ion to interstitial site that is referred to as a Frenkel defect. Defects also take the form of

dislocations within the crystal and unterminated grain boundaries between crystals. All of these can act as trap sites, which have electronic states within the semiconductor band gap and result in carrier localization and loss through non-radiative recombination pathways. They can also act as centres where mobile charge carriers scatter. Carrier mobility is proportional to the average time between scattering events and an increase in defect density would contribute to a reduction of the carrier mobility.[66] A reduction in mobility would be detrimental to the performance of photovoltaic devices, where rapid carrier transport to the extraction interface is a critical parameters.

As a consequence of the above, the variations in carrier mobility reported in literature can largely be attributed to the variety of processing conditions that have been used for film fabrication. The solution processability of the organo-metallic perovskites are one of their biggest strengths, but it also gives rise to large variations between films in terms of defects within the perovskite grains as well as the macroscale morphology of the fabricated thin films. Large single crystals of OMPs would be near ideal systems to characterize the intrinsic properties of the material. Investigation of solution processed films should attempt to link experimental observations to device performance as well as the film morphology. This would allow for a better understanding of their correlation and provide practical insights and direction for future work.

Work by DeQuilettes et al.[29] used correlated microscopy and photoluminescence (PL) measurements to demonstrate the microstructure dependence of luminescence in polycrystalline OMP films. Their work revealed significant variations between the different grains that make up a single solution processed film, in terms of the magnitude

of radiative and nonradiative carrier recombination pathways. The photoluminescence (PL) was shown to have large variations with certain grains exhibiting brighter PL, indicating more efficient radiative recombination. While in other grains, non-radiative recombination pathways are dominant and they are hence darker. The grain boundaries were generally dimmer in all cases, indicating faster, non-radiative recombination occurs at the interfaces between grains. Chemical treatment of their films using pyradine was shown to partially passivate non radiative traps at the grain boundaries, resulting in increased radiative recombination.

1.3 Electroabsorption

The splitting of spectral lines in atoms and molecules by application of static external electric field was discovered Joahnnes Stark in 1913[67] and forms the basis of Stark spectroscopy. More broadly, Electroabsorption (EA) corresponds to a change in a materials absorption spectrum due to the presence of a local or externally applied electric field. The differential absorption (ΔA) signal is detected using a modulation technique and is calculated by subtracting the steady state absorption from the absorption of the material subjected to an electric field (illustrated in Figure 1.10).
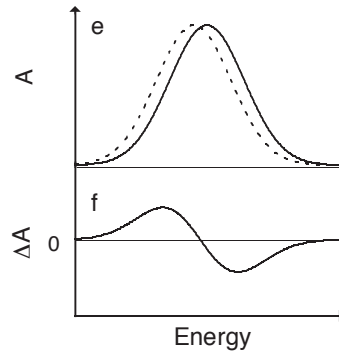
Figure 1.10 – Due to the static electric field the absorption spectrum of the material is shifted (dotted and solid lines in the top figure correspond to the absorption spectrum with and without the applied field. The bottom figure corresponds to the calculated difference between the spectra. Figure from ref 67.

This technique can be used to probe the change in dipole moment and polarizability of a transition state by monitoring the dependence of the field strength on the shape and amplitude of the EA spectra.[68] The change in the absorption band shape, $\Delta A(\nu)$, of molecular and excitonic species subjected to an electric field $\vec{E}$ can be described as the linear combination of first and second derivatives of the static absorption spectrum A: [69-71]

$$\Delta A(\lambda) = -\frac{\partial A(\lambda)}{\partial \lambda} \cdot \vec{m}_{0k} \vec{E} - \frac{1}{2}\frac{\partial A(\lambda)}{\partial \lambda} \cdot \vec{p}_{0k} \vec{E}^2 + \frac{1}{2}\frac{\partial^2 A(\lambda)}{\partial \lambda^2} \cdot (\vec{m}_{0k} \vec{E})^2 \quad \textbf{Eq. 1.6}$$

where E is the electric field exerted on the sample, m_{0k} is the change in the permanent dipole moment, and p_{0k} is the difference in polarizability between the ground (0) and state (k) connected by the optical transition that is being probed. The first term in Eq 1.6 is linear in E and reaches zero for isotropic samples, because the transition dipole moment, m_{0k} is averaged over all possible orientations. The second term shows that changes in the

dipole moment are associated with the second derivative of the absorption spectrum, and the last term includes the product of the change in polarizability between the ground and perturbed state, p_{0k}, and the first derivative of the absorption spectrum.

An EA shift can be induced by the application of an external electric field, but it can also be caused by a local electric field formed by photo-generated charge carriers, the resulting coulomb interaction affects the absorbance of the surrounding material. Such EA features due to local electric fields between photogenerated carriers have been shown to manifest after photoexcitation in transient absorption (TA) measurements where no applied external field is present.[71-74] Trinh et al.[71] observed such transient photoinduced EA features in their TA measurements of $CH_3NH_3PbI_3$ films. They attributed their observations to the electric field created by hot carriers that affects the subsequent absorption of the material, resulting in a transient Stark shift. The spectral features associated with their observed photoinduced EA were also observed in EA spectroscopy studies, that investigated the spectral line shape of perovskite films on the application of an external field.[75,76]

1.4 Bibliography

1.   Becquerel, A. E. *Recherches sur les effets de la radiation chimique de la lumière solaire au moyen des courants electriques*. (Comptes rendus de lÁcademie des sciences, 1839).

2.   Kojima, A., Teshima, K., Shirai, Y. & Miyasaka, T. Organometal Halide Perovskites as Visible-Light Sensitizers for Photovoltaic Cells. *J. Am. Chem. Soc.* **131,** 6050–6051 (2009).

3.   Kim, H.-S. *et al.* Lead iodide perovskite sensitized all-solid-state submicron thin film mesoscopic solar cell with efficiency exceeding 9%. *Sci Rep* **2,** 591 (2012).

4.   Lee, M. M., Teuscher, J., Miyasaka, T., Murakami, T. N. & Snaith, H. J. Efficient Hybrid Solar Cells Based on Meso-Superstructured Organometal Halide Perovskites. *Science* **338,** 643–647 (2012).

5.   Fox, M. *Optical properties of solids*. (2010).

6.   Kitel, C. *Introduction to solid state physics*. (Introduction to Solid State Physics, 1971).

7.   Hendry, E. Charge dynamics in novel semiconductors. *Thesis* (2005).

8.   Rose, G. Beschreibung einiger neuen Mineralien des Urals. *Annalen der Physik* **124,** 551–573 (1839).

9.   WEBER, D. CH3NH3PbX3, a Pb(Ii)-System with Cubic Perovskite Structure. *Zeitschrift Fur Naturforschung Section B-a Journal of Chemical Sciences* **33,** 1443–1445 (1978).

10.   Desilvestro, J., Graetzel, M., Kavan, L., Moser, J. & Augustynski, J. Highly efficient sensitization of titanium dioxide. *J. Am. Chem. Soc.* **107,** 2988–2990 (1985).

11.   O'regan, B. & Grfitzeli, M. A low-cost, high-efficiency solar cell based on dye-sensitized. *Nature* (1991).

12.   Im, J.-H., Lee, C.-R., Lee, J.-W., Park, S.-W. & Park, N.-G. 6.5% efficient perovskite quantum-dot-sensitized solar cell. *Nanoscale* **3,** 4088–4093 (2011).

13.   Grätzel, M. *et al.* Solid-state dye-sensitized mesoporous TiO2 solar cells with high

photon-to-electron conversion efficiencies. *Nature* **395,** 583–585 (1998).

14. Kojima, A., Teshima, K., Shirai, Y. & Miyasaka, T. Organometal halide perovskites as visible-light sensitizers for photovoltaic cells. *J. Am. Chem. Soc.* **131,** 6050–6051 (2009).

15. Burschka, J. *et al.* Influence of the counter electrode on the photovoltaic performance of dye -sensitized solar cells using a disulfide /thiolate redox electrolyte. *Energy & Environmental Science* **5,** 6089–6097 (2012).

16. Armstrong, G. Dye-sensitized solar cells: Improving efficiency. *Nat Chem* **4,** 4–5 (2011).

17. *NREL Cell efficiency chart - http://www.nrel.gov/ncpv/images/efficiency_chart.jpg.*

18. Luo, J. *et al.* Water photolysis at 12.3% efficiency via perovskite photovoltaics and Earth-abundant catalysts. *Science* **345,** 1593–1596 (2014).

19. Ling, Y. *et al.* Bright Light-Emitting Diodes Based on Organometal Halide Perovskite Nanoplatelets. *Adv. Mater. Weinheim* **28,** 305–311 (2016).

20. Zhu, H. *et al.* Lead halide perovskite nanowire lasers with low lasing thresholds and high quality factors. *Nat Mater* **14,** 636–642 (2015).

21. Lin, Q., Armin, A., Burn, P. L. & Meredith, P. Filterless narrowband visible photodetectors. *Nature Photonics* **9,** 687–694 (2015).

22. Song, Z., Watthage, S. C., Phillips, A. B. & Heben, M. J. Pathways toward high-performance perovskite solar cells: review of recent advances in organo-metal halide perovskites for photovoltaic applications. *J. Photon. Energy* **6,** 022001–022001 (2016).

23. Burschka, J. *et al.* Sequential deposition as a route to high-performance perovskite-sensitized solar cells. *Nature* **499,** 316–319 (2013).

24. Chen, C. W. *et al.* Efficient and Uniform Planar-Type Perovskite Solar Cells by Simple Sequential Vacuum Deposition. *Adv. Mater. Weinheim* **26,** 6647–6652 (2014).

25. Chen, Q. *et al.* Planar heterojunction perovskite solar cells via vapor-assisted solution process. *J. Am. Chem. Soc.* **136,** 622–625 (2014).

26. Teuscher, J., Ulianov, A., Müntener, O., Grätzel, M. & Tétreault, N. Control and Study of the Stoichiometry in Evaporated Perovskite Solar Cells. *ChemSusChem* **8,** 3847–3852 (2015).

27. Zhao, Y. & Zhu, K. Solution Chemistry Engineering toward High-Efficiency Perovskite Solar Cells. *J. Phys. Chem. Lett.* **5,** 4175–4186 (2014).

28. Xiao, Z. *et al.* Solvent Annealing of Perovskite-Induced Crystal Growth for Photovoltaic-Device Efficiency Enhancement. *Adv. Mater. Weinheim* **26,** 6503–6509 (2014).

29. deQuilettes, D. W. *et al.* Impact of microstructure on local carrier lifetime in perovskite solar cells. *Science* **348,** 683–686 (2015).

30. Tosun, B. S. & Hillhouse, H. W. Enhanced Carrier Lifetimes of Pure Iodide Hybrid Perovskite via Vapor-Equilibrated Re-Growth (VERG). *J. Phys. Chem. Lett.* **6,** 2503–2508 (2015).

31. Salim, T. *et al.* Perovskite-based solar cells: impact of morphology and device architecture on device performance. *Journal of Materials Chemistry A* **3,** 8943–8969 (2015).

32. Saliba, M. *et al.* Cesium-containing Triple Cation Perovskite Solar Cells: Improved Stability, Reproducibility and High Efficiency. *Energy & Environmental Science* (2016). doi:10.1039/C5EE03874J

33. Stranks, S. D. *et al.* Electron-hole diffusion lengths exceeding 1 micrometer in an organometal trihalide perovskite absorber. *Science* **342,** 341–344 (2013).

34. Zhou, H. *et al.* Interface engineering of highly efficient perovskite solar cells. *Science* **345,** 542–546 (2014).

35. Baena, J. P. C. *et al.* Highly efficient planar perovskite solar cells through band alignment engineering. *Energy & Environmental Science* **8,** 2928–2934 (2015).

36. Walsh, A. Principles of Chemical Bonding and Band Gap Engineering in Hybrid Organic-Inorganic Halide Perovskites. *J. Phys. Chem. C* **119,** 5755–5760 (2015).

37. Mitzi, D. B. Templating and structural engineering in organic–inorganic perovskites. *Journal of the Chemical Society, Dalton Transactions* **0,** 1–12 (2001).

38. Wu, X. *et al.* Trap States in lead iodide perovskites. *J. Am. Chem. Soc.* **137,** 2089–

2096 (2015).

39. Butler, K. T., Frost, J. M. & Walsh, A. Band alignment of the hybrid halide perovskites $CH_3NH_3PbCl_3$, $CH_3NH_3PbBr_3$ and $CH_3NH_3PbI_3$. *Materials Horizons* **2,** 228–231 (2015).

40. Kulkarni, S. A. *et al.* Band-gap tuning of lead halide perovskites using a sequential deposition process. *Journal of Materials Chemistry A* **2,** 9221–9225 (2014).

41. Protesescu, L. *et al.* Nanocrystals of Cesium Lead Halide Perovskites ($CsPbX_3$, X = Cl, Br, and I): Novel Optoelectronic Materials Showing Bright Emission with Wide Color Gamut. *Nano Lett.* **15,** 3692–3696 (2015).

42. Liu, M., Johnston, M. B. & Snaith, H. J. Efficient planar heterojunction perovskite solar cells by vapour deposition. *Nature* **501,** 395–398 (2013).

43. Yu, H. *et al.* The Role of Chlorine in the Formation Process of '$CH_3NH_3PbI_{3-x}Cl_x$' Perovskite. *Advanced Functional Materials* **24,** 7102–7108 (2014).

44. Kanhere, P., Chakraborty, S., Rupp, C. J., Ahuja, R. & Chen, Z. Substitution induced band structure shape tuning in hybrid perovskites ($CH_3NH_3Pb_{1-x}Sn_xI_3$) for efficient solar cell applications. *RSC Advances* **5,** 107497–107502 (2015).

45. Even, J., Pedesseau, L., Jancu, J.-M. & Katan, C. Importance of Spin-Orbit Coupling in Hybrid Organic/Inorganic Perovskites for Photovoltaic Applications. *J. Phys. Chem. Lett.* **4,** 2999–3005 (2013).

46. Zheng, F., Tan, L. Z., Liu, S. & Rappe, A. M. Rashba Spin–Orbit Coupling Enhanced Carrier Lifetime in $CH_3NH_3PbI_3$. *Nano Lett.* **15,** 7794–7800 (2015).

47. Leppert, L., Reyes-Lillo, S. E. & Neaton, J. B. Electric Field- and Strain-Induced Rashba Effect in Hybrid Halide Perovskites. *J. Phys. Chem. Lett.* **7,** 3683–3689 (2016).

48. Etienne, T., Mosconi, E. & De Angelis, F. Dynamical Origin of the Rashba Effect in Organohalide Lead Perovskites: A Key to Suppressed Carrier Recombination in Perovskite Solar Cells? *J. Phys. Chem. Lett.* **7,** 1638–1645 (2016).

49. Azarhoosh, P., Frost, J. M., McKechnie, S., Walsh, A. & van Schilfgaarde, M. Relativistic origin of slow electron-hole recombination in hybrid halide perovskite

solar cells. *APL Materials* **4,** 091501 (2016).

50. Motta, C. *et al.* Revealing the role of organic cations in hybrid halide perovskite CH3NH3PbI3. *Nat Comms* **6,** 7026 (2015).

51. Xing, G. *et al.* Long-Range Balanced Electron-and Hole-Transport Lengths in Organic-Inorganic CH3NH3PbI3. *Science* **432,** 344–347 (2013).

52. Li, Y. *et al.* Direct Observation of Long Electron-Hole Diffusion Distance in CH3NH3PbI3 Perovskite Thin Film. *Sci Rep* **5,** 14485 (2015).

53. Dong, Q. *et al.* Electron-hole diffusion lengths > 175 μm in solution-grown CH3NH3PbI3 single crystals. *Science* **347,** 967–970 (2015).

54. Wehrenfennig, C., Eperon, G. E., Johnston, M. B., Snaith, H. J. & Herz, L. M. High charge carrier mobilities and lifetimes in organolead trihalide perovskites. *Adv. Mater. Weinheim* **26,** 1584–1589 (2014).

55. Marchioro, A. *et al.* Unravelling the mechanism of photoinduced charge transfer processes in lead iodide perovskite solar cells. *Nature Photonics* **8,** 250–255 (2014).

56. Umari, P., Mosconi, E. & De Angelis, F. Relativistic GW calculations on CH3NH3PbI3 and CH3NH3SnI3 Perovskites for Solar Cell Applications. *Sci Rep* **4,** 4467 (2014).

57. Filip, M. R., Verdi, C. & Giustino, F. GW Band Structures and Carrier Effective Masses of CH3NH3PbI3 and Hypothetical Perovskites of the Type APbI$_3$: A = NH4, PH4, AsH4, and SbH4. *J. Phys. Chem. C* **119,** 25209–25219 (2015).

58. Galkowski, K. *et al.* Determination of the exciton binding energy and effective masses for methylammonium and formamidinium lead tri-halide perovskite semiconductors. *Energy & Environmental Science* **9,** 962–970 (2016).

59. Stoumpos, C. C., Malliakas, C. D. & Kanatzidis, M. G. Semiconducting Tin and Lead Iodide Perovskites with Organic Cations: Phase Transitions, High Mobilities, and Near-Infrared Photoluminescent Properties. *Inorg. Chem.* **52,** 9019–9038 (2013).

60. Chen, Y. *et al.* Extended carrier lifetimes and diffusion in hybrid perovskites

revealed by Hall effect and photoconductivity measurements. *Nat Comms* **7,** 12253 (2016).

61.   Ponseca, C. S. *et al.* Organometal halide perovskite solar cell materials rationalized: ultrafast charge generation, high and microsecond-long balanced mobilities, and slow recombination. *J. Am. Chem. Soc.* **136,** 5189–5192 (2014).

62.   Bonn, M. THz Studies of Charge and Exciton Dynamics in Semiconductor Nanostructures. in CMT3–2 (OSA, 2009). doi:10.1364/CLEO.2009.CMT3

63.   La-o-vorakiat, C. *et al.* Elucidating the role of disorder and free-carrier recombination kinetics in $CH_3NH_3PbI_3$ perovskite films. *Nat Comms* **6,** 7903 (2015).

64.   Valverde-Chávez, D. A. *et al.* Intrinsic femtosecond charge generation dynamics in single crystal CH3NH3PbI3. *Energy & Environmental Science* **8,** 3700–3707 (2015).

65.   Savenije, T. J. *et al.* Thermally Activated Exciton Dissociation and Recombination Control the Carrier Dynamics in Organometal Halide Perovskite. *J. Phys. Chem. Lett.* **5,** 2189–2194 (2014).

66.   Ball, J. M. & Petrozza, A. Defects in perovskite-halides and their effects in solar cells. *Nature Energy* **1,** 16149 (2016).

67.   Stark, J. Beobachtungen über den Effekt des elektrischen Feldes auf Spektrallinien. I. Quereffekt. *Annalen der Physik* **348,** 965–982 (1914).

68.   Bublitz, G. U. & Boxer, S. G. Stark spectroscopy: applications in chemistry, biology, and materials science. *Annu Rev Phys Chem* **48,** 213–242 (1997).

69.   Lanzani, G. *The photophysics behind photovoltaics and photonics.* (2012).

70.   Roiati, V. *et al.* Stark Effect in Perovskite/TiO2 Solar Cells: Evidence of Local Interfacial Order. *Nano Lett.* **14,** 2168–2174 (2014).

71.   Trinh, M. T., Wu, X., Niesner, D. & Zhu, X.-Y. Many-body interactions in photo-excited lead iodide perovskite. *Journal of Materials Chemistry A* **3,** 9285–9290 (2015).

72.   Causa, M. *et al.* The fate of electron–hole pairs in polymer:fullerene blends for organic photovoltaics. *Nat Comms* **7,** 12556 (2016).

73. Gélinas, S. *et al.* Ultrafast Long-Range Charge Separation in Organic Semiconductor Photovoltaic Diodes. *Science* **343,** 512–516 (2014).

74. Cabanillas Gonzalez, J., Grancini, G. & Lanzani, G. Pump-Probe Spectroscopy in Organic Semiconductors: Monitoring Fundamental Processes of Relevance in Optoelectronics. *Adv. Mater. Weinheim* **23,** 5468–5485 (2011).

75. Wu, X. *et al.* Composition-Dependent Light-Induced Dipole Moment Change in Organometal Halide Perovskites. *J. Phys. Chem. C* **119,** 1253–1259 (2015).

76. Ziffer, M. E., Mohammed, J. C. & Ginger, D. S. Electroabsorption Spectroscopy Measurements of the Exciton Binding Energy, Electron–Hole Reduced Effective Mass, and Band Gap in the Perovskite CH3NH3PbI3. *ACS Photonics* **3,** 1060–1068 (2016).

2 Experimental Techniques

Electromagnetic radiation can serve as a contactless probe of the fundamental processes that occur in photonic materials. By carefully choosing the probe wavelength, we are able to selectively investigate interactions and phenomena that are uniquely visible at specific parts of the electromagnetic spectrum. This gives us the ability to create a broad understanding of the fundamental material properties and processes that occur after photo-excitation. In this chapter the key experimental techniques will be presented. The majority of this thesis involved the investigation of important processes in opto-electronic materials at the femtosecond and picosecond timescale. Femtosecond pulsed lasers were the primary experimental tool used over the course of this work to give us access to the ultrafast time scale. Three primary spectroscopic techniques which relied on ultrafast pulsed lasers, were combined to provide a comprehensive understanding of the process
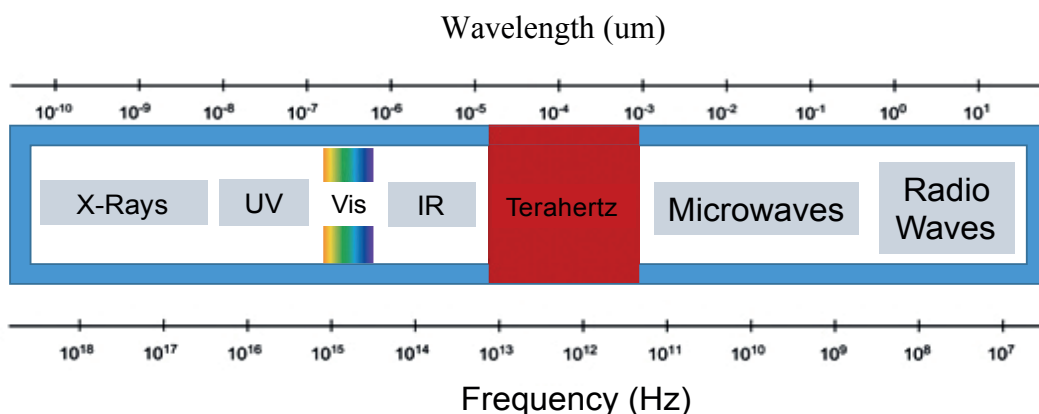
Figure 2.1 – The electromagnetic spectrum with the visible and THz parts of the spectrum highlighted

that occur on the macro and microscale in our investigated films. In transient absorption spectroscopy, we relied on optical pulses in the visible part of the spectrum. While our time-resolved electroabsorption setup used these optical pulses in combination with the application of modulated voltage pulses, to investigate the macroscopic carrier dynamics under applied electric fields. In THz spectroscopy we combine optical excitation in the visible part of the spectrum with probing in the THz domain, to directly observe carrier formation and recombination dynamics and probe the microscopic carrier mobility of photogenerated charge carriers. The fundamentals of the experimental techniques will be presented in detail in this chapter.

2.1 Time-resolved laser spectroscopy

Time resolved spectroscopy allows us investigate fundamental processes that occur within a system in response to controlled external perturbations. These perturbations are usually optical in nature. Ultrafast pulsed lasers that provide pulses of light with a femtosecond duration, were used to investigate the response of photovoltaic materials and devices to optical excitation. Both of the pulsed laser sources used in our measurements were femtosecond Ti:Sapphire amplified pulsed lasers (Clark - CPA-2001 for Transient absorption and electroabsroption spectroscopy and Coherent (Libra USP HE) for time resolved-THz spectroscopy). The femtosecond pulse duration allows us to visualize ultrafast processes occurring down to the femtosecond timescales. In order to monitor these processes in time we use a time resolved setup that uses optical pump and probe pulses. The general outline for such pump-probe measurements are provided in this

section and are generally applicable, with some variation, in all our spectroscopic techniques. Further details related to each spectroscopic technique will be provided in subsequent sections.

In the typical pump-probe technique, we use an optical pump pulse that takes our system to an excited state. The pump wavelength is tuned to access a desired transition within the investigated system. The probe pulse monitors the response of the sample to the pump excitation. This usually manifests as a change in the transmission of the probe through either a reduction in transmission due to the formation of some new species, which absorbs or scatters the probe, or an increase in transmission of the probe due to a bleaching of an electronic transition by the pump (these processes are visible at different parts of the spectrum and depend on the wavelength of the probe pulse). By recording the absorption of the probe with and without the pump we can determine the differential absorption ΔA. By introducing a controllable delay between the pump and probe beams we can monitor the evolution of ΔA in time, giving us the dynamics of the optically excited system. This is accomplished by increasing the path length that the pump or probe travels using a delay stage (which allows us to access the dynamics occurring up to 1ns after photoexcitation). By using a spectrally broad probe pulse we can simultaneously monitor the influence of the pump on different parts of the spectrum and the dynamics of these processes. This gives us a substantial amount information, from which we can reconstruct the processes occurring in our investigated system subsequent to its optical excitation.

2.2   Transient absorption spectroscopy

Femtosecond transient absorption spectroscopy is an ultrafast optical pump-probe technique. The probe in this case is a broadband white light continuum (400 - 900nm), which allows us to monitor the spectral changes and associated dynamics due to pump excitation, in the visible and near-IR parts of the spectrum. The pump is a femtosecond (40-60fs) optical pulse generated using a NOPA, which gives us the ability to tune the excitation wavelength. The resulting, pump induced perturbation to the system is monitored using the probe pulse. Putting the probe pulse on a delay stage allows us to vary the relative delay between the pump and probe and monitor the dynamics between 100fs to 1.2ns. The differential absorption signal of the probe is the difference between the absorbance of the pumped and un-pumped sample. This is obtained by monitoring the transmitted probe intensity with the pump (I_p) and without the pump (I_{np}) and the intensity of the probe on the sample (I_0)

$$\Delta A = A_{pump} - A_{unpumped} = -\log(\frac{I_p}{I_0}) + \log(\frac{I_{np}}{I_0}) = -\log(\frac{I_p}{I_{np}})$$ **Eq. 2.1**

2.3   Time-resolved electroabsorption spectroscopy (TREAS)

The Femotsecond transient absorption measurements detailed in the previous section are a powerful tool in probing the response of a system to optical perturbations. They allow us to observe the spectral signatures of species and phenomena that are the direct result of optical excitation by the pump pulse. In TAS measurements, we usually study

the active layer responsible for the formation and transport of charge carriers. However, the photovoltaic systems we investigate are more complex than just the active layers. The inclusion of electrodes and externally applied electric fields in functioning photovoltaic devices, means that the phenomena and associated dynamics we observe under operational conditions are likely to be far more complex than what we observe with TAS. In order to investigate opto-electronic materials under conditions that move closer to operational ones, the time-resolved electroabsorption spectroscopy (TREAS) has been used which allows us to measure complete devices under externally applied fields and observe the associated photogenerated carrier dynamics and spectral changes that are uniquely visible under these conditions.

Broadly, the technique allows us to monitor the change in the absorption spectrum of a material due to an electric field and the response of photogenerated carriers to the applied field. Initially, to observe the steady-state change in the absorption spectrum upon the application of an electric field (electroabsorption (EA)), the active layer is sandwiched between two electrodes to which a voltage is applied and we observe the EA signal using a broadband probe pulse. In the next step, using a pump-probe scheme we can monitor the drift dynamics of photogenerated charge carriers due to the externally applied field. The formation and drift of photogenerated charge carriers to the oppositely charged electrodes screens the externally applied field, diminishing the effective electric field (E_{eff}) felt by the bulk of the material. We can monitor the reduction in E_{eff} by observing the diminishing spectral signature of the steady state EA that was initially characterized (and is related to the magnitude of the field felt by the bulk of the material). This change

can be associated with the drift of charge carriers and their associated screening of the electric field in time. The dynamics are obtained by delaying the pump relative to the probe while maintaining a constant externally applied field. This allows us to visualize the carrier drift across our investigated film, calculate the carrier mobility in the femtosecond timescales, and observe the dynamics of the carriers' motion across the film in time and as a function of the different processes that can affect their macroscopic drift. Such as trapping/detrapping or grain boundaries which are highly dependent on film morphology. The advantage of the technique lies in our ability to probe the electric field dynamics using femtrosecond optical pulses, which allows us to access time-scales that are significantly shorter than those that can be obtained by purely electrical measurements.

2.3.1 State of the art

Gulbinas et al.[1] used transient Stark spectroscopy to probe the field induced shift of a materials absorption spectrum (Stark shift) and its screening by the separation of photogenerated electron-hole pairs. They demonstrated the dynamic character of the Stark shift absorption band after excitation with pump pulses with a picosecond duration. Monitoring the dynamics of the Stark shift band allowed them to quantitatively analyze the spatial evolution of photo-generated charge pairs. Cabanillas et al[2] used the transient Stark spectroscopy technique to determine the charge mobility of PCBM films in the picosecond regime. They identified two distinct regimes, a short lived period of high

mobility lasting around 10ps and a slower transport regime commencing once carriers reach the inter-domain boundary and trapping becomes efficient, resulting in a reduction of the carrier mobility. Work by A. Devizis et al.[3] used time-resolved electric field induced second harmonic generation (TREFISH) to demonstrate the impact of disorder in amorphous semi-conductors on the carrier mobility. Work done by Jelissa De Jonghe and Andrius Devizis in our lab used the TREAS technique to monitor the formation dynamics of free electrons through the disassociation of interfacial charge transfer (CT) states in planar cyanine/fullerene solar cells[4,5].

2.3.2 ΔAbsorption in TREAS

In order to more clearly understand the technique and the results presented in later chapters, an understanding of the differential absorption signals we obtain from our measurements is important. In conventional TAS measurements, the pump is modulated i.e. every second pump pulse is blocked by a chopper running at 500Hz, half the repetition rate of our 1KHz laser. The $\Delta A(t, \lambda)$ signal we observe is the difference in the broadband probe with the pump ($A_{pump} (t, \lambda)$) and without the pump ($A(t, \lambda)$), as a function of the pump-probe delay (t) and is given by Eq. 2.2.

For the steady state electroabsorption (EA) spectra, we modulate the applied voltage using a function generator that provides square voltage pulses at 500hz, with each pulse having 100us duration. We measure $\Delta A(\lambda)$ by looking at the probe absorption with the

externally applied electric field ($A_E(\lambda)$) and without the applied field ($A(\lambda)$). Which gives us the steady state change in the absorption spectrum of our sample due to the application of an electric field and is given by Eq. 2.3.

For the time resolved electroabsorption measurements, we call the spectra and dynamics obtained electrmodulated differential absorption (EDA) for clarity. In the $\Delta A(t, \lambda)$ signal, the pump is present in both the collected absorption spectra (with a relative pump-probe delay (t)). The voltage pulse is modulated and the difference is taken as the probe absorption **with the pump and applied voltage** ($A_{E+Pump}(t, \lambda)$) and the probe absorption **with the pump but no applied voltage** ($A_{Pump}(t, \lambda)$) and is given by Eq.2.4. Figure 2.2 shows the pump, probe and modulated voltage pulses that are used in a standard TREAS measurement.

TA spectrum
$$\Delta A(t, \lambda) = A_{pump}(t, \lambda) - A(t, \lambda) \qquad \textbf{Eq. 2.2}$$
EA spectrum
$$\Delta A(\lambda) = A_E(\lambda) - A(\lambda) \qquad \textbf{Eq. 2.3}$$
EDA spectrum
$$\Delta A(t, \lambda) = A_{E+Pump}(t, \lambda) - A_{pump}(t, \lambda) \qquad \textbf{Eq. 2.4}$$
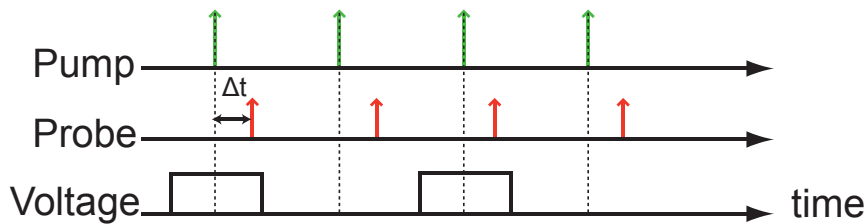
Figure 2.2 – The pump, probe and modulated voltage in a typical EDA measurement. The pump and probe are delayed relative to each other (Δt) and the voltage is modulated so that it is present for every second pump-probe pulse pair1.[5]

2.3.3 Experimental

<u>Laser Source</u>

The laser source used for the TAS and TREAS setups was a Ti:Sapphire femtosecond laser (CPA-2001 from Clark). The frequency doubled output of a Nd:YAG laser (532nm, 7W) pumped with an arc lamp was used to pump the Ti:Sapphire medium. The seed was provided by a frequency doubled Er-doped fiber laser (775nm), which was pumped with a diode laser and constitutes the oscillator of the system. The system uses a chirped pulse amplification (CPA) technique, in which the seed pulse is stretched in the time domain to reduce the peak power. Subsequent to amplification in the laser cavity, the amplified pulse is compressed using diffraction gratings to obtain pulse with a duration of ≈ 150fs and the average energy of the pulses were 920µj.

<u>NOPA</u>

In order to tune the excitation wavelength of the pump beam, a two stage Non-Linear Optical Parametric Amplifier (NOPA) was used. A part of the output of the laser (150uj) was sent to the NOPA. The laser input was divided into two and a small part was used in the first stage to produce a chirped white light continuum (WLC) by focusing on a sapphire plate. The second part of the laser input is frequency doubled using a BBO crystal and again divided (20/80%). The smaller fraction is used in the first stage to select the wavelength we would like as the output of the NOPA. This is achieved by spatially overlapping the beam with the chirped WLC on a BBO crystal and temporally overlapping it with the desired wavelength in the WLC, through which we selectively

amplify the intended wavelength. The resulting signal is further amplified in the second stage by overlapping it on a second BBO with the larger fraction of doubled fundamental of the laser. The output of the NOPA is then compressed using a pair of glass prisms to obtain ≈ 50fs pulses with pulse energies that depend on the output wavelength.

TREAS Measurements

The TREAS setup was originally built in our lab by Dr. Andrius Devizis in 2013, the setup has also been used for the TAS measurements.

The schematic of the TREAS setup is shown in Figure 2.3. The pump beam is generated from the NOPA and the WLC for the probe beam is generated using the fundamental of the laser focused on a 3mm sapphire plate. The polarizations of both the beams are set at their magic angle. The pump-probe delay was controlled using a PI delay stage. A function generator (Tektronik AFG 2001) is used to generate the voltage pulses and is set at 500Hz and produces square voltage pulses of 100μs duration. The pump and probe pulses are at 1KHz and arrive ≈ 50μs after the application of the voltage pulse. The measurements are done in reflectance mode, with the pump and probe beams passing through the transparent electrode and being reflected off the metallic electrode. The probe beam was dispersed in a grating spectrograph (SR163, Andor Technology) and finally detected shot by shot at a 1 kHz rate with a 512×58 pixel back-thinned CCD detector (S07030- 0906, Hamamatsu). Part of the probe beam was split before the sample into a reference beam reaching a second detector, which allowed for corrections of shot-to-shot fluctuations. The same setup has been used for TAS measurements. For which the

function generator was disconnected and a chopper set to 500Hz was used to cut every

second pump pulse.
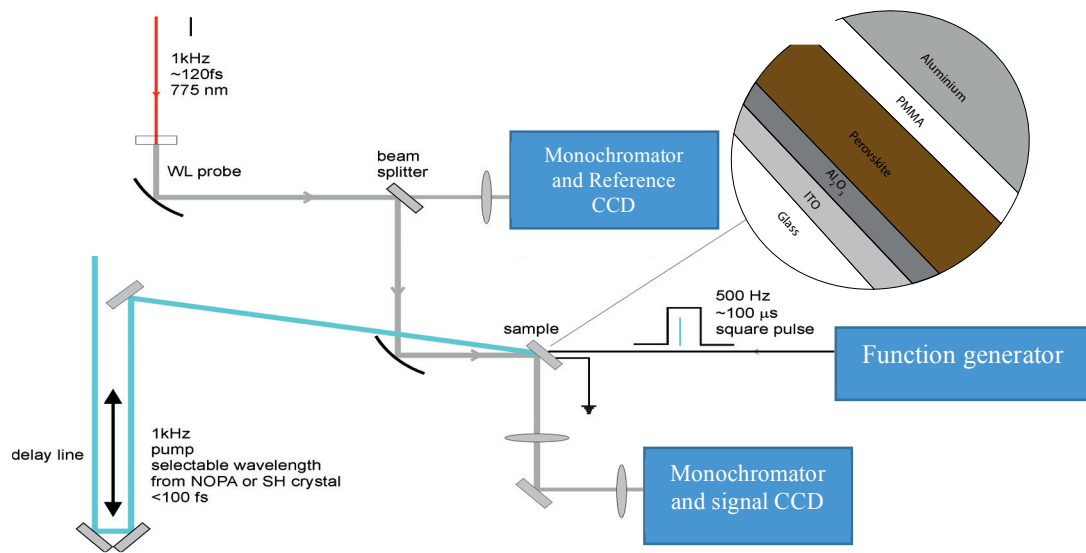
Figure 2.3 – Schematic of the TREAS setup. For TAS measurements a chopper was placed in the path of the pump beam and modulated at 500hz and the function generator was switched off.

2.4 THz Spectroscopy

THz radiation generally refers to the frequency spanning about 100GHz to 30THz. For

reference 1 THz corresponds to a photon with an energy of 4.1meV and wavelength

300μm, which is significantly lower than the typical energy required for electronic

transitions in semi-conductors. THz radiation can nevertheless be used as a probe for

charge carrier formation and dynamics due to the strong scattering and absorption of THz

radiation by free carriers, as well as low frequency vibrations or phonons. The THz-time domain spectroscopy (THz-TDS) technique allows for the determination of both the amplitude and phase of the THz probe pulse, through the direct measurement of the transient electric field of the THz pulse transmitted/reflected through the sample and reference substrate. This allows us to calculate the frequency dependent complex values of conductivity (σ), refractive index(η) and relative dielectric function (ε) across our measured range of 0.4– 2.3THz for the sample.

The addition of an optical pump pulse allows us to carry out time resolved optical pump–terahertz probe spectroscopy (OPTP). The pump pulse is used for photoexcitation of the sample we investigate. Subsequent to absorption of photons, the THz pulse is used to probe the complex induced photoconductivity at a defined time after photoexcitation. We probe the evolution of the photoconductivity of the sample, in time, by delaying the pump excitation relative to the probe pulse. In this manner we can directly visualize charge carrier formation and recombination dynamics.

The use of femtosecond lasers in THz spectroscopy was reported for the first time by Grischkowsky et al.[6] in 1989. Where they used THz radiation generated by photoconductive dipole antennas to investigate water vapor. Since these initial reports, THz-TDS systems have continued to progress with improvements linked to the development of ultrafast laser technology.[7] The Development of alternative THz generation techniques allowed for the extension of the generated frequency range to several THz with pulse durations of 200fs.[8]

A variety of physical systems have been studied using this experimental technique. Investigation of systems using THz-TDS resulted in the observation of the

formation of excitons[9], phonons present in crystalline solids[10] and electron transport properties in TiO_2[11]. Time resolved optical pump-THz probe measurements were used to investigate carrier dynamics in organic molecular crystals[12] and photoinduced carrier dynamics in mp-TiO_2 films[13] and other systems [14]. Reviews of recent work are presented in refs [15,16].

2.4.1 Experimental

Setup

The THz spectroscopy setup that has been used over the course of this thesis was originally built by V.K. Thorsmolle and subsequently rebuilt with a new laser source by Jan C. Brauer. A schematic outline of the THz setup and beam path is provided in Figure 2.4.

1) Laser Source

The laser source for the THz setup was a Ti:Sapphire amplified laser system (LIBRA USP HE, Coherent). The system consists of a Ti:Sapphire oscillator (Vitesse) that is pumped by a Verdi laser head, and provides 4nj pulses at a frequency of 80MHz and a wavelength of 800nm.[17] The regenerative amplifier is pumped using an Evolution laser with a power of 22W and at 1kHz. The generated pulses have an energy of $\approx$ 3.3mj, wavelength of 800nm and pulse duration of 45fs. The output of the laser is divided into three parts: the first goes to pump the OPA, the second is used for THz generation and the third part of the fundamental is used for detection of the THz pulse

2) Optical parametric amplification (OPA)

Using an OPA we can tune the wavelength of the optical pulses we generate based on the requirements (i.e. the absorption spectrum) of the samples we investigate. The OPA used in our setup was an OPerA SOLO (Coherent) that could produce pulses between 235 to 2500nm.

As the input into the OPA we use a part of the 800nm generated from the laser source which is directed into the OPA. A small fraction of this beam is split and focused on a sapphire plate to generate a white light continuum (WLC). The WLC is then stretched temporally and focused on a beta barium borate (BBO) crystal. A small part of the fundamental is also directed on to the BBO crystal so that the two beams overlap spatially. By tuning the temporal delay of the fundamental to match that of the wavelength we would like to select in the temporally stretched WLC and adjusting the BBO angle to have phase matching conditions, we can obtain the desired wavelength. The pre-amplified pulse is then overlapped with the rest of the fundamental of the laser on a second BBO crystal. Changing the angle of the BBO and the delay between the fundamental and pre-amplified pulse allows us to tune the frequency of the generated signal and idler. We can then either directly make use of either of the generated pulses or further convert them by generating their second harmonic or by sum-frequency mixing with a part of the pump pulse.

3) THz generation and detection

In order to generate the THz pulse and subsequently probe its electric field we use the remaining two parts of the fundamental from the laser.

Generation of the THz radiation is accomplished by optical rectification of the 800nm fundamental of the laser in a zinc telluride (ZnTe) crystal. In order to generate the THz pulse we focus 800uj of the fundamental of the laser onto a 1mm ZnTe crystal that results in the emission of THz pulses with a frequency bandwidth between 0.1 to 2.3THz and allows us to carry out measurements with a time-resolution of 400fs. A PTFE (Polytetrafluroethylene / Teflon) plate is placed immediately after the ZnTe crystal, which blocks any fundamental that is transmitted through the ZnTe crystal but is mostly transparent to our generated THz region (between 0.1-3THz). The THz radiation emitted from the ZnTe crystal is collected, collimated and focused on to the sample by gold coated parabolic mirrors. The sample is placed within a cryostat that allows for temperature control. A second PTFE plate is placed just behind the sample to block visible radiation from the pump pulse.

After the THz radiation passes through the sample it is collected and collimated by parabolic mirrors. Electro-optic detection of the transmitted THz electric field is carried out using a second ZnTe crystal. The phase and amplitude information of the transmitted THz pulse is extracted by mapping out the amplitude of its electric field in time. In order to do this the pulse is focused on a second ZnTe crystal. This results in an induced birefringence in the ZnTe crystal that is dependent on the amplitude of the THz wave as it passes through the crystal. A gating beam (fundamental of the laser) is focused on the ZnTe crystal (and spatially overlaps with the THz pulse) and is used to map out the amplitude of the transmitted THz pulse in time. The THz beam incident on the ZnTe crystal results in a tilt of the polarization of the linearly polarized gating beam due to its birefringence. We convert the linear polarization of the gating beam to circular

polarization by using a quarter wave plate (QW in Fig. 2.4). The tilt of polarization of the gating beam passing through the ZnTe crystal, delivers an optical polarization after the QW plate, the difference between its vertical and horizontal components is proportional to the intensity of the THz. The polarization modulation of the gating beam is then converted to an intensity modulation. The vertical and horizontal components of the gating beam are separated using a Wollaston prism and the difference in intensity of the two components are detected using two balanced diodes. By temporally delaying the gating beam (using a delay stage) with respect to the THz wave, the intensity of the THz pulse is monitored in time. The entire THz generation and detection line is enclosed within a dry box that has been purged with nitrogen, to reduce humidity that would absorb THz radiation (under typical measurement conditions the humidity is $\approx 4.5\%$).
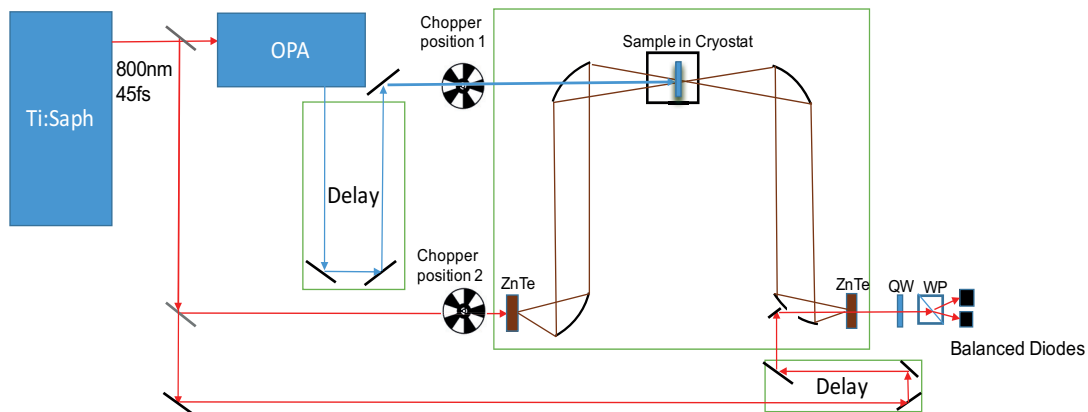
Figure 2.4 – Schematic of the THz setup. Chopper position 1 is used to conduct optical pump THz probe measurements and position 2 is used to conduct dark THz measurements where there is pump excitation.

2.4.2 Data Analysis

The pump-probe experiments with THz radiation are analogous to conventional measurements that use visible light, in terms of using an optical excitation and probing the spectral change at a time t after excitation. However, in addition to the change the intensity of the transmitted probe, we can also have access to the phase shift of the spectral frequencies contained within the THz probe pulse. Which allows us to obtain the complex photoconductivity of the sample. Due to the strong absorption of free charge carriers in the THz spectral region, we can use the THz pulse as a direct probe of photogenerated carrier dynamics (formation, recombination, relaxation, etc.) and their mobility. Photoexcitation by a pump pulse creates charge carriers, controlling the time delay of the pump relative to the THz probe pulse allows us to carry out time resolved THz measurements. Scattering by carriers would reduce the transmitted THz, so our observed ΔT would typically be negative due to a reduction in the transmission after the formation of free carriers that increase the conductivity

In OPTP we monitor the change in transmission (ΔT) of the THz probe pulse due to photoexcitation. At a defined delay (t) between the pump and probe, the $\Delta T(t)$ signal is obtained by modulating the pump pulse using a chopper set to half the repetition frequency of the probe and calculating the difference in transmission between the pumped and un-pumped sample. The OPTP technique allows us to easily monitor the photogenerated carrier dynamics by fixing the probe pulse at the peak amplitude of the THz electric field (T_{max}) (in Figure 2.5, T_{max} would be the peak of the transmitted pulse (black trace at 0ps)). We then vary the delay between the pump and THz probe to obtain the frequency averaged change in photoconductivity. For a thin film where the thickness (L) $\ll \lambda$, provided there is a negligible change in phase on photoexcitation, the average change in photoconductivity $\Delta\sigma(t)$ at a pump-probe delay (t) can be related to $\Delta T(t)/T_{max}$ according to the equation[18] Eq. 2.5.
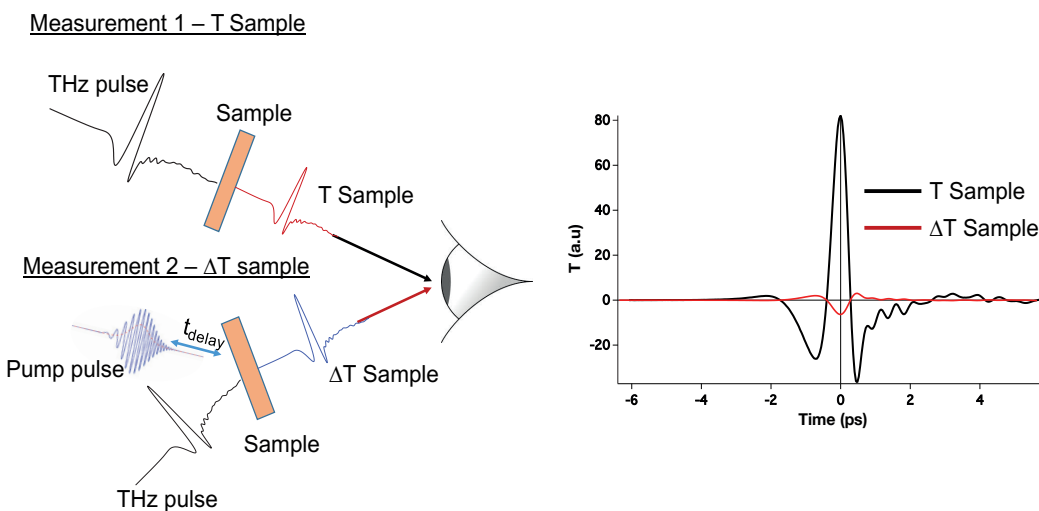
Figure 2.5 - Schematic of the measurements undertaken to obtain the photoconductivity of the sample. Linear scans of the transmission of the THz pulse through the dark sample and the photoexcited sample are illustrated in the figure to the right

$$\Delta\sigma(t) = \frac{(n_a + n_b)\varepsilon_0 c}{d} \frac{\Delta T(t)}{T_{max}}$$ **Eq. 2.5**

Where ε_0 is the permittivity of vacuum, c the speed of light, d the penetration depth of the pump in the sample, n_a and n_b are the refractive indexes of the materials that surround the sample. n_a and n_b are usually the index of vacuum ($n_a = 1$) and the quartz substrate ($n_b = 2.13$).

In addition to the frequency averaged photoconductivity dynamics we can also measure the spectrally resolved photoconductivity. The frequency resolved photoconductivity spectra can be obtained by placing the chopper in the path of the pump, fixing the pump-probe delay (t) and then scanning the gating beam to obtain the complete modulation of the THz pulse in time. This gives us the $\Delta T(t, \tau)$ of the THz pulse in time (τ) (measurement 2 in Figure 2.5), which is the difference in transmission between the excited sample $T_{s,ex}(t, \tau)$ and the unexcited sample $T_s(\tau)$. We then record the THz pulse passing through an unexcited sample to have the transmission $T_s(\tau)$ in the dark (measurement 1 in Figure 2.5). With which we can calculate the complex photoconductivity $\sigma(\omega,t)$ of the sample. If the variation the complex conductivity response of the sample due to the pump pulse is insignificant relative to the oscillation period of the THz pulse i.e. the leading edge of the THz pulse experiences the same conductivity response relative to the trailing edge (there is no rapid change in conductivity
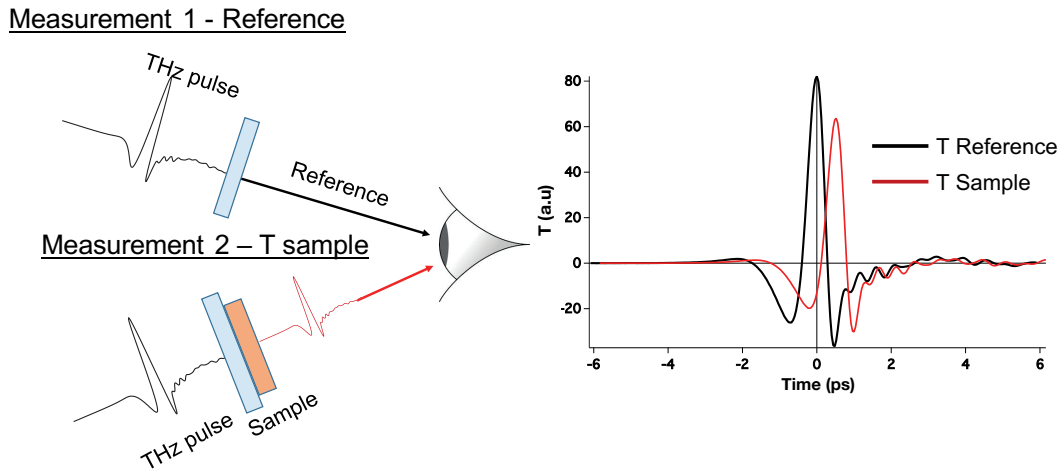
Figure 2.6 – Schematic of the measurements undertaken to obtain the dark materials parameters. Linear scans of the transmission of the THz pulse through the reference and sample are illustrated in the figure to the right**.**

due to charge carrier formation, trapping, cooling or recombination), then a steady state approximation can be used to obtain complex conductivity spectrum σ(ω) using the Fourier transformed $\Delta T(\omega)$ and $T(\omega)$ acording to:

$$\Delta\sigma(\omega) = -\frac{(n_a + n_b)\varepsilon_0 c}{d}\frac{\Delta T(\omega)}{T(\omega)} \qquad \textbf{Eq. 2.6}$$

The complex refractive index and permittivity of the sample can also be obtained by measuring the linear scan of the transmission of the THz pulse passing through the reference substrate (measurement 1, Figure 2.6) and the THz transmission through the sample in the dark without photoexcitation (measurement 2, Figure 2.6).

The complex refractive index η^* is defined by:

$$\eta^* = \eta + i\kappa \qquad \textbf{Eq. 2.7}$$

where η is the refractive index of the material ($\eta = c / v$, here v is the velocity of light in the film) and the imaginary part of η^* is related to the extinction coefficient (κ) of the material (the relationship to the absorption coefficient of the material is provided by $\alpha = 4\pi\kappa/\lambda$). The absorption coefficient and the refractive index of the material are related to the power, P, and phase, ϕ, of the Fourier transform of the scans taken of the sample and the reference substrate through [19]:

$$\alpha = -\frac{1}{d}\ln\left(\frac{P}{P_0}\right) \qquad \textbf{Eq. 2.8}$$

$$n = 1 + \frac{c}{2\pi\omega d}(\phi - \phi_0) \qquad \textbf{Eq. 2.9}$$

Where P and ϕ are the Fourier transforms of the scans through the sample and P_0 and ϕ_0 through the reference substrate.

The complex refractive index η^* and complex relative dielectric function ε^* are related by:

$$\eta^* = \sqrt{\varepsilon^*} \qquad \textbf{Eq.2.10}$$

For the complex permittivity, the real, ε', and imaginary part ε'' are calculated by [19]:

$$\varepsilon' = n^2 - k^2 \text{ and } \varepsilon'' = 2nk \qquad \textbf{Eq. 2.11}$$

2.5 Bibliography

1.   Gulbinas, V., Kananavičius, R., Valkunas, L. & Bässler, H. Dynamic Stark effect as a probe of the evolution of geminate electron-hole pairs in a conjugated polymer. *Phys. Rev. B* **66,** 233203 (2002).

2.   Cabanillas-Gonzalez, J. *et al.* Photoinduced Transient Stark Spectroscopy in Organic Semiconductors: A Method for Charge Mobility Determination in the Picosecond Regime. *Phys. Rev. Lett.* **96,** 106601 (2006).

3.   Devižis, A., Serbenta, A., Meerholz, K., Hertel, D. & Gulbinas, V. Ultrafast Dynamics of Carrier Mobility in a Conjugated Polymer Probed at Molecular and Microscopic Length Scales. *Phys. Rev. Lett.* **103,** 027404 (2009).

4.   Devižis, A. *et al.* Dissociation of Charge Transfer States and Carrier Separation in Bilayer Organic Solar Cells: A Time-Resolved Electroabsorption Spectroscopy Study. *J. Am. Chem. Soc.* **137,** 8192–8198 (2015).

5.   Risse, J. N. D. J. Ultrafast dynamics of photoinduced charge separation in cyanine- and polymer-based organic photovoltaic systems. (2015). EPFL- thesis (6627)

6.   Exter, M. V., Fattinger, C. & Grischkowsky, D. Terahertz time-domain spectroscopy of water vapor. *Opt Lett* **14,** 1128–1130 (1989).

7.   Jepsen, P. U., Cooke, D. G. & Koch, M. Terahertz spectroscopy and imaging - Modern techniques and applications. *Laser & Photon. Rev.* **5,** 124–166 (2010).

8.   Qi Wu & Xi-Cheng Zhang. Design and characterization of traveling-wave electrooptic terahertz sensors. *IEEE Journal of selected topics in quantum electronics* **2,** 693–700 (1996).

9.   Groeneveld, R. & Grischkowsky, D. Picosecond time-resolved far-infrared experiments on carriers and excitons in GaAs-AlGaAs multiple quantum wells. *JOSA B* (1994).

10.   Schall, M., Walther, M. & Jepsen, P. U. Phys. Rev. B 64, 094301 (2001) - Fundamental and second-order phonon processes in CdTe and ZnTe. *Phys. Rev. B* (2001).

11.   Hendry, E., Wang, F. & Shan, J. Electron transport in TiO_2 probed by THz time-

domain spectroscopy. *Phys. Rev. B* (2004).

12. Hegmann, F. A., Tykwinski, R. R., Lui, K. P. H., Bullock, J. E. & Anthony, J. E. Picosecond transient photoconductivity in functionalized pentacene molecular crystals probed by terahertz pulse spectroscopy. *Phys. Rev. Lett.* **89,** 227403 (2002).

13. Tiwana, P., Parkinson, P., Johnston, M. B., Snaith, H. J. & Herz, L. M. Ultrafast Terahertz Conductivity Dynamics in Mesoporous TiO$_2$: Influence of Dye Sensitization and Surface Treatment in Solid-State Dye-Sensitized Solar Cells. *J. Phys. Chem. C* **114,** 1365–1371 (2010).

14. Beard, M. C., Turner, G. M. & Schmuttenmaer, C. A. Transient photoconductivity in GaAs as measured by time-resolved terahertz spectroscopy. *Phys. Rev. B* **62,** 15764–15777 (2000).

15. Němec, H., Kužel, P. & Sundström, V. Charge transport in nanostructured materials for solar energy conversion studied by time-resolved terahertz spectroscopy. *Journal of Photochemistry and Photobiology A: Chemistry* **215,** 123–139 (2010).

16. Ulbricht, R., Hendry, E., Shan, J., Heinz, T. F. & Bonn, M. Carrier dynamics in semiconductors studied with time-resolved terahertz spectroscopy. *Rev. Mod. Phys.* **83,** 543–586 (2011).

17. Brauer, J. C. Linear and Time-Resolved THz Spectroscopy of Photonic and Charge Transporting Systems. (2012). doi:10.5075/epfl-thesis-5444

18. Nienhuys, H.-K. & Sundström, V. Intrinsic complications in the analysis of optical-pump, terahertz probe experiments. *Phys. Rev. B* **71,** 235110 (2005).

19. Dexheimer, S. L. Terahertz spectroscopy: principles and applications. (2007).

3 THz Spectroscopy of Hybrid Organic-Inorganic Perovskite Films

3.1 Introduction

In this chapter we investigate thin film perovskites using time-resolved THz spectroscopy. Hybrid organic-inorganic perovskites have emerged as one of the most promising active materials for new generations of photovoltaics[1,2] and a broad range of opto-electronic devices. The spectrally broad absorption of the semiconductor combined with the ability to transport both electrons and holes allows them to efficiently harness the solar spectrum and extract photogenerated carriers.[3,4] Their excellent optical and electronic properties have resulted in device efficiencies that rival established silicon based devices.[5] Despite this very rapid progress, much remains to be understood regarding the intrinsic properties of the material and the basic mechanisms of solar cell operation. Some of the key factors related to the performance of photovoltaic devices made from these materials are the nature of the photogenerated species, the efficiency of their transport across the device and the rates of loss mechanisms such as carrier recombination.

The dynamics of charge carriers created using an optical excitation pulse in the visible part of the spectrum (within the absorption spectrum of the material) are probed with

radiation in the THz domain. We are able to directly visualize the formation and loss of photogenerated carriers due to their interaction with the THz pulse. In addition to being able to selectively probe photogenerated charge carriers, THz spectroscopy allows us to simultaneously obtain information about the change in amplitude and phase of the THz probe pulse as it passes through the sample in its photoexcited or ground state. In this way we directly obtain the frequency dependence of the complex material parameters as well as vibrational interactions over the investigated THz frequency range.

Photoconductivity measurements using THz spectroscopy investigates the high frequency, nanoscopic conductivity of our sample films. Using this technique, we aim to obtain an understanding of the intrinsic properties of the perovskite in terms of their material parameters, such as microscale carrier mobility and carrier transport insights obtained from the complex conductivity spectrum. Since the measurements with the THz setup does not take into account the macroscopic movement of charges, we combine our THz investigations with EDA measurements (presented in subsequent chapters) that allow us to build a comprehensive understanding of the micro and macroscale carrier properties of the material.

We investigate two perovskite compositions: the first of which is the methylammonium ($CH_3NH_3^+$, MA) lead iodide perovskite ($MAPbI_3$), this composition was used in the seminal papers demonstrating high performance photovoltaic devices,[1,2] and used ubiquitously for fabrication of perovskite based optoelectronic devices and fundamental investigations during the first few years of the field. Recently, more complex perovskite alloys[6,7] that used mixed organic cations/halide anions and result in improved material

properties and film morphology have been synthesized. The second perovskite we examine is a mixed cation - Formamidinium ($CH=CHNH_3^+$, FA) / methylammonium and mixed halide - Iodide / Bromide alloy with the composition $(FAPbI_3)_{0.85}(MAPbBr_3)_{0.15}$.

To begin, the frequency averaged THz conductivity dynamics of the two perovskite compositions are measured. The fluence dependence of the dynamics allows us to obtain information on the deactivation pathways of the perovskite subsequent to photoexcitation. We combine our results with theoretical/experimental literature reports[8-13] and explain our observations using an indirect bandgap model for the perovskite. In which, carrier excitation occurs through a direct band gap transition, while deactivation proceeds through a combination of: slow, trap and indirect band gap recombination pathways at low carrier densities and a fast recombination pathway through a direct transition at elevated carrier densities. Subsequently bimolecular recombination rates and carrier mobilities, along with their dependence on temperature are calculated from the photoconductivity and the dynamics from the time-resolved measurements. Finally, the frequency resolved conductivity and dark THz spectra of our two films are investigated. Over the course of the discussion, we link our observations and calculated parameters to the characterized film morphology and photovoltaic device performance.

3.2 Experimental

3.2.1 Sample preparation

Perovskite samples prepared for THz spectroscopy were deposited on quartz substrates. Two perovskite compositions were investigated over the course of this thesis. The first - methylammonium lead iodide (MAPbI$_3$) and the second - a mixed halide (Iodide / Bromide) / mixed cation (FA / MA) perovskite (FAPbI$_3$)$_{0.85}$(MAPbBr$_3$)$_{0.15}$ (**which will be referred to as the mixed perovskite from here on**).

MAPbI$_3$ films: The films used in our measurements were fabricated by Dr. Joël Teuscher, the procedure is described as follows: A 155-nm-thick film of MAPbI$_3$ was coated on top of the quartz substrate by thermally coevaporating methylammonium iodide (CH$_3$NH$_3$I) and lead iodide (PbI$_2$) in a vacuum. Methylammonium iodide was synthesized and purified following a reported recipe.[14] PbI$_2$ (99%, Aldrich) was used as received. Substrates and chemicals were loaded in an evaporator chamber (custom-built, Lesker). The chamber was pumped down to a base pressure of 9×10^{-6} mbar. The methylammonium iodide source was contained in a molybdenum boat covered by a perforated lid (Omnicore). The CH$_3$NH$_3$I evaporation rate was adjusted with a proportional−integral−derivative (PID) controller conditioning the heating power supply with a pressure set point of 1.23×10^{-4} mbar. PbI$_2$ was placed in a quartz crucible heated by a tungsten wire coil (EVB9, EVC2, Lesker), and its evaporation rate was controlled with a quartz microbalance placed inside the chamber.[15] The rate of MAPbI$_3$ deposition

onto the substrate was 0.03 nm s^{-1}. Details on the evaporation setup and procedure are provided in reference.[16]

Mixed perovskite film: The mixed perovskite films were prepared by Dr. Juan-Pablo Correa-Baena and the description of the deposition procedure has been adapted from ref [17]. The perovskite films were deposited from a precursor solution containing FAI (1 M), PbI$_2$ (1.1 M, TCI Chemicals), MABr (0.2 M) and PbBr$_2$ (0.2 M, Alfa Aesar) in anhydrous DMF:DMSO 4 : 1 (v/v, Acros). The perovskite solution was spin-coated in a two-step program; first at 1000 rpm for 10 s and then at 4000 rpm for 30 s. During the second step, 100 μL of chlorobenzene were poured on the spinning substrate 15 s prior to the end of the program. The substrates were then annealed at 100°C for 1 h in a nitrogen filled glove box. The sample thickness as determined from the UV-Vis absorbance of the film on quartz was 560nm.

3.2.2 Film and device characterization

Cross sectional SEM images were obtained in collaboration with Dr. Ibrahim Dar, the JV curves for devices made with evaporated MAPbI$_3$ film were provided by Dr. Joël Teuscher and the JV curves for devices made with the mixed perovskite were done in collaboration with Dr. Juan-Pablo Correa Baena.

A ZEISS Merlin HR-SEM (Scanning electron microscope) was used to characterize the morphology of the device cross-section. Devices made using the perovskite active layers were measured using a 450 W xenon light source (Oriel). The spectral mismatch

between AM 1.5G and the simulated illumination was reduced by the use of a Schott K113 Tempax filter (Prazisions Glas & Optik GmbH). The light intensity was calibrated with a Si photodiode equipped with an IR-cutoff filter (KG3, Schott) and it was recorded during each measurement. Current–voltage characteristics of the cells were obtained by applying an external voltage bias while measuring the current response using a digital source meter (Keithley 2400).[17]

3.2.3 THz spectroscopy

The THz spectroscopy system used for our measurements has previously been described in section 2. Our measurements have been conducted using a pump pulse generated by an optical parametric amplifier, with the wavelength tuned to 560nm or 750nm depending on our desired excitation wavelength. The beam diameter was determined to be 3.3 – 3.8 mm with a beam profiler (BC 106-Vis, Thorlabs). The low temperature measurements were carried out in an optical helium cryostat (Oxford instruments). The measurements were carried out in dry box, which was purged with nitrogen to reduce the humidity to $\approx 5\%$.

3.3   Results and Discussion

3.3.1 Cross sectional SEM
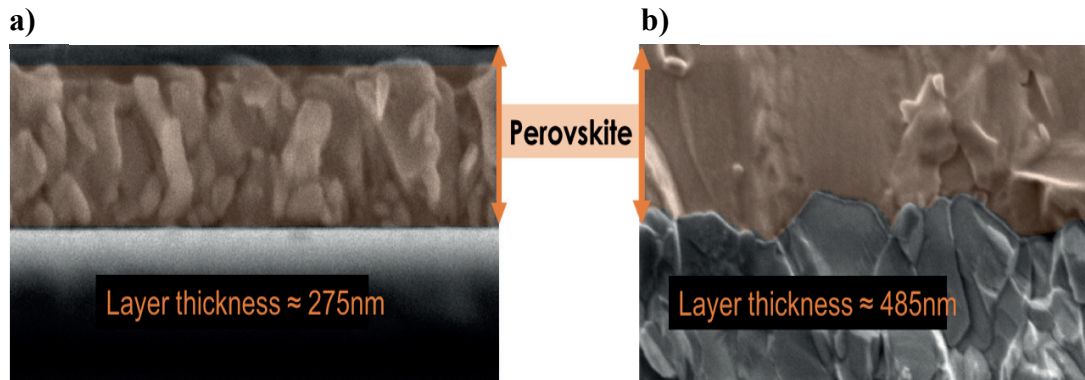
Figure 3.1 - Cross sectional SEM images for typical layers of our MAPbI$_3$ film (3.1a) and mixed perovskite film (3.1b). The perovskite layer has been shaded in brown to distinguish it from the substrate. The active perovskite layer shown in this figure are a part of the complete devices that are subsequently investigated in chapters 4 and 5.

Cross sectional SEM images of films of our two perovskite compositions are presented in Figure 3.1. For the MAPbI$_3$ we observed a morphology that was extremely granular with grain dimensions that were between 5 -100nm. The cross sectional SEM of the mixed perovskite showed it was homogeneous morphologically and had crystals that spanned the thickness of the film.

3.3.2 Device Performance

The performance of complete photovoltaic devices made using the two perovskite compositions were characterized. For the mixed perovskite sample, a planar device with the following architecture was used: $FTO|SnO_2|(FAPbI_3)_{0.85}(MAPbBr_3)_{0.15}$ |spiro-OMeTAD. The MAPbI$_3$ device had the following FTO|TiO$_2$| MAPbI$_3$|spiro-OMeTAD.

The typical current-voltage scans (J-V) for devices formed from the two investigated perovskite compositions are displayed in Fig 3.2. The MAPbI$_3$ based devices had a maximum power conversion efficiency (PCE) of 12.4%, with an open circuit voltage (V_{oc}) of 1.15V, short circuit current (J_{sc}) of 16 mA cm^{-2} and fill factor (FF) of 0.62. The mixed perovskite devices had a PCE of 17.9%, with a V_{oc} of 1.16V, J_{sc} of 22.4 mA·cm^{-2} and FF of 0.67.
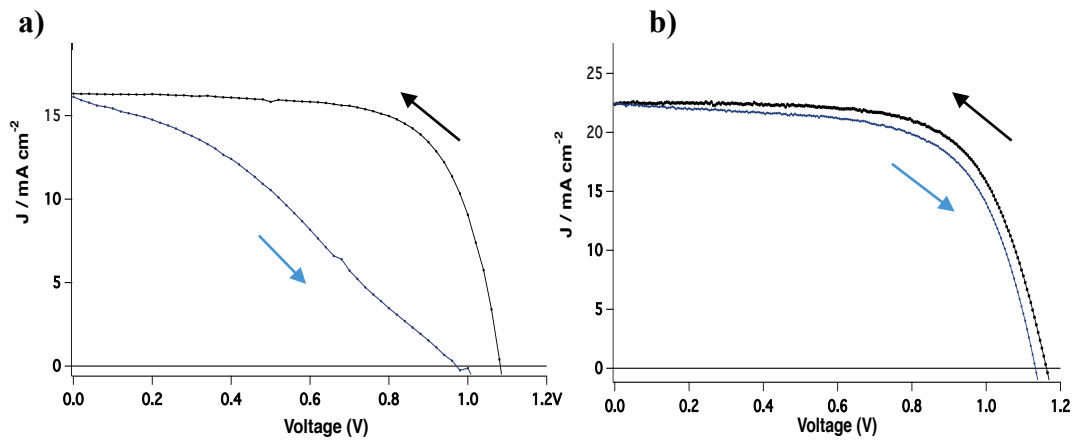

Figure 3.2 - JV scans for the devices made of MAPbI$_3$ (a) and mixed perovskite (b) device in the forward and reverse directions. The MAPbI$_3$ perovskite had a PCE of 12.4%, J_{sc} of 16mA · cm^{-2} and V_{oc} of 1.15 V. The mixed perovskite had an average PCE of 17.9%, J_{sc} of 22.38 mA · cm^{-2}, V_{oc} of 1.16 V and V_{pmax} of 0.9 V.

3.3.3 Charge carrier dynamics

There has been significant debate on the nature of the photogenerated species in perovskite based photovoltaic devices, in part surrounding whether photoexcitation resulted in the direct formation of free carriers, bound excitons or a mixture of the two.[18] Literature reports of the exciton binding energy in MAPbI$_3$ have varied between from 2meV up to as high as 50meV.[18-23] The general consensus now is that the binding energies are at the lower end of the estimated scale, with values for the exciton binding energy <16meV being the most likely.[20] This would mean that the binding energy is generally lower or similar to the thermal energies at room temperature where $k_bT \approx 25.7$ meV (at 298K). This indicates that the photo-excited species at room temperature is composed primarily of mobile charge carriers and not excitons, these charge carriers form either directly after photoexcitation or through splitting of a transient excitonic species. In addition, the large absorbance of the perovskite over the visible part of the spectrum coupled with the long lifetimes experienced by photogenerated charge carriers[24,25] has led to uncertainty over the nature of the recombination pathways that govern carrier relaxation. The strong absorbance of the perovskite allows for the fabrication of devices with an active layer thickness of around 500nm, which is around 1000 times thinner than the typical requirements for silicon based devices, where the fundamental transition is indirect in nature (hence a weaker absorption which requires a thicker silicon layer). The lifetimes of the mobile, photogenerated carriers have been shown to be as long as 30μs in films.[24,26] Which leads to the question of how such large densities of charge carriers (due to the strong absorption) can exist in the film without recombination occurring at a

much more rapid rate. We attempt to answer these questions over the course of this chapter by investigating the early dynamics of charge carriers and identifying the fluence dependent mechanisms that govern the recombination processes. In our measurements, photo-excitation was carried out using an optical pulse with a wavelength tuned to 560nm or 750nm. The density of photo excited charge carriers formed by the excitation pulse can be controlled by modulating the pump fluence.

The early time scale, at t < 3ps after photoexcitation is shown in Fig 3.3 for excitation at low carrier densities, where there is no observable recombination dynamics over 1ns (Figure 3.3 inset). We observe a rise that can be associated with the formation of charge carriers which is complete in ≈ 1.1 ps and has a $t_{1/2}$ of ≈ 600 fs. The differential signal we observe on the frequency averaged optical pump – THz probe (OPTP) measurements are related to the photoinduced conductivity of the film and proportional to the charge carrier mobility and their density. Since the exciton binding energy is lower than the thermal
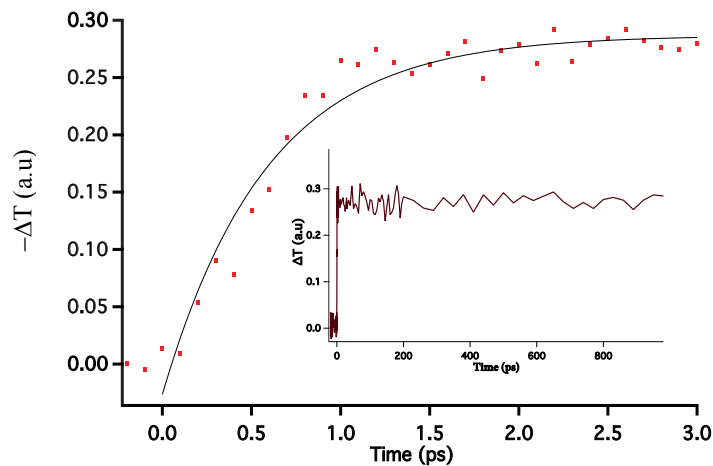
Figure 3.3 – Early OPTP dynamics for the mixed perovskite film with pump excitation at 560nm and a carrier excitation density of $2 \times 10^{18} \, cm^{-3}$. **Inset** – dynamics up to 1000ps

energy at room temperature, we expect our observed THz response to photoexcitation to be primarily due to free charge carriers. The species formed initially after photoexcitation can be assigned to an exciton, which is an electrically neutral quasiparticle and hence does not contribute to the photoconductivity probed using THz radiation. The transient excitonic species disassociates in 1.1 ps to form free charge carriers and is responsible for the observed rise in photoconductivity. Our results are in good agreement with previous literature reports on the exciton nature of the initial photogenerated species[27] and the timescales for its dissociation.[28,29]

Figure 3.4 shows the THz dynamics for excitation at different excitation densities for both the mixed and MAPbI$_3$ perovskite films. For the MAPbI$_3$ sample, fluence dependent measurements were carried out at two excitation wavelengths, 560nm and 750nm. Excitation at 750nm is near the absorption edge of our measured sample and results in the excitation of electrons from the valence band to the conduction band with very little excess energy. Whereas with 560nm we excite carriers into states significantly above the conduction band edge. For the dynamics at low excitation fluence, in both the mixed perovskite and MAPbI$_3$, we see that there is no observable change in the amplitude of the THz signal between 1 - 1000ps after an initial rise following photoexcitation. In MAPbI$_3$ we see this for both excitation wavelengths (560 and 750nm). This indicates that at low excitation densities, after the formation of free charge carriers, there is no change in the carrier mobility or the carrier density due to loss mechanisms such as recombination or trapping. The lifetimes of these long lived charge carriers have been previously

determined to be 10-100μs[24] and the recombination mechanism was proposed to be predominantly trap assisted at low excitation densities.[30]

However, theoretical calculations[8,31-33] and experimental work[8,11,34] suggested that after photoexcitation, electrons and holes occupy bands which are shifted in k space relative to each other, resulting in an indirect relaxation pathway. The degeneracy of the conduction levels are broken due to spin orbit coupling (SOC), resulting in a splitting to form multiple bands.[35] With the formation of the indirect band due to an offset of the SOC split conduction band minimum (CBM) relative to the valence band (VB) in k space, due to the Rashba effect that results in a mismatch of the CBM and VB for momentum and spin,[13] both of which suppress the return of the carriers to the ground state. Walsh et al.[9] proposed that the mismatch in momentum is the dominant effect in suppressing carrier recombination rather than the spin mismatch.

At higher excitation densities, we see that there is an observable decay of the photoconductivity signal within our measured window. This decay could reflect a change in either, the mobility of the carriers and/or a reduction in the charge carrier density. There is unlikely to be a significant change in carrier mobility by increasing the excitation fluence, since we observe no change in the photoconductivity signal over time at low fluences. Rather the decay is likely to reflect a loss of carriers due to recombination process that are directly linked to the change in photogenerated charge carrier density.
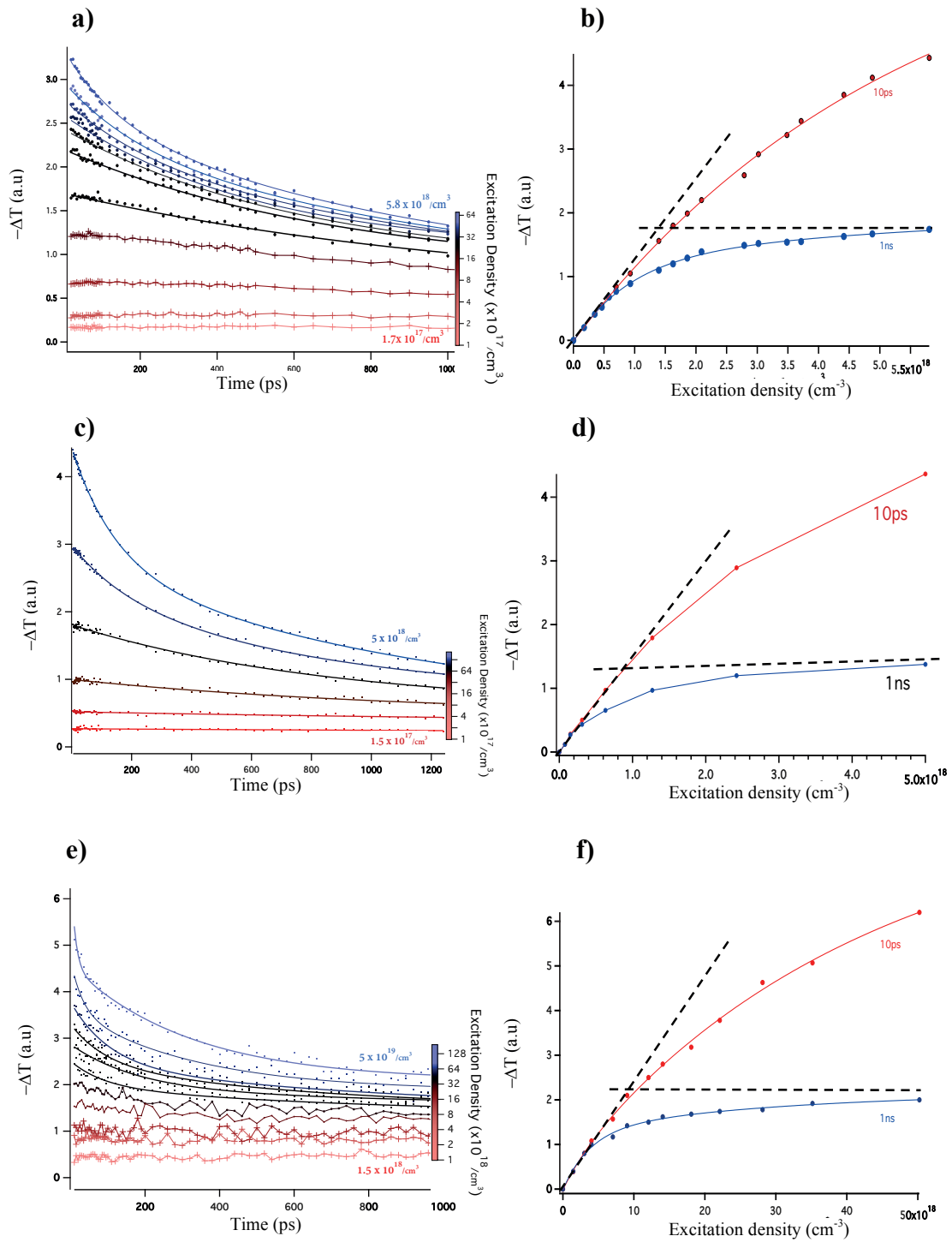
Figure 3.4 – OPTP dynamics are presented in figures **3.4 a), c) & e)** for different pump excitation fluences and **fig. 3.4 b), d) & f)** displaying the signal amplitude (ΔT) at 10ps and 1ns after photoexcitation. **Fig 3.4 a) & b)** are for the MAPbI$_3$ film with pump excitation at 560nm, **c) & d)** for MAPbI$_3$ with the pump at 750nm and **e) & f)** are the mixed perovskite film with excitation at 560nm.

In Fig 3.4 (b, d & f) we plot the amplitude of the $-\Delta T$ signal at 10 ps and 1 ns after excitation as function of the excitation density (n_0). At 10 ps, we plot the THz amplitude at its peak after photoexcitation, while at 1 ns we monitor the signal amplitude after its reduction due to carrier recombination at the limit of our measurement window. The excitation density at which the onset of carrier recombination occurs can be calculated at the point at which the amplitudes at 10 ps and 1 ns begin to diverge. For the tri-iodide perovskites, carrier recombination can be observed at carrier densities above 4×10^{17} cm^{-3} as observed in Fig 3.4b. Whereas for the mixed perovskite we see that recombination begins at excitation densities above 5×10^{18} cm^{-3} (Fig. 3.4f) which is an order of magnitude above that of the multi-grain MAPbI$_3$ perovskite. In addition, we see that for both types of perovskite at increasing carrier densities there is a plateau in the signal amplitude measured at 1 ns (dotted lines for the 1ns trace in Fig 3b, d & f) while the THz signal amplitude at 10 ps continues to grow with increasing excitation density. This reflects a convergence of the dynamics traces at higher excitation fluences with increasing time after photoexcitation.

In summary, our fluence dependent measurements show:

1) No carrier recombination within 1 ns at both excitation wavelengths for low excitation densities.

2) Carrier loss through recombination at higher carrier densities, which occurs in ≈ 1 ns.

3)   Carrier recombination results in a reduction of the THz signal amplitude. The decay in signal amplitudes for the different fluences proceeds until the traces begin to converge at longer times ≈ 1 ns. Which reflects a carrier population density which can stably coexist at short timescales, and their recombination occurs at longer times > 1 μs.

4)   There is an order of magnitude difference between the onset carrier densities for fast recombination between the mixed perovskite and $MAPbI_3$ films.

Our observations indicate that at low excitation densities, the photogenerated charge carriers occupy states from which the rate of recombination is extremely low. Excitation above a certain threshold (n_{onset}) carrier density ($n_{onset} = 4x10^{17}$ cm^{-3} for $MAPbI_3$ and $5x10^{18}$ cm^{-3} for the mixed perovskite) results in the loss of carriers through recombination, until the carrier population once again returns to a value that is stable over the nanosecond timescale. Based on these observations we determine that two primary recombination regimes exist: a slow one (k_{slow}) that is present at excitation densities $n < n_{onset}$ with carriers exhibiting lifetimes > 1 μs in this regime[23,24] and a fast regime (k_{fast}) at $n > n_{onset}$, where recombination reduces the carrier population within 1ns until $n \approx n_{onset}$. A significant part of this recombination happens within our accessible 1ns time scale, however we observe a portion of the recombination falls just outside our measurement window so we do not see the carrier density reach $n = n_{onset}$ exactly.

Based on the wavelength dependent measurements for the $MAPbI_3$ film, we see that nature of carrier recombination (k_{fast} and/or k_{slow}) does not depend significantly on the excitation wavelength (between the two investigated wavelengths). Excitation of carriers

with a pump wavelength of 750nm, which is just above the band gap, results in similar dynamics to those observed with excitation at 560nm. This tells us that carriers with significant surplus energy provided by excitation at 560nm have similar recombination pathways and lifetimes as those excited nearer to the band edge with minimal excess energy. The primary determinant of whether a k_{fast} component exists is the initial density of excited carriers rather than the excess, above band gap energy these carriers have at excitation.

The perovskite films we investigate demonstrate high, ambipolar carrier mobilities and devices made from these films have high power conversion efficiencies. This implies that carriers occupy bands within which they are mobile and carrier transport to the extracting interface is efficient. This would indicate that the significant portion of carriers formed after photoexcitaion have long lifetimes while also having high mobility and hence are not localized within deep trap states. However, time resolved measurements of carrier dynamics at longer, microsecond time scales have found mono-molecular recombination dynamics associated with trap mediated carrier recombination.[25,28,30,36,37] Wu et al.[38] showed that the trap states were excitonic in nature in the bulk perovskite films, with the density of these excitonic traps increasing as the dimensions of the crystals were reduced from 3 to 2-dimensional perovskite sheets. Other experimental techniques such as spatially resolved fluorescence microscopy by deQuilettes et al.[39] have found microstructure dependent defects which contribute to trap assisted carrier recombination.

Our observed dynamics could be explained by photogenerated carriers that exist in either:

1) one of two distinct bands, within which either fast or slow recombination pathways are dominant, and their occupation is dependent on the density carriers or / and;

2) carriers that relax into trap states from which recombination occurs slowly. Complete filling of these trap states with increasing excitation density results in a surplus of carriers that remain in the conduction band and undergo fast recombination with their oppositely charged counterpart.

While it is likely that trap states exist at grain boundaries and defects within the grain, the majority of carriers that are formed in high performance films/devices at all excitation fluences would generally be present as freely mobile carriers and not immobilized at these trap states. So the density of traps states alone would not account for the fluence dependent dynamics we observe.

In addition, if the generated carriers relaxed into trap states, then the n_{onset} value we determined would serve as a characteristic value for the density of these trap states. However, the observation of a higher n_{onset} for the mixed perovskite than $MAPbI_3$ is incompatible with the significantly higher device performance we observe for the former. Hence, our observations are better explained by a combination of trap mediated recombination and the existence of two bands with significantly different rates of carrier recombination.

The trap state density is heavily influenced by processing conditions which determine the morphological quality of the film and quality of the individual perovskite crystals that form the film;[16,39] resulting in a range of trap state densities depending on the fabrication conditions. This would explain the significant variations in the modelled contribution that trap states have to the experimentally observed recombination dynamics reported in literature.[13,30] Our observations would also imply that the long carrier lifetimes are an intrinsic property of the material and not dependent on the morphological quality. This would support our observation of long lived carriers in both the mixed perovskite with large crystals and the granular, polycrystalline films of $MAPbI_3$ with significantly larger trap states at the grain boundaries.

3.3.4 Band model

The existence of an indirect band conduction band ($CB_{indirect}$) was theoretically predicted[8,10,32,33] to occur through Rashba splitting of the conduction/valence bands. The presence of an indirect transition between the CBM and VBM would fit with the slow recombination dynamics we observe. In addition, a second transition which is direct in nature, through overlap of the CB and VB in k space, would explain the significantly faster recombination kinetics. At low fluences our results show that carrier recombination is entirely due to the k_{slow} pathway, regardless of the excitation wavelength. The excitation of carriers by high energy photons at 560nm would be a direct transition in to the conduction band[9] and they subsequently thermalize into $CB_{indirect}$. For excitation near the band edge (750nm) it is unclear whether the transition is initially direct, with thermal energy being sufficient to overcome the activation energy for carrier transfer to $CB_{indirect}$;

or if simultaneous carrier coupling with a photon and phonon results in the primary excitation near the band edge being indirect in nature.

Carriers residing in the indirect band would face a momentum forbidden recombination pathway. In order for recombination to happen, they would either have to couple with a phonon to provide the required momentum for the transition to occur or proceed through defect sites within the crystal or at grain boundaries. This phonon mediated recombination process would take place at a significantly slower rate than the direct recombination of carriers from CB_{direct}. Savenije et al.[11] calculated an activation energy of 47meV for transfer between the direct and indirect bands suggesting that thermal energy might assist the transfer from the indirect to direct bands, and slow recombination occurs through this pathway.

Our fluence dependent dynamics can be explained by the filling of states in $CB_{indirect}$ with increasing excitation densities. With the progressive filling of $CB_{indirect}$, occupation of the indirect band becomes less energetically favourable and surplus carriers begin to occupy states in CB_{direct}. Carriers in the direct band undergo recombination at a significantly higher rate due to the overlap of the CB and VB in k space. The population of CB_{direct} is depleted until the remaining carrier density is the sum of those occupying $CB_{indirect}$ ($n_{indirect}$) + trap states (n_{trap}) i.e. $n \approx n_{onset}$. The possible relaxation pathways at high and low fluences are illustrated in the free energy state diagram in figure 3.5. Figure 3.6 illustrates the offset of the conduction band in k space and the filling of the indirect band with increasing excitation density.
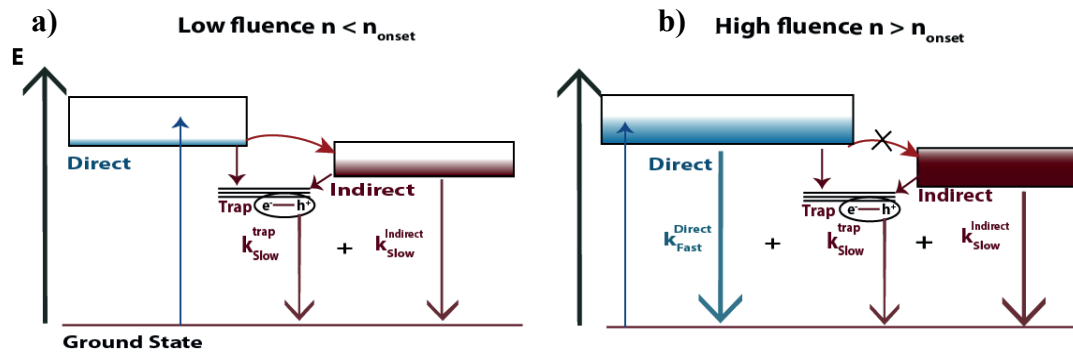
Figure 3.6 – Free-energy state diagram illustrating recombination pathways at low (a) and high (b) carrier densities. At low carrier densities recombination proceeds through the two slow pathways (Trap and Indirect). At high carrier densities recombination proceeds through the two slow pathways, in addition the fast recombination pathway which is direct in nature is also visible.
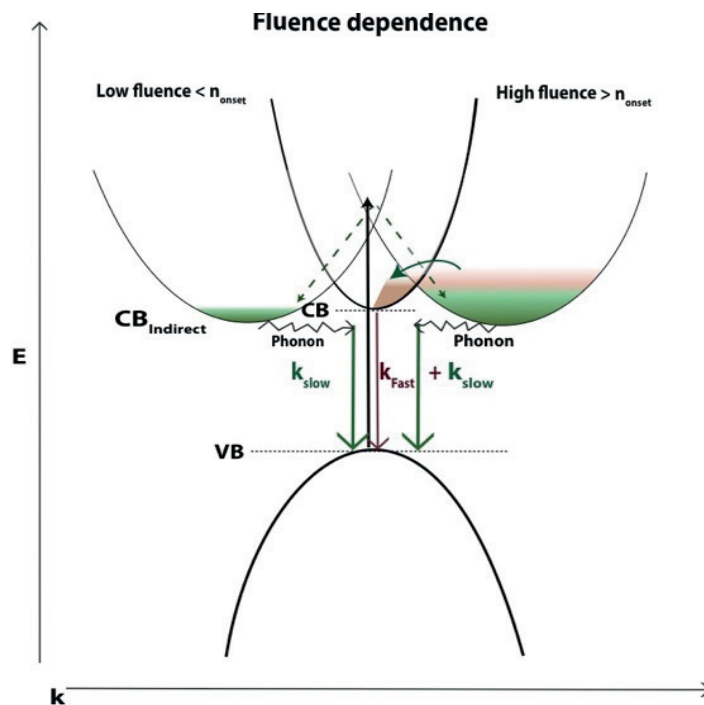
Figure 3.6 – Schematic band diagrams displaying filling of the direct and k-space shifted indirect band and recombination pathways at low fluence (left part of figure) and high fluence (right). The initial absorption of photons at 560nm occurs between band at the same k values and hence is direct in nature. At low fluences, carrier recombination from the indirect band is forbidden due to the momentum mismatch and requires coupling with a phonon for recombination to occur. At high fluences carrier recombination can also proceed through the direct band, the overlap of the CB and VB in k-space allows this process to occur at a quicker rate without the assistance of a phonon to provide the required momentum.

The n_{trap} value is highly dependent on the processing conditions.[15,17,39-41] Significant effort has been directed over the last years to improve film morphology by forming larger grains[42,43] that facilitate the transport of carriers across the film; passivation of grain boundaries[44] that act as recombination centres, as well as improving the quality of the formed crystals through fewer internal defects. The goal being to reduce loss pathways, while assisting the transport and extraction of photogenerated carriers at the electrodes. The reduction in the density of trap states would preserve the carrier population in $CB_{indirect}$ by restricting possible relaxation pathways and ensuring carriers remain in the indirect band until extraction. This however would not change the value of $n_{Indirect}$, above which carriers begin to occupy CB_{direct} and fast recombination occurs.

The $n_{Indirect}$ value would be an intrinsic property of the material whose upper limit could not be raised through improvements in the quality of the perovskite crystal or macroscale film morphology. Modification of the chemical composition of the perovskite would however provide an avenue to affect the materials intrinsic properties. The Spin orbit coupling that results in the splitting of the conduction levels in the perovskite is present in crystals without inversion symmetry. The disorder that is caused by partial substitution of the cation and halides in the $MAPbI_3$ composition to form an alloy, would result in further breaking of the symmetry and is expected to enhance the effects of SOC.[9]

Our fluence dependent measurements show an n_{onset} value is approximately an order of magnitude higher in the mixed perovskite film, $(FAPbI_3)_{0.85}(MAPbBr_3)_{0.15}$, than $MAPbI_3$. The improved film morphology of the mixed perovskite film would result in fewer grain boundaries that act as trapping sites. The expected reduction in n_{trap} would also reduce

the n_{onset} value if $n_{indirect}$ stayed constant. However, we see a large increase in n_{onset} for the mixed perovskite, that shows that alloying of the perovskite does modulate $n_{indirect}$. This occurs due to additional symmetry breaking caused by compositional disorder of the occupational sites enhancing the spin-split indirect gap.[9] This could manifest as a change in the energetic position of the indirect band relative to CB_{Direct}, which increases the number of states that can be occupied before their filling becomes energetically unfavorable; or a change in the curvature of $CB_{Indirect}$ that results in an increase in the density of states (in both cases the value of $n_{Indirect}$ would increase.)

The ability to sustain a large density of free charge carriers under constant illumination is a fundamental requirement for a photovoltaic material. And our results show that the mixed ion perovskites support a significantly higher carrier density before the onset of bimolecular recombination. Carrier densities of $\approx 10^{17}$ cm^{-3} are typical for an operating solar cell[9] and the mixed perovskites, which can support densities of $\approx 5 \times 10^{18}$ cm^{-3} are comfortably away from the threshold for fast, direct band recombination. This provides direction for future work to move beyond improving the morphological quality of the films to engineering the composition of the material to achieve improved device performance.

3.3.5 Bimolecular recombination rates

In our time resolved measurements at room temperature, we see either two or three recombination regimes depending on the excitation fluence. At low excitation energies we see a long lived component that is expected to be first order, monomolecular recombination assisted by shallow or excitonic traps[23,30,38,45] or through phonon mediated recombination from the indirect band.[8,10,32] Beyond a certain excitation threshold (4 x 10^{17} cm^{-3} for $CH_3NH_3PbI_3$ and 5 x 10^{18} cm^{-3} for mixed ion perovskites), we see charge carrier recombination occurring within our 1 – 1000 ps measurement window. In this high fluence regime, carrier recombination occurs through higher order pathways such as bimolecular recombination (which is second order) or Auger recombination (third order). Bimolecular processes occur through the band-to-band recombination of mobile electrons and holes and would be a second order process that depends on the carrier density. In Auger recombination, three charge carriers are simultaneously involved. Energy and momentum from the recombination of two carriers is transferred to a third carrier and would hence be a third order recombination process.

The recombination process we observe within our investigated time window are predominantly bimolecular in nature over our investigated excitation fluence range. This is reflected in the decay dynamics which can be divided into two components, a fast decay in < 1 ns and a slow decay component which shows no dynamics in our investigated window. However, at the highest excitation fluence used for the mixed ion perovskite, for a carrier excitation density of ≈ 5 x 10^{20} cm^{-3} (Figure 3.4e), we see two distinct decay components within 1 ns. The faster of the two components decays in < 20 ps and can be

associated with Auger recombination of free charge carriers, due to its third-order dependence with excitation intensity that has been reported.[46] While the second component can be assigned to the bimolecular recombination of free carriers.

In order to extract the bimolecular rate constant a second order rate equation can be applied. The rate of recombination would depend on the concentration of both electrons and holes. At high excitation densities, where the carrier density that recombines through the direct transition is significantly larger than $n_{indirect}$ and n_{trap}, we can approximate that the concentration of e_{cb}^- & h_{Vb}^+ are similar and equivalent to the number of photons absorbed. The change in carrier concentration with time for a second order process is then given by the rate equation:

$$\frac{d[n]}{dt} = k[n]^2 \qquad \textbf{Eq. 3.1}$$

where n is the concentration of carriers and k is the recombination coefficient of the bimolecular process. The integrated form of Eq. 3.1 equation leads to:

$$\frac{1}{[n]_t} = \frac{1}{[n]_0} + kt \qquad \textbf{Eq. 3.2}$$

Where n_0 is the initial carrier concentration and n_t is the concentration after a time t. Plotting n_t^{-1} as a function of time allows us to calculate the coefficient (k) of the second order kinetics from the gradient.

a)

b)
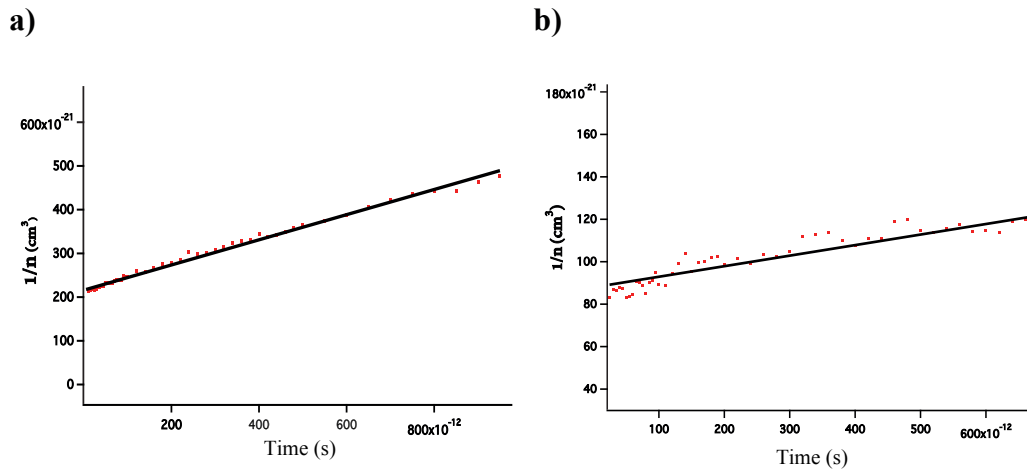
Figure 3.7 – n^{-1} vs. time for MAPbI$_3$ (a) and mixed (b) perovskite calculated from the initial carrier density of 4.8×10^{18} cm^{-3} (MAPbI$_3$) and 1.2×10^{19} cm^{-3} (Mixed), the straight lines are the second order kinetics from Eq. 3.2

Figure 3.7 shows n_t^{-1} against time for the mixed and MAPbI$_3$ perovskites. The solid line in figure 3.7 corresponds to the fitted second-order kinetics of Eq. 3.2. The inverse concentration against time is linear in figure 3.7, indicating that for the plotted initial carrier densities, bimolecular recombination processes are the primary deactivation pathway at times < 1 ns. We can ignore the trap assisted first order monomolecular recombination contribution, since they take place at much longer timescales as evidenced by the flat dynamics we see at low excitation densities. We obtain a second order recombination coefficient of 3.2 x 10^{-10} cm^3 s^{-1} for multi-grain CH$_3$NH$_3$PbI$_3$ films and a coefficient of 5 x 10^{-11} cm^3 s^{-1} for the mixed perovskite. Both perovskite compositions exhibit extremely low carrier recombination coefficients that are comparable to inorganic crystalline semiconductors such as GaAs.[47]

Our measured recombination coefficient values are also confirmed by those obtained using other techniques: Y.Chen et al.[48] used Hall effect and photoconductivity measurements to obtain bimolecular recombination coefficients between $10^{-10} - 10^{-11}$ cm^3 s^{-1}. Savenije et al.[49] obtained second order coefficients of 1.3 x 10^{-11} cm^3 s^{-1} using time-resolved microwave conductivity. Wehrenfennig et al. obtained bimolecular recombination rates of 8.7 x 10^{-11} cm^3 s^{-1} using a similar OPTP technique.

The bimolecular recombination rates reported across literature have been fairly consistent over a range morphology. Indicating that the process, as expected, is not dependent on trap states at grain boundaries or within defects in the crystal. Rather the measured value is likely to be intrinsic to the material and hence would show very little dependence on the morphology. Our measured bimolecular rate constants do however show a difference between our two perovskite compositions. With the mixed ion perovskite showing a lower bimolecular recombination rate while also being able to sustain a considerably higher density of carriers before the onset bimolecular recombination process relative to $MAPbI_3$.

3.3.6 Carrier mobility at THz frequencies

In the low fluence regime we see a linear dependence of the THz signal amplitude with excitation density. At higher excitation fluences we observe a deviation from linearity when looking at the 10 ps trace in Fig.3.4 b, d & f. Indicating that recombination at short time scales < 10 ps reduces the carrier population or that the valence band is significantly depleted of carriers, hence there are fewer carriers that can be excited to the conduction

band. We observe a negligible phase change upon photoexcitation (Appendix 3.1), so the frequency averaged photoconductivity ($\Delta\sigma$) over the penetration depth of the optical pulse can be related to the $\Delta T/T$ signal through equation Eq 2.5. Charge carrier mobilities are a more practical material characteristic than the photoconductivity and can be extracted from the frequency averaged photoconductivity THz using Eq. 3.3.[50]

$$\phi\mu = \frac{\Delta\sigma}{en_\pm} \qquad \textbf{Eq. 3.3}$$

Where e is the elementary charge and $n_\pm$ is the calculated density of electrons + holes, and ϕ is the generation efficiency of a carrier pair for each absorbed photon. For our calculations we assume a charge carrier generation rate of unity, a value that is less would mean the carrier mobility is actually higher than what we calculate. In addition, our THz mobility measurements give average values that does not distinguish between the mobility of electrons and holes.[50]

In order to obtain accurate mobility values, we use values for $\Delta\sigma$ at low fluences, where there is no change in the photoconductivity due to carrier recombination. The average calculated mobility at low fluences for MAPbI$_3$ is 41 $\pm$ 3 cm^2 V^{-1} s^{-1} and 22 $\pm$ 4 cm^2 V^{-1} s^{-1} for the mixed ion perovskite. Interestingly, we obtain higher carrier mobility for the multi-grain MAPbI$_3$ perovskite which has a poorer device performance (12%) relative to large grain mixed perovskites (18%). The carrier mobility measured with OPTP spectroscopy are generally the upper limit values for carrier mobility, due to the high frequency of the probe, carrier mobility is measured on a short length and time scale. Our observation of lower carrier mobility in films that form higher performance devices

suggest that the intrinsic carrier mobility is not the limiting factor for the performance of perovskite based photovoltaic cells. Rather, the device performance is limited in part by the density of carriers that can exist prior to the onset of fast bimolecular recombination and the rate of this loss pathway. These characteristics are determined by the density of carriers that occupy the $CB_{indirect}$ and the quality of the perovskite film in terms of grain boundaries, defects/traps in the crystal that act as recombination centres while also hindering the long range transport of charge carriers for extraction at their respective electrodes.

3.3.7 Temperature dependent carrier mobility

The temperature dependence of the carrier properties in $MAPbI_3$ and mixed perovskites have also been investigated using OPTP spectroscopy. In order to do this, we probed the photoconductivity of the perovskite films to obtain the temperature dependence of the carrier mobility and the bimolecular recombination dynamics.

The frequency averaged carrier mobility for a range of temperatures was calculated from the photoconductivity at 5ps after photoexcitation in a similar manner to the mobility at room temperature. A low carrier density of 1.5×10^{18} cm^{-3} was used, which was below the threshold for bimolecular recombination at room temperature. The
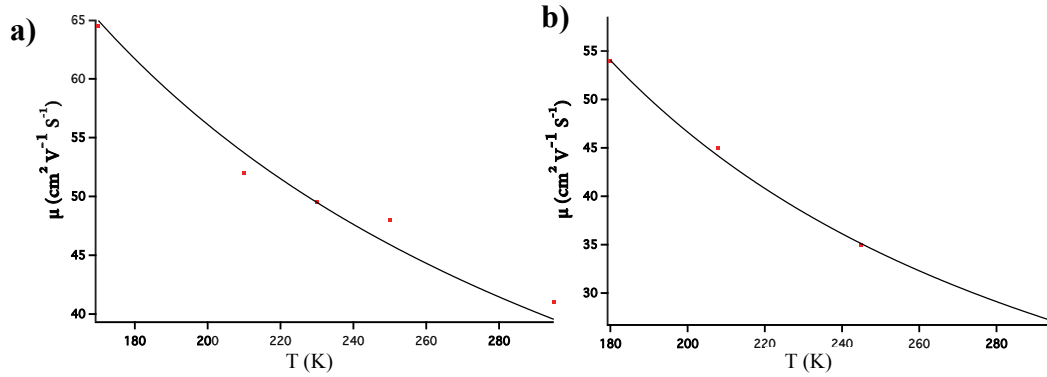
Figure 3.8 – mobility vs. temperature plot for MAPbI$_3$ (a) and the mixed perovskite (b). The points represent the experimental value and the line represents a power law fit with $\mu \propto T^{-0.9}$ for MAPbI$_3$ and $\mu \propto T^{-1.6}$ for the mixed perovskite.

mobility was calculated under the assumption that the carrier generation (ϕ) rate is constant and near unity with reducing temperature in the tetragonal phase of the perovskite (the tetragonal phase exists between T = 165 K to 327 K) [51]. The calculated mobilities are plotted against temperature in figure 3.8. A power law fit of μ against temperature (T) results in $\mu \propto T^{-1.6}$ for the mixed ion perovskite and $\mu \propto T^{-0.9}$ for MAPbI$_3$.

The scattering processes that have a dependence on the temperature are phonon scattering and scattering by ionized impurities. Carrier mobility is proportional to the average time between all scattering events, given by the relaxation time constant τ.

$$\mu = \frac{e}{m^*}\tau \qquad \textbf{Eq. 3.4}$$

According to Mathiessen's rule, the various scattering mechanisms are assumed to be independent of each other and the total relaxation time (τ) is a summation of the independent scattering mechanisms[52], given by:

$$\frac{1}{\tau} = \frac{1}{\tau_{phon}} + \frac{1}{\tau_{imp}} + \ldots \qquad \textbf{Eq. 3.5}$$

Where τ_{phon} and τ_{imp} are the temperature dependent carrier scattering processes due to phonons and ionized impurities. The relation of phonon and ionized impurity scattering with temperature is expected to be[53]:

$$\tau_{phon} \propto \mu_{phon} \propto T^{-\frac{3}{2}} \quad \text{and} \quad \tau_{imp} \propto \mu_{imp} \propto T^{+\frac{3}{2}} \qquad \textbf{Eq.3.6}$$

With μ_{phon} and μ_{imp} being the mobilities limited by phonon and charged impurity scattering. The relationship implies that the decrease in mobility with increasing temperature to be proportional to $T^{-\frac{3}{2}}$ for phonon scattering. As temperature rises, the increase in thermal vibrations would result in increased scattering and hence lower mobility. If carrier mobility is limited by ionized impurity scattering, the mobility rises with increasing T, with a $T^{+\frac{3}{2}}$ dependence. An increase in the average thermal speed of carriers with rising temperature would result in them spending less time near ionized impurity as they pass, reducing the effect of this scattering mechanism.

Zhao et al.[52] show the expected dependence of the carrier mobility as function of the temperature for different doping densities (Figure 3.9). Their calculations show that at low defect and doping concentrations carrier mobility is primarily determined through scattering by acoustic phonons (red line in figure 3.9). While at higher defect and doping
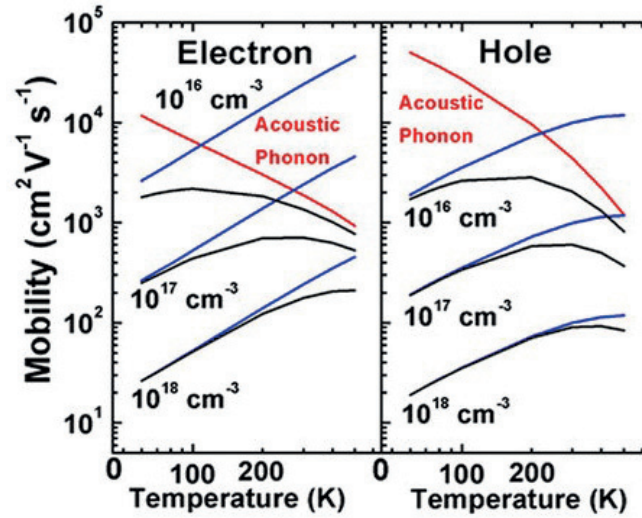
Figure 3.9 – The figure (taken from ref 52) represents theoretical calculations for the contributions of phonon scattering (red) and impurity scattering (blue) to the overall mobility (black) as a function of temperature for different defect/doping concentrations.

concentrations, the mobility is primarily limited by charged impurity scattering (blue line in figure 3.9). With the effective carrier mobility at a certain temperature being a combination of these two temperature dependent scattering contributions (black lines in figure 3.9).

Our results show that for the mixed ion perovskite, the change in mobility with temperature is $\propto T^{-1.6}$ and we can experimentally show that the carrier mobility is primarily limited by phonon scattering, which would result in a $\propto T^{-1.5}$ dependence. In MAPbI$_3$, the $\propto T^{-0.9}$ dependence we see, implies that μ depends on a mixture of phonon and charged impurity scattering. The total relaxation time would involve both τ_{phon} and τ_{imp}, with τ_{phon} having the larger contribution to the carrier mobility (τ_{phon} increases with decreasing T, while τ_{imp} increases with decreasing T).

In order to link our observations to the performance of devices made using the two perovskite films, we should emphasize the observed distinction between the two films. In the MAPbI$_3$ film, we see the charged impurity density is significant due to its influence on the carrier mobility in our temperature dependent measurements. Whereas, in the mixed perovskite film there is no visible contribution form charged impurities. The absence of these charged impurities could contribute to the reduction in hysteresis we observe in the current-voltage scans for these devices (figure 3.2). The slow migration of ions has been proposed as one of the reasons for the significant photocurrent hysteresis that has been observed in perovskite based devices, with ion migration under electric fields being mediated by defects that are present within the film, such as vacancies or interstitials.[54,55] In addition to these point defects, channels between grain boundaries have been proposed as pathways for the ion migration.[55,56] In MAPbI$_3$ films, the high density of charged point defects that are present within the crystal and at grain boundaries would be a source of charged impurity scattering of charge carriers while also contributing to the observed hysteresis. The improvements in the size and quality of the crystals we see in the mixed perovskite films would mean that they possess fewer defects, in addition to the reduction in grain boundaries due to larger crystals. A significant reduction in the number of charged defects would reduce the impurity scattering contribution as well as result in devices with less hysteresis.[55]

3.3.8 Temperature dependent recombination rates

In Fig 3.10a we see the carrier recombination dynamics at a high excitation density for two temperatures (295 K and 165 K) for the MAPbI$_3$ film. The increase in amplitude we observe with reducing temperature is due the increased carrier mobility (the photoconductivity signal is proportional to carrier mobility and density). Fig 3.10b plots the inverse carrier concentration (n_t^{-1}) vs. time to show the second order dynamics as previously described in Eq. 3.2. Fitting of the experimental results (with Eq. 3.2) allows us to extract second order recombination coefficients of 3.2 x 10^{-10} cm^3 s^{-1} at 295 K and 4.8 x 10^{-10} cm^3 s^{-1} at 165 K. We see that reducing the temperature leads to an increase in the rate of recombination. The observed increase in the recombination coefficient can be related to the rise in carrier mobility with decreasing temperature. Our temperature dependent recombination rates can be explained by the Langevin model for bimolecular
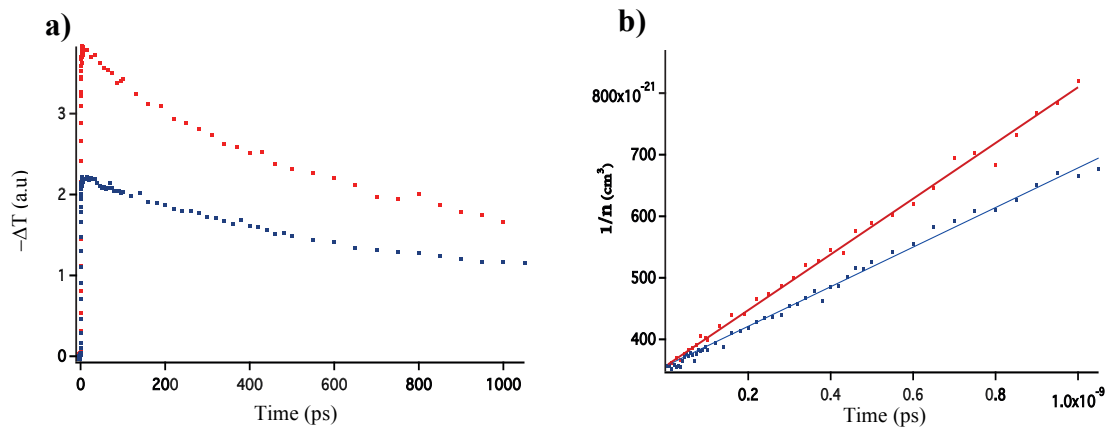
Figure 3.10 – a) shows the dynamics of MAPbI$_3$ at 295kel (Blue) and 165kel (red) for pump excitation at 560nm and a carrier density of 2.8 x 10^{18} cm^{-3} **b)** the points shows the change in inverse carrier density (n^{-1}) vs Time for 295K (blue) and 165K (red) calculated from the dynamics. The solid lines are the second order kinetics according to Eq 3.2.

recombination that had previously been used by Wehrenfennig et al.[25] to describe their observed recombination rates. In the Langevin theory the likelihood of a recombination event occurring is related to the probability of the oppositely charged carriers finding each other,[57] which is related to the carrier density and their mobility. The recombination rate constant according to the Langevin formalism is:[57]

$$k = k_{lan} = \frac{e\mu}{\varepsilon_0 \varepsilon_r} \qquad \textbf{Eq. 3.7}$$

Where μ is the mobility, ϵ_0 the vacuum permittivity, and ϵ_r the permittivity of the active layer. We observe that the rate of bimolecular recombination is proportional to the carrier mobility. Hence if $k \propto \mu$, the increasing mobility we observe with reducing temperature would result in an increase the recombination rate. Our temperature dependent mobility measurements for the MAPbI$_3$ showed a mobility of 41 cm^2.V^{-1}.s^{-1} at 295 K and 64 cm^2.V^{-1}.s^{-1} at 170 K. The ratio of the change in mobility is 1.56 (64/41), which matches the ratio of our calculated second order recombination coefficients of 1.5 (4.8x10^{-10} / 3.2x10^{-10}). This shows that the change in the recombination coefficients with temperature can be well explained by the related change in carrier mobility.

3.3.9 THz conductivity spectra

The frequency averaged conductivity measurements that have previously been presented were obtained by monitoring the change in transmission, at the peak amplitude of the THz pulse, as a function of time after photoexcitation. This allowed us to observe the dynamics of free carrier formation and recombination and calculate the carrier mobility from the change in photoconductivity. In addition to the frequency averaged conductivity measurements, we also carried out frequency resolved THz measurements within our experimentally accessible window of 0.3 - 2.4 THz. The spectral dependence of the photoconductivity and dark permittivity can provide valuable information about the nature of carrier transport in the investigated materials.

3.3.9.1   Drude-Smith conductivity models

A range of models have been used to analyze the conductivity spectrum depending on the nature of the generated carriers and the morphology of the investigated samples. Of these, the Drude model provides a simple description of the response of free carriers to the frequency of an applied electric field in photoexcited semiconductors or other conductive materials. The complex Drude conductivity, at frequency ω, is given by the equation:

$$\sigma(\omega) = \frac{\sigma_{dc}}{1 - i\omega\tau} \qquad \textbf{Eq. 3.8}$$

With τ being the scattering time for carriers that have been elastically scattered and σ_{dc}, is the dc conductivity given by:

$$\sigma_{dc} = \frac{ne^2}{m^*} = \omega_p^2 \tau \varepsilon_0 \qquad \textbf{Eq. 3.9}$$

In the above equation, n is the density of charge carriers, e the elementary charge, m^* the effective mass, ε_0 the vacuum permittivity and ω_p the carrier plasma frequency, which is given by:

$$\omega_p = \sqrt{\frac{ne^2}{\varepsilon_0 m^*}} \qquad \textbf{Eq. 3.10}$$

The conventional Drude model has been successful in describing homogeneous systems, where transport is dominated by free carriers across large crystalline domains.[58-60] The Drude-Smith model, which was developed by Smith has been able to effectively model deviations from Drude like conductivity that can occur in inhomogeneous systems where carrier transport is hindered by localization and scattering due to disorder.[61-63] A second Smith term is added, with a factor c_n, that modifies the Drude model to account for the retained carrier velocity after backscattering after n events. An assumption that the persistence of the velocity is retained only after the first collision (n = 1) allows the Drude-Smith equation to be simplified to:

$$\sigma(\omega) = \frac{\sigma_{dc}}{1 - i\omega\tau} * (1 + \frac{c}{1 - i\omega\tau}) \qquad \textbf{Eq. 3.11}$$

Where the c varies between $-1 < c < 0$. At $c = 0$ the conductivity is described purely by the classical Drude model. Increasing carrier backscattering is reflected by c values that become increasingly negative, varying from conductivity that is Drude like to one that is dominated by carrier backscattering for values of $c < -0.5$. In systems where the conductivity is dominated by carrier backscattering, the imaginary part of the conductivity is negative at low frequencies, which can be seen in Fig. 3.11 for values of $c < -0.5$. The conductivity becomes increasingly negative as the frequency increases before reaching its negative maximum. The real part of the conductivity, for $c = 0$ is at its maximum at DC conductivity and steadily decreases at higher frequencies. For $c < -0.5$, the real part of the conductivity increases at higher frequencies and peaks at $\omega\tau = 1$ for $c = -1$.

a)   b)
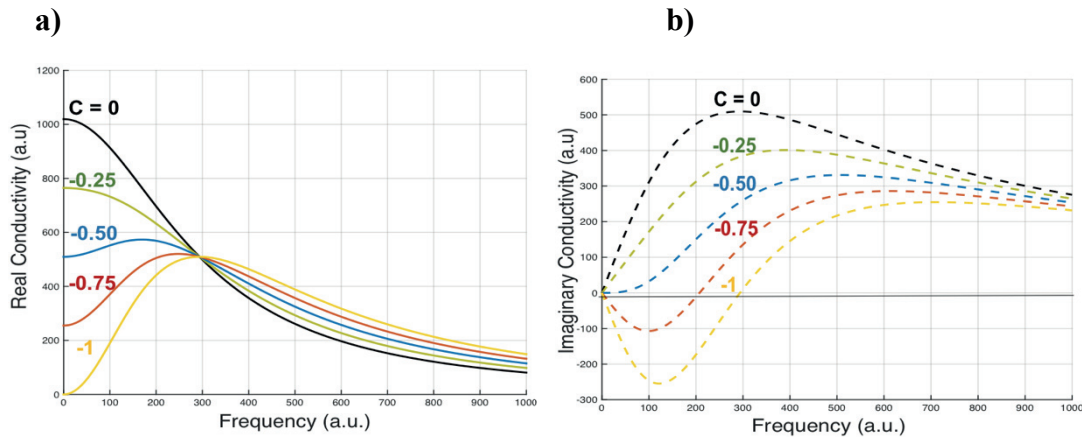
Figure 3.11 – Simulated real (a) and imaginary (b) conductivity modelled with the Drude-Smith model for varying values of the back scattering term (C)

3.3.9.2   THz conductivity spectra

In order to obtain the real and imaginary parts of the photoinduced conductivity spectrum, the dark spectrum $T(\omega)$ and the differential absorption spectrum of the photoexcited $\Delta T(\omega,t)$ are taken. The $\Delta T(\omega,t)$ measurements are taken at steady state

conditions, with t ≈ 10 ps after photoexcitation, which is longer than the formation time for the charge carriers, and at low excitation densities where there is no change in the carrier population over our measured time scale (i.e. no change in the signal amplitude as measured in the OPTP dynamics fixed at the peak of the THz amplitude). The complex photoconductivity spectrum is extracted according to equation Eq. 2.6. The real and imaginary parts of the experimentally obtained conductivity spectra for the mixed and MAPbI$_3$ perovskites are displayed in figure 3.12 (dotted plots), in addition the calculated conductivities from the Drude-Smith model are plotted on the same figure (solid lines) according to eq. 3.11. Within the parameters of the Drude-Smith model; the plasma frequency $\omega_p = \sqrt{\frac{n_\pm e^2}{\varepsilon_0 m^*}}$ has been calculated and fixed in the model using the known carrier density (1.5×10^{18} cm^{-3} for the mixed and 5×10^{17} cm^{-3} for MAPbI$_3$) (assuming 100% generation efficiency for electrons and holes)) and m* = 0.23m$_e$, which are theoretically calculated and experimentally obtained values reported in literature.[20,64] It should be noted that there could be a variation of the effective mass between perovskite compositions. In addition, our assumption of a generation efficiency of unity might be overestimated affecting ω_p. We primarily aim to correlate the observed conductivity spectra to the morphology and scattering process that occur in our two perovskite films, which can be accomplished by observing the magnitude of the Smith contribution in the Drude-Smith conductivity model. The experimental complex photoconductivity spectra for the mixed perovskite displays a nearly flat, positive real part and near zero imaginary part. For conductivity that is Drude-like we expect to see a zero imaginary component and nearly dispersionless real conductivity in our investigated THz window.

For the mixed perovskite, the conductivity spectrum could be replicated using the simple Drude model, with the Smith term set to c = 0, and a τ of 2.9 fs (calculated using Eq. 3.4 and the previously calculated mobility of 22 $cm^2.V^{-1}.s^{-1}$). Which indicates that conductivity is primarily Drude-like and not dominated by disorder induced carrier scattering or carrier localization. This can be correlated to the large crystalline domains we observe in the mixed ion perovskites from our cross sectional SEM images and the absence of charged impurities which we identified with our temperature dependent mobility measurements.

For the MAPbI$_3$ perovskite film, the imaginary part of the photoconductivity is negative at THz frequencies and becomes increasingly negative at higher frequencies. The real part of the conductivity is positive and shows a small increase with rising frequencies. For conductivity dominated by scattering the imaginary part of σ would be negative. This is reflected in the Drude-Smith fit which requires c = -0.60 and τ of 8.3 fs, in order to obtain a good fit to our experimental results. The low valued c term indicates that the Smith contribution to the conductivity dominates due to backscattering of carriers, likely off grain boundaries[65] and defects due to increased structural disorder or charged defects.[66] Our experimental results can be well explained by the small crystalline domains in our morphologically granular MAPbI$_3$ samples. Which have grains with dimensions between 5-100nm as characterized through cross-sectional SEM images of samples. And the presence scattering centres in the form of charged impurities, that were previously identified through our temperature dependent mobility measurements. Such charged

defects, in high enough densities, could act as scattering centres by providing a columbic restoring force.[67]
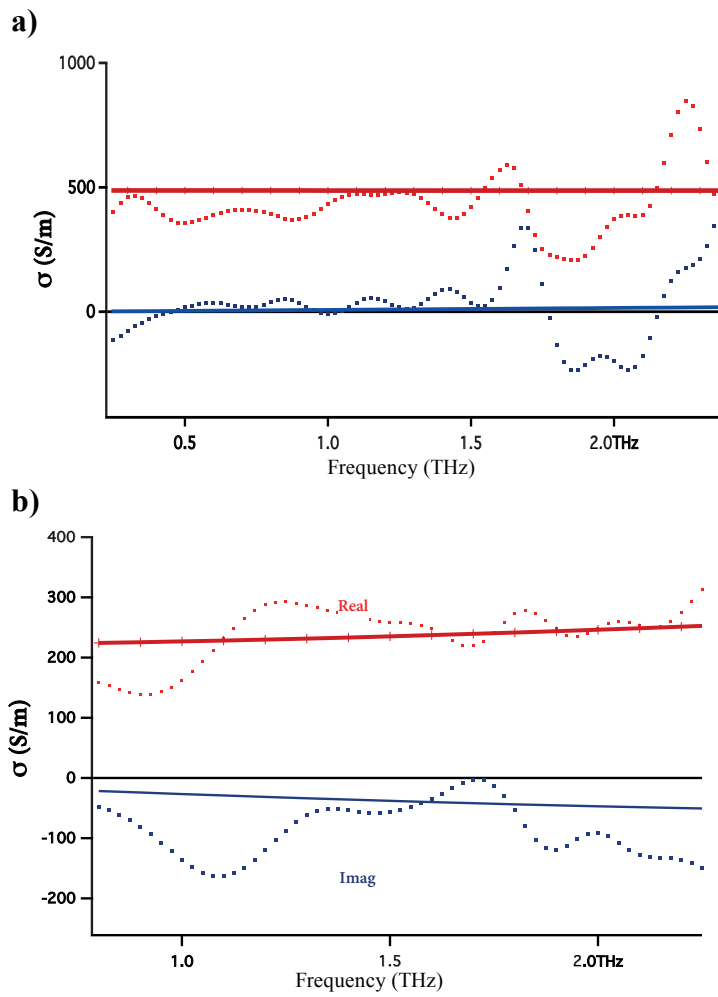
Figure 3.12 – real (red) and imaginary (blue) parts of the photoconductivity for the mixed (Fig 3.12a) and MAPbI$_3$ (3.12b) films. The dotted points represent the experimental obtained values while the solid lines are the Drude-Smith fits.
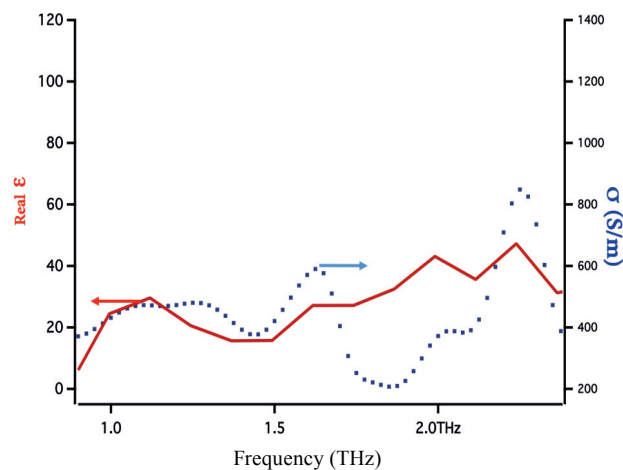
3.3.9.3   Dark permittivity spectra

We can also obtain the dark permittivity spectrum by measuring the linear scan of the THz pulse passing through the dark sample and through the reference substrate. The real part of the measured dark permittivity of the mixed ion and MAPbI$_3$ perovskites are presented in figure 3.13. In the dark permittivity spectra for MAPbI$_3$ we observe features at 1.1, 1.7 and 2.35 THz. In the mixed ion perovskite, we observe four peaks, centered at $\approx$ 1.1, 1.6, 1.9 and 2.2 THz. Previous THz measurements observed peaks at $\approx$1 Thz and 2 THz.[23] Theoretical DFT simulations and experimental measurements with Raman spectroscopy[68] of MAPbI$_3$, that lie within our measured THz window, identified two Raman active modes at 1.5 THz and 2.2 THz. With the peak at 1.5 THz being attributed to the I-Pb-I bending mode and the one at 2.2 THz corresponding to the Pb-I stretching mode.[68] The previous computational and experimental work corresponds quite closely to our observed features at 1.7 and 2.2 THz and can be assigned to the vibrational and stretching modes associated with the lead-halide bonds.
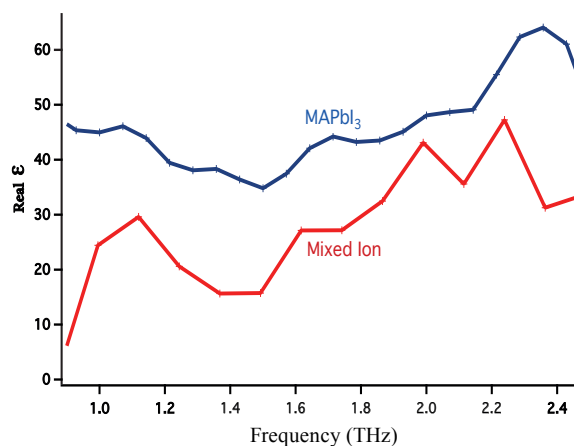
Figure 3.13 - Real dark permittivity spectra of MAPbI$_3$ (Blue) and the mixed perovskite.

In the mixed perovskite we see an additional peak at 1.9 THz and a possible shift of the two peaks centered at 2.35 and 1.7 THz in $MAPbI_3$, red shifting to 2.2 and 1.6 THz, respectively. Our observations can be related to Raman measurements of perovskites with mixtures of halides (iodide and bromide) in different ratios carried out by Ledinsky et al.[69] Their measurements showed that the observed bands are significantly stronger and sharper for the mixed halides than for single halide $MAPbI_3$ or $MAPbBr_3$.

Figure 3.14 shows the real parts of the photoconductivity and permittivity for the mixed perovskite. We observe some overlap of the features observed in the real part of the dark permittivity with the photoconductivity spectra. With sharp peaks observable at 1.6 and 2.2 THz which overlap with the peaks observed in the dark permittivity spectrum. Along with features and 1.1 and 2 THz that overlap with peaks that are observable in the dark spectrum. Since the photoconductivity spectra is obtained by dividing the $\Delta T_{sample}(\omega,t)$ of the photoexcited sample by T_{sample} of the dark sample, we would expect the peaks to cancel out. However, we continue to observe features associated with the dark spectrum

Figure 3.14 – Real dark permittivity (red) and photoconductivity (Blue) for the mixed perovskite.

in our photoconductivity spectrum. This indicates that there is an induced modulation of the vibrational modes we observe in our dark spectrum[70,71] due to photoexcitation and generation of charge carriers by the pump pulse. Future work that systematically investigates the compositional dependence of the perovskite, by sequentially varying the halide and cation ratios would shed more light on the vibrational bonds involved and the nature of their modulation subsequent to photoexcitation.

3.4 Conclusion

Over the course of this chapter we investigated two perovskite films with different chemical compositions and film morphologies. The multi-grain MAPbI$_3$ perovskite had crystal dimensions ranging from $5 - 100$ nm and fabrication of devices with these films gave average PCEs of 12%. The mixed composition produced large perovskite crystals with dimensions that were comparable to the thickness of the layer and resulted in preparation of devices with an average device PCE of 18%.

We initially carried out time resolved OPTP measurements to investigate the formation and recombination dynamics of photo-generated charge carriers. Subsequent to photoexcitation we observe that the generation of free charge carriers occurs in ≈ 600 fs and proceeds through the disassociation of a transient excitonic species. With our fluence dependent measurements we were able to identify two distinct recombination pathways following charge generation. A fast recombination pathway which is present at elevated carrier densities and proceeds through direct band-band recombination until a stable, long

lived (>1 ns) carrier population density is reached. And a slow recombination pathway that involves carriers that occupy an indirect band as well as those residing in trap states. Carriers occupying the indirect band would face a momentum forbidden recombination pathway that significantly enhances carrier lifetimes; the offset in momentum between the CB and VB would require coupling with a phonon for radiative recombination to occur or carrier recombination would have to proceed through unoccupied defect states. Both of these processes would have rates that are significantly slower than direct band-band recombination. Our results show that the density of carriers that can exist in $CB_{indirect}$ is sufficiently high ($\approx 10^{17} - 10^{18}$) to support the carrier densities which exist under the typical operational conditions in photovoltaic devices.[9]

Engineering of the film deposition process to improve the film morphology and reduce the density of trap states would enhance carrier lifetimes and facilitate the macroscale carrier transport properties. However, in order to increase the density of states that can be occupied in the indirect band, compositional engineering of the perovskite would be required to modify an intrinsic material property that is not dependent on the macroscale film morphology. Our experimental results show that in the mixed perovskite film, a significantly larger density of photogenerated charge carriers can indeed be sustained prior to the onset of the fast recombination component. This shows that tuning the chemical composition of the perovskite can modify the occupation density of the indirect band prior to recombination occurring through the direct transition.

Investigation of the conductivity spectra for the $MAPbI_3$ and mixed perovskites were also carried out and the spectra were fit using the Drude-Smith model. The conductivity

for the mixed perovskite was predominantly Drude like, whereas the MAPbI$_3$ film had a large Smith contribution to the conductivity indicating significant backscattering of carriers. The smaller crystal size in our MAPbI$_3$ film results in a larger number of boundaries and surface states between the grains which would contribute to scattering. In addition, the charged impurity scattering that was identified through our temperature dependent photoconductivity measurements can also be linked to the backscattering we observe in the Drude-Smith fits. We observed vibrational modes in the dark permittivity spectrum for both of our investigated samples as well as the photo-induced modulation of these modes in the mixed sample. These observations provide direction for future work which investigates the dependence of the cation and halides, on the intensity and frequencies of the observed spectral features.

Such compositional investigations can also provide insights into the nature of the photoinduced modulations in the spectra. These measurements can be combined with newly developed time-resolved broadband-THz spectroscopy which allows for the direct probing of carrier dynamics at faster timescales ($\approx$ 50 fs) and investigation of the THz spectrum between 2 - 20 THz, which was outside our currently accessible frequency and time domain. This relatively broader band THz probe can be used to probe phonon modes that were previously not visible and identify their possible coupling with charge carriers.

Due to the high frequency of the probe and short pulse duration, the THz technique measures carrier mobility on a short length scale and would likely be the upper bounds for the sample. The calculated carrier mobilities were 41 ± 3 cm^2 V^{-1} s^{-1} for MAPbI$_3$ and 22 ± 4 cm^2 V^{-1} s^{-1} for the mixed perovskite sample. Our results show that the device

performance cannot be directly linked to the intrinsic carrier mobility, with the $MAPbI_3$ device having a PCE of 12% while the mixed perovskite had a PCE of 18%. Rather, the overall device performance is determined by range of other factors that determine the efficiency with which the photogenerated charge carriers can be extracted at the electrodes. The mixed perovskite was shown to be able to sustain carrier densities that were an order of magnitude higher than the conventional $MAPbI_3$ composition prior to the onset of fast bimolecular recombination, while also demonstrating a lower rate of bimolecular recombination. Both of these attributes would support the efficient extraction of charge carriers prior to their loss through recombination.

In addition, the microscale mobility we investigate with the THz setup would not necessarily represent the average mobility of carriers travelling across the film to their respective accepting layers. The macroscale mobility is correlated with the film morphology and process that hinder the transport of carriers across the film, such as trapping/de-trapping at grain boundaries and defects. This would result in an average mobility that is lower than the intrinsic mobility of carriers in a perfect defect free crystal. Characterization of the macroscale transport properties and correlating the evolution of the carrier's mobility with film morphology as they drift across the device are important steps in identifying the mechanisms that limit transport across the film and will be investigated in detail over the next chapters.
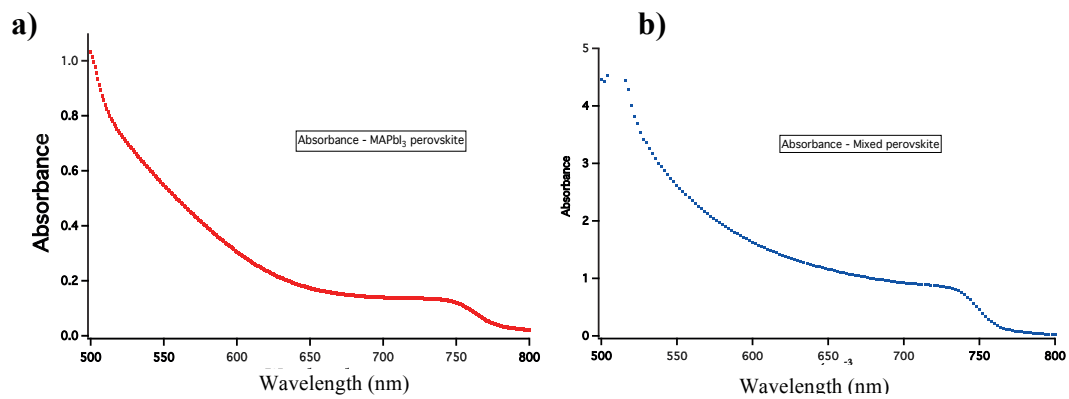
3.5 Appendix

Appendix 3.1 - Negligible phase change on photoexcitation
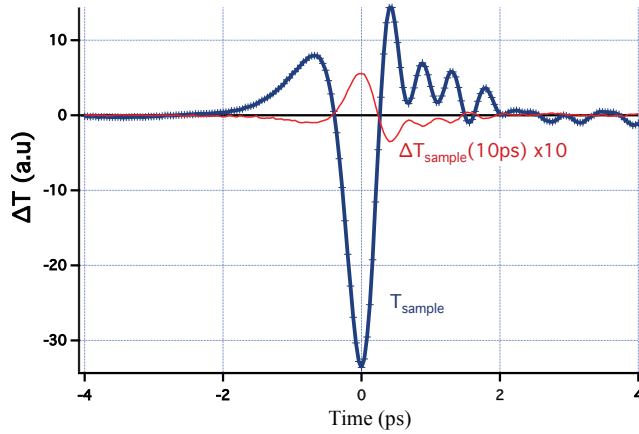
Figure A3.1 - Typical THz waveform passing for the pulse transmitted through the unexcited sample (blue) and the pulse transmitted through the photoexcited sample. (red)

Appendix 3.2

Figure A3.2 – Absorbance spectrum of MAPbI$_3$ and the mixed perovskite.

3.6 Bibliography

1.   Kim, H.-S. *et al.* Lead iodide perovskite sensitized all-solid-state submicron thin film mesoscopic solar cell with efficiency exceeding 9%. *Sci Rep* **2,** 591 (2012).

2.   Lee, M. M., Teuscher, J., Miyasaka, T., Murakami, T. N. & Snaith, H. J. Efficient Hybrid Solar Cells Based on Meso-Superstructured Organometal Halide Perovskites. *Science* **338,** 643–647 (2012).

3.   Stranks, S. D. *et al.* Electron-hole diffusion lengths exceeding 1 micrometer in an organometal trihalide perovskite absorber. *Science* **342,** 341–344 (2013).

4.   Xing, G. *et al.* Long-Range Balanced Electron-and Hole-Transport Lengths in Organic-Inorganic $CH_3NH_3PbI_3$. *Science* **432,** 344–347 (2013).

5.   Song, Z., Watthage, S. C., Phillips, A. B. & Heben, M. J. Pathways toward high-performance perovskite solar cells: review of recent advances in organo-metal halide perovskites for photovoltaic applications. *J. Photon. Energy* **6,** 022001–022001 (2016).

6.   Pellet, N. *et al.* Mixed-Organic-Cation Perovskite Photovoltaics for Enhanced Solar-Light Harvesting. *Angewandte Chemie International Edition* **53,** 3151–3157 (2014).

7.   Saliba, M. *et al.* Cesium-containing Triple Cation Perovskite Solar Cells: Improved Stability, Reproducibility and High Efficiency. *Energy & Environmental Science* (2016). doi:10.1039/C5EE03874J

8.   Motta, C. *et al.* Revealing the role of organic cations in hybrid halide perovskite $CH_3NH_3PbI_3$. *Nat Comms* **6,** 7026 (2015).

9.   Azarhoosh, P., Frost, J. M., McKechnie, S., Walsh, A. & van Schilfgaarde, M. Relativistic origin of slow electron-hole recombination in hybrid halide perovskite solar cells. *APL Materials* **4,** 091501 (2016).

10.   Etienne, T., Mosconi, E. & De Angelis, F. Dynamical Origin of the Rashba Effect in Organohalide Lead Perovskites: A Key to Suppressed Carrier Recombination in Perovskite Solar Cells? *J. Phys. Chem. Lett.* **7,** 1638–1645 (2016).

11.   Hutter, E. M. *et al.* Direct-indirect character of the bandgap in methylammonium

lead iodide perovskite. *Nat Mater* 115–120 (2016). doi:10.1038/nmat4765

12. Niesner, D. *et al.* Giant Rashba Splitting in CH3NH3PbBr3 Organic-Inorganic Perovskite. *Phys. Rev. Lett.* **117,** 126401 (2016).

13. Zheng, F., Tan, L. Z., Liu, S. & Rappe, A. M. Rashba Spin–Orbit Coupling Enhanced Carrier Lifetime in CH3NH3PbI3. *Nano Lett.* **15,** 7794–7800 (2015).

14. Im, J.-H., Lee, C.-R., Lee, J.-W., Park, S.-W. & Park, N.-G. 6.5% efficient perovskite quantum-dot-sensitized solar cell. *Nanoscale* **3,** 4088–4093 (2011).

15. Paraecattil, A. A., De Jonghe-Risse, J., pranculis, V., Teuscher, J. & Moser, J. E. Dynamics of Photocarrier Separation in MAPbI3 Perovskite Multigrain Films under a Quasistatic Electric Field. *J. Phys. Chem. C* **120,** 19595–19602 (2016).

16. Teuscher, J., Ulianov, A., Müntener, O., Grätzel, M. & Tétreault, N. Control and Study of the Stoichiometry in Evaporated Perovskite Solar Cells. *ChemSusChem* **8,** 3847–3852 (2015).

17. Baena, J. P. C. *et al.* Highly efficient planar perovskite solar cells through band alignment engineering. *Energy & Environmental Science* **8,** 2928–2934 (2015).

18. D'Innocenzo, V. *et al.* Excitons versus free charges in organo-lead tri-halide perovskites. *Nat Comms* **5,** 3586 (2014).

19. Miyata, A. *et al.* Direct measurement of the exciton binding energy and effective masses for charge carriers in organic-inorganic tri-halide perovskites. *Nat Phys* **11,** 582–U94 (2015).

20. Galkowski, K. *et al.* Determination of the exciton binding energy and effective masses for methylammonium and formamidinium lead tri-halide perovskite semiconductors. *Energy & Environmental Science* **9,** 962–970 (2016).

21. Hirasawa, M., Ishihara, T., GOTO, T., Uchida, K. & Miura, N. Magnetoabsorption of the Lowest Exciton in Perovskite-Type Compound (CH3H3)PbI3. *Physica B* **201,** 427–430 (1994).

22. Mahboubi Soufiani, A. *et al.* Polaronic exciton binding energy in iodide and bromide organic-inorganic lead halide perovskites. *Appl. Phys. Lett.* **107,** 1–5 (2015).

23. Wehrenfennig, C., Liu, M., Snaith, H. J., Johnston, M. B. & Herz, L. M. Charge-

carrier dynamics in vapour-deposited films of the organolead halide perovskite CH3NH3PbI3−xClx. *Energy & Environmental Science* **7,** 2269–2275 (2014).

24. Marchioro, A. *et al.* Unravelling the mechanism of photoinduced charge transfer processes in lead iodide perovskite solar cells. *Nature Photonics* **8,** 250–255 (2014).

25. Wehrenfennig, C., Eperon, G. E., Johnston, M. B., Snaith, H. J. & Herz, L. M. High charge carrier mobilities and lifetimes in organolead trihalide perovskites. *Adv. Mater. Weinheim* **26,** 1584–1589 (2014).

26. Chen, Y. *et al.* Extended carrier lifetimes and diffusion in hybrid perovskites revealed by Hall effect and photoconductivity measurements. *Nat Comms* **7,** 12253 (2016).

27. Yang, Y. *et al.* Large polarization-dependent exciton optical Stark effect in lead iodide perovskites. *Nat Comms* **7,** 12613 (2016).

28. Wu, X. *et al.* Trap States in lead iodide perovskites. *J. Am. Chem. Soc.* **137,** 2089–2096 (2015).

29. Ponseca, C. S. *et al.* Organometal halide perovskite solar cell materials rationalized: ultrafast charge generation, high and microsecond-long balanced mobilities, and slow recombination. *J. Am. Chem. Soc.* **136,** 5189–5192 (2014).

30. Stranks, S. D. *et al.* Recombination Kinetics in Organic-Inorganic Perovskites: Excitons, Free Charge, and Subgap States. *Physical Review Applied* **2,** (2014).

31. Leppert, L., Reyes-Lillo, S. E. & Neaton, J. B. Electric Field- and Strain-Induced Rashba Effect in Hybrid Halide Perovskites. *J. Phys. Chem. Lett.* **7,** 3683–3689 (2016).

32. Azarhoosh, P., Frost, J. M., McKechnie, S., Walsh, A. & van Schilfgaarde, M. Relativistic origin of slow electron-hole recombination in hybrid halide perovskite solar cells. *APL Materials* **4,** 091501 (2016).

33. Zheng, F., Tan, L. Z., Liu, S. & Rappe, A. M. Rashba Spin-Orbit Coupling Enhanced Carrier Lifetime in CH3NH3PbI3. *Nano Lett.* **15,** 7794–7800 (2015).

34. Ke, X., Yan, J., Zhang, A., Zhang, B. & Chen, Y. Optical band gap transition from direct to indirect induced by organic content of CH3NH3PbI3 perovskite films.

Appl. Phys. Lett. **107,** 091904 (2015).

35. Even, J., Pedesseau, L., Jancu, J.-M. & Katan, C. Importance of Spin-Orbit Coupling in Hybrid Organic/Inorganic Perovskites for Photovoltaic Applications. *J. Phys. Chem. Lett.* **4,** 2999–3005 (2013).

36. Wang, Y. *et al.* Trap-limited charge recombination in intrinsic perovskite film and meso-superstructured perovskite solar cells and the passivation effect of the hole-transport material on trap states. *Phys Chem Chem Phys* **17,** 29501–29506 (2015).

37. Wen, X. *et al.* Defect trapping states and charge carrier recombination in organic-inorganic halide perovskites. *Journal of Materials Chemistry C* **4,** 793–800 (2016).

38. Trap States in Lead Iodide Perovskites. **137,** 2089–2096 (2015).

39. deQuilettes, D. W. *et al.* Impact of microstructure on local carrier lifetime in perovskite solar cells. *Science* **348,** 683–686 (2015).

40. Jeon, N. J. *et al.* Solvent engineering for high-performance inorganic-organic hybrid perovskite solar cells. *Nat Mater* **13,** 897–903 (2014).

41. Lim, S. S. *et al.* Modulating carrier dynamics through perovskite film engineering. *Phys Chem Chem Phys* **18,** 27119–27123 (2016).

42. Bag, S. & Durstock, M. F. Large Perovskite Grain Growth in Low-Temperature Solution-Processed Planar p-i-n Solar Cells by Sodium Addition. *ACS Appl Mater Interfaces* **8,** 5053–5057 (2016).

43. Kim, M. K. *et al.* Effective control of crystal grain size in $CH_3NH_3PbI_3$ perovskite solar cells with a pseudohalide $Pb(SCN)_2$ additive. *CrystEngComm* **18,** 6090–6095 (2016).

44. Xu, J. *et al.* Perovskite-fullerene hybrid materials suppress hysteresis in planar diodes. *Nat Comms* **6,** 7081 (2015).

45. Johnston, M. B. & Herz, L. M. Hybrid Perovskites for Photovoltaics: Charge-Carrier Recombination, Diffusion, and Radiative Efficiencies. *Acc. Chem. Res.* **49,** 146–154 (2016).

46. Trinh, M. T., Wu, X., Niesner, D. & Zhu, X.-Y. Many-body interactions in photo-excited lead iodide perovskite. *Journal of Materials Chemistry A* **3,** 9285–9290 (2015).

47. Charache, G. W. *et al.* InGaAsSb thermophotovoltaic diode: Physics evaluation. *Journal of Applied Physics* **85,** 2247–2252 (1999).

48. Chen, Y. *et al.* Extended carrier lifetimes and diffusion in hybrid perovskites revealed by Hall effect and photoconductivity measurements. *Nat Comms* **7,** 12253 (2016).

49. Savenije, T. J. *et al.* Thermally Activated Exciton Dissociation and Recombination Control the Carrier Dynamics in Organometal Halide Perovskite. *J. Phys. Chem. Lett.* **5,** 2189–2194 (2014).

50. Paracchino, A., Brauer, J. C., Moser, J.-E., Thimsen, E. & Graetzel, M. Synthesis and Characterization of High-Photoactivity Electrodeposited Cu2O Solar Absorber by Photoelectrochemistry and Ultrafast Spectroscopy. *J. Phys. Chem. C* **116,** 7341–7350 (2012).

51. Weller, M. T., Weber, O. J., Henry, P. F., Di Pumpo, A. M. & Hansen, T. C. Complete structure and cation orientation in the perovskite photovoltaic methylammonium lead iodide between 100 and 352 K. *Chem. Commun. (Camb.)* **51,** 4180–4183 (2015).

52. Zhao, T., Shi, W., Xi, J., Wang, D. & Shuai, Z. Intrinsic and Extrinsic Charge Transport in CH3NH3PbI3 Perovskites Predicted from First-Principles. *Sci Rep* **7,** 19968 (2016).

53. Van Zeghbroeck, B. Principles of semiconductor devices. *Colarado University* (2004).

54. Azpiroz, J. M., Mosconi, E., Bisquert, J. & De Angelis, F. Defect migration in methylammonium lead iodide and its role in perovskite solar cell operation. *Energy & Environmental Science* **8,** 2118–2127 (2015).

55. Yuan, Y. & Huang, J. Ion Migration in Organometal Trihalide Perovskite and Its Impact on Photovoltaic Efficiency and Stability. *Acc. Chem. Res.* **49,** 286–293 (2016).

56. Shao, Y. *et al.* Grain boundary dominated ion migration in polycrystalline organic–inorganic halide perovskite films. *Energy & Environmental Science* **9,** 1752–1759 (2016).

57.   Lakhwani, G., Rao, A. & Friend, R. H. Bimolecular Recombination in Organic Photovoltaics. *http://dx.doi.org/10.1146/annurev-physchem-040513-103615* **65,** 557–581 (2014).

58.   Beard, M. C., Turner, G. M. & Schmuttenmaer, C. A. Transient photoconductivity in GaAs as measured by time-resolved terahertz spectroscopy. *Phys. Rev. B* **62,** 15764–15777 (2000).

59.   Kaindl, R. A., Carnahan, M. A., Hägele, D., Lövenich, R. & Chemla, D. S. Ultrafast terahertz probes of transient conducting and insulating phases in an electron-hole gas. *Nature* **423,** 734–738 (2003).

60.   Wooten, F. *Optical properties of solids*. (2013).

61.   Ulbricht, R., Hendry, E., Shan, J., Heinz, T. F. & Bonn, M. Carrier dynamics in semiconductors studied with time-resolved terahertz spectroscopy. *Rev. Mod. Phys.* **83,** 543–586 (2011).

62.   La-o-vorakiat, C. *et al.* Elucidating the role of disorder and free-carrier recombination kinetics in $CH_3NH_3PbI_3$ perovskite films. *Nat Comms* **6,** 7903 (2015).

63.   Cooke, D. G. *et al.* Transient terahertz conductivity in photoexcited silicon nanocrystal films. *Phys. Rev. B* **73,** 193311 (2006).

64.   Filip, M. R., Verdi, C. & Giustino, F. GW Band Structures and Carrier Effective Masses of $CH_3NH_3PbI_3$ and Hypothetical Perovskites of the Type $APbI_3$: A = NH_4, PH_4, AsH_4, and SbH_4. *J. Phys. Chem. C* **119,** 25209–25219 (2015).

65.   Němec, H., Kužel, P. & Sundström, V. Far-infrared response of free charge carriers localized in semiconductor nanoparticles. *Phys. Rev. B* **79,** 115309 (2009).

66.   Ahn, H. *et al.* Terahertz spectroscopic study of vertically aligned InN nanorods. *Appl. Phys. Lett.* **91,** 163105 (2007).

67.   Ahn, H. *et al.* Terahertz spectroscopic study of vertically aligned InN nanorods. *Appl. Phys. Lett.* **91,** 163105 (2007).

68.   Quarti, C. *et al.* The Raman Spectrum of the $CH_3NH_3PbI_3$ Hybrid Perovskite: Interplay of Theory and Experiment. *J. Phys. Chem. Lett.* 131226091716006 (2013). doi:10.1021/jz402589q

69.   Ledinský, M. *et al.* Raman Spectroscopy of Organic-Inorganic Halide Perovskites. *J. Phys. Chem. Lett.* **6,** 401–406 (2015).

70.   Hoke, E. T. *et al.* Reversible photo-induced trap formation in mixed-halide hybrid perovskites for photovoltaics. *Chemical Science* **6,** 613–617 (2015).

71.   Zhu, X.-Y. & Podzorov, V. Charge Carriers in Hybrid Organic–Inorganic Lead Halide Perovskites Might Be Protected as Large Polarons. *J. Phys. Chem. Lett.* **6,** 4758–4761 (2015).

4. Time-Resolved Electroabsorption Spectroscopy of MAPbI$_3$ Films

This chapter is based on the publication:

Dynamics of Photocarrier Separation in MAPbI$_3$ Perovskite Multigrain Films under a Quasistatic Electric Field. Arun Aby Paraecattil, J. De Jonghe-Risse, V. Pranculis, J. Teuscher and J.-E. Moser. Journal of Physical Chemistry C, vol. 120, num. 35, p. 19595-19602, 2016.

Abstract: Applying time-resolved electroabsorption spectroscopy for the first time to methylammonium lead triiodide perovskite (MAPbI$_3$) thin films under reverse bias, we monitored optically the ultrafast evolution of the local counter-electric field produced by the drift of photogenerated electrons and holes in opposite directions. Under an externally applied electric field of $|E| < 10^5$ V cm^{-1}, the carriers were found to reach a separation of 40 nm within ~1 ps. This distance corresponds to the average dimensions of crystalline grains in the active film, at the boundaries of which charges were trapped. An intragrain average carrier drift mobility of $\mu_\pm = 23$ cm^2 V^{-1} s^{-1} was inferred. Subsequent charge detrapping, migration through the entire film, and accumulation at its insulated surfaces caused a blue shift of the perovskite absorption edge that arose within tens of picoseconds, owing to a trap-limited electron drift mobility $\mu_n = 6$ cm^2 V^{-1} s^{-1}. Charge recombination was entirely suppressed between field-separated photocarriers generated at initial densities of $n_0 \leq 2 \times 10^{16}$ cm^{-3}. Accumulation of electrons at the interface between a mesoporous TiO$_2$ electron-transport layer and a multigrain MAPbI$_3$ film was also observed, which was indicative of delayed charge injection through a poor contact junction.

4.1 Introduction

In this chapter we continue our investigation of previously introduced perovskite based films using time resolved electro-absorption spectroscopy (TREAS). Despite the significant research efforts that have been focused towards the characterization of the fundamental properties of these materials we still have a lot to understand about the basic mechanisms of operation. Typical photovoltaic device characterization protocols rely on current-voltage scans to measure power conversion efficiency. For a number of photovoltaic cell architectures, however, accurate device characterization has proven to be difficult, due to the apparent huge dielectric constant of the perovskite at low frequency and an anomalous photocurrent hysteresis observed under typical measurement conditions.[1-3] The latter effects reflect a polarization of the active material submitted to an electric field and is believed to be primarily caused by slow halide ions and halide vacancies migration within the material and charge accumulation at ion-blocking interfaces.[4-6]

Ionic disorder in perovskites at room temperature imply the presence of interstitial iodide anions and iodide vacancies within the crystal that are likely to act as hole- and electron traps, respectively.[7-9] Photophysical studies,[10,11] photoluminescence nano-imaging,[12] and transient absorption microscopy [13-15] have also evidenced trap and midgap states in the material, which are located predominantly at grain boundaries and interfaces. The size of crystalline grains in perovskite films and the quality of the electronic contact at the interface between the active layer and the electron acceptor material appear, therefore, to play a crucial role in determining the devices photovoltaic performances.[16-

[18] The design of new possibilities to improve them call for a deeper insight into the details of the trapping of photogenerated charge carriers at grain boundaries and of the accumulation of charges at the perovskite interfaces. The determination of carrier mobilities has been achieved so far by the application of various techniques, contactless time-domain terahertz spectroscopy being one among them. This technique, however, probes the oscillation of carriers over very short distances and does not allow for the characterization of drift mobilities on the order of 200−400 nm, corresponding to typical thicknesses of perovskite films in a solar cell. Apart from Hall effect measurements, a number of electrical methods, such as time-of-flight (TOF) techniques, have been employed to determine dc mobilities within large crystals and in complete photovoltaic devices.[19,20] The nanosecond time resolution of photocurrent probing constitutes a serious limitation in these cases and prevents the observation of ultrafast stages of the carrier separation dynamics.

Time-resolved electroabsorption spectroscopy (TREAS) has been designed to probe optically the perturbation of an externally applied electric field experienced by an absorber semiconductor, a donor−acceptor bilayer, or a solid blend with femtosecond time resolution.[21] This recently established experimental technique relies on the electric-field-dependent optical response of a material (electroabsorption: Stark or Franz−Keldysh effects). Photogeneration of charge pairs, splitting of these pairs, and subsequent drift of the carriers perturb the electric field exerted locally on the material, causing changes in its absorption. Monitoring the temporal evolution of these optical properties in an ultrafast pump−probe spectroscopy scheme allows for the reconstruction of the electric field and,

hence, the dynamics of charge motion. TREAS based on the transient Stark effect has been successfully applied to scrutinize the charge generation and separation dynamics in bilayer and bulk heterojunction organic photovoltaic cells.[22,23] This technique was applied in this work for the first time to investigate the dynamics of charge carrier separation and trapping in MAPbI$_3$ perovskite thin films subjected to an external quasi-static electric field.

4.2   Experimental

4.2.1 Sample preparation

Vapor deposition of the perovskite films were carried out by Dr. Joël Teuscher. ALD deposition of the Al$_2$O$_3$ layer was carried out by Dr. Aswani Yella. The general device fabrication procedure is as follows:

An ITO conductive glass substrate was covered by atomic layer deposition (ALD) with a 30-nmthick film of insulating alumina. Al$_2$O$_3$ was deposited from pulses of Al(CH$_3$)$_3$ precursor and water vapor at 114°C.[24] A 280-nm-thick film of MAPbI$_3$ was then coated on top of the alumina layer by thermally coevaporating methylammonium iodide (CH$_3$NH$_3$I) and lead iodide (PbI$_2$) in a vacuum. Methylammonium iodide was synthesized and purified following a reported recipe.[25] PbI$_2$ (99%, Aldrich) was used as received. Substrates and chemicals were loaded in an evaporator chamber (custom-built, Lesker). The chamber was pumped down to a base pressure of 9×10^{-6} mbar. The methylammonium iodide source was contained in a molybdenum boat covered by a

perforated lid (Omnicore). The CH_3NH_3I evaporation rate was adjusted with a proportional−integral−derivative (PID) controller conditioning the heating power supply with a pressure set point of 1.23×10^{-4} mbar. PbI_2 was placed in a quartz crucible heated by a tungsten wire coil (EVB9, EVC2, Lesker), and its evaporation rate was controlled with a quartz microbalance placed inside the chamber. The rate of $MAPbI_3$ deposition onto the substrate was 0.03 nm s^{-1}. Details on the evaporation setup and procedure are provided in ref [26]. An insulating poly(methyl methacrylate) (PMMA) layer (25−30 nm thick) was deposited by spin-coating on top of the evaporated perovskite. PMMA beads (MW 120000, Sigma-Aldrich) were dissolved in chlorobenzene (15 mg/mL), and the solution was spin-coated (5000 rpm for 2 min) in a glovebox under a dry and oxygen free atmosphere. Gold was finally thermally evaporated on the polymer (BenchTop Turbo evaporator, Denton), yielding an 80-nm-thick film of metal. Samples were kept in the glovebox until they were used for laser experiments. The aforementioned vacuum deposition techniques were employed to prepare complete solar cell devices with an ITO conductive glass|mesoporous-TiO_2|vapor-deposited $MAPbI_3$|Au architecture. Deposition of the 2-μm-thick mesoporous titania layer was carried out by spin-coating a colloidal solution of TiO_2 with a particle diameter of 20 nm at 5000 rpm for 20s. The film was then gradually heated to 500 °C and sintered at that temperature for 15 min.

## 4.2.2 Device characterization

A ZEISS Merlin HR-SEM (Scanning electron microscope) was used to characterize the morphology of the device cross-section. The measurements were carried out by Dr. Ibrahim Dar.

4.2.3   Time resolved electro-absorption spectroscopy (TREAS) and Transient absorption (TA) spectroscopy

The experimental details have been previously described in section 2.2. Similar pump−probe schemes were used for ultrafast transient absorption spectroscopy and TREAS measurements. Both experiments were based on a common amplified Ti:sapphire femtosecond laser system (CPA-2001, Clark-MXR), with an output wavelength of 780 nm at a repetition rate of 1 kHz. The pump beam at 545 nm was generated by a two-stage noncollinear optical parametric amplifier (NOPA-Plus, ClarkMXR), with a typical pulse duration of 50−60 fs. The pump and probe pulses were time-delayed with respect to one another using a computerized translation stage, and they were crossed in the sample. After being being reflected off the gold electrode of the EDA sample (after entering through the transparent ITO layer), the probe beam was dispersed in a grating spectrograph and detected shot by shot at a 1 kHz rate with CCD detector (S07030- 0906, Hamamatsu). For TA spectroscopy, the pump beam was chopped at one-half the amplifier repetition rate (500 Hz). In TREAS experiments, each probe pulse was crossed with the pump at the full 1 kHz repetition rate. The voltage applied to the electrodes was modulated at 500 Hz using a function generator (AFG 2021, Tektronix), which provided square voltage pulses (up to 6-V reverse bias, 100-μs pulse duration). Multiple samples were measured under the same conditions, yielding consistent results.

4.3 Results

4.3.1 Device characterization
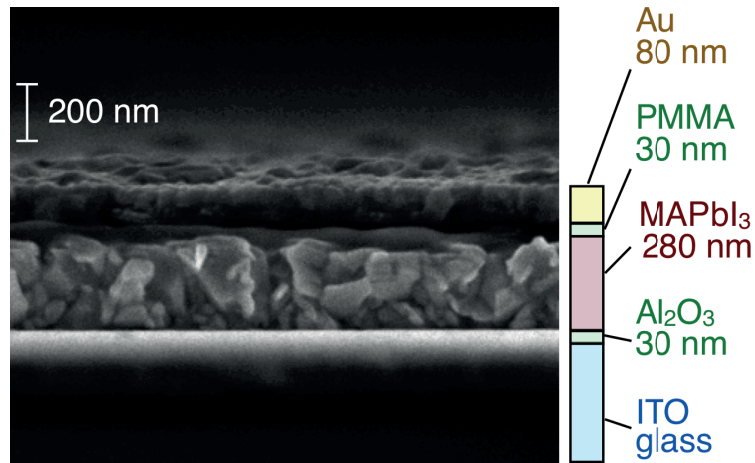
Figure 4.1 -. Cross-sectional scanning electron microscopy (SEM) image of an insulated, vapor-deposited MAPbI$_3$ film sandwiched between two conductive electrodes. From bottom to top, the micrograph shows ITO conductive glass coated with an insulating layer of alumina, the perovskite film, a second insulating layer made of spin-coated PMMA, and an evaporated gold layer constituting the second electrode. The polycrystalline morphology of the vapor-deposited MAPbI$_3$ film is clearly visible, with grain size varying between 5 and 100 nm.

The samples used in this work had a multilayer structure of the form ITO|Al$_2$O$_3$|MAPbI$_3$|PMMA|Au, where the active material was sandwiched between two insulating layers acting as barriers against carrier injection and collection at the electrodes. Samples were prepared by coating an ITO/glass conductive transparent substrate with an insulating, 30-nm-thick Al$_2$O$_3$ layer, on top of which a 280-nm-thick film of MAPbI$_3$ was deposited by coevaporation of methylammonium iodide (CH$_3$NH$_3$I) and lead iodide (PbI$_2$).[26,27] A 30nm insulating layer of PMMA was deposited by

spincoating a solution of the polymer onto the perovskite, allowing the active film to be encapsulated and protected against possible degradation by moisture and oxygen. The overall thickness of the sample between the two conductive electrodes was determined by scanning electron microscopy to be 340 ± 20 nm (Figure 4.1).

4.3.2 Spectral changes due to optical and electrical perturbations

A short recap of the ΔA signals we observe using the TREAS and TA technique will be given to aid in the understanding of the presented measurements. To obtain the transient absorption (TA) spectra, the pump excitation pulse is modulated by using a chopper to physically block every second pump pulse. The differential absorption signal (ΔA) is effectively the difference between the white light spectrum with and without the pump pulse (Eq. 4.1). The TA dynamics are obtained by monitoring the ΔA at different relative time delays (t) between the pump and probe pulses. To generate the static electro-absorption (EA) spectra, a square voltage pulse is applied between the ITO and Au electrodes with a pulse duration of 100 µs and a repetition rate of 500 Hz (half the repetition rate of the laser). In this case, the function generator (which applies the voltage) acts as the chopper. We modulate the applied voltage and look at the white light spectrum with and without the externally applied voltage and the ΔA is obtained according to Eq. 4.2. The electro-modulated absorption spectra (EDA) spectra and dynamics are obtained by modulating the applied voltage while obtaining the ΔA at different relative pump and probe delays (Eq. 4.3).

The absorbance changes, ΔA, determined in each case are defined by the following differences:

TA spectrum

$$\Delta A(t, \lambda) = A_{pump}(t, \lambda) - A(t, \lambda) \qquad \textbf{Eq. 4.1}$$

EA spectrum

$$\Delta A(\lambda) = A_{E}(\lambda) - A(\lambda) \qquad \textbf{Eq. 4.2}$$

EDA spectrum

$$\Delta A(t, \lambda) = A_{E+Pump}(t, \lambda) - A_{pump}(t, \lambda) \qquad \textbf{Eq. 4.3}$$

where $A(\lambda)$ is the absorbance spectrum measured in the absence of a field and with no pump excitation, $A_{E}(\lambda)$ is the spectrum of the sample subjected to the electric field E, $A_{pump}(t, \lambda)$ is the transient spectrum obtained upon laser-pulsed excitation, and $A_{E+pump}(t, \lambda)$ is the transient spectrum of the sample subjected to both the external electric field and the optical pump. Figure 4.2 shows the static electro-absorption spectrum (red trace) of MAPbI$_3$, its transient absorption spectrum (yellow trace), and its electro-modulated differential absorption spectrum (black trace).
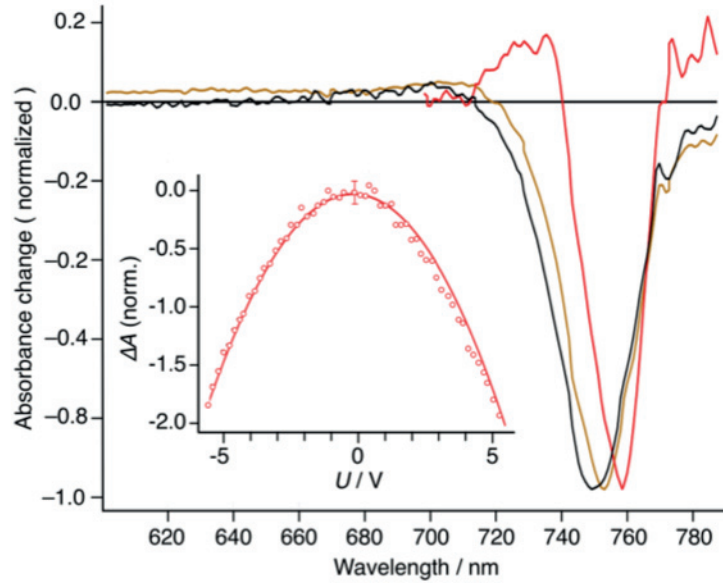
Figure 4.2 - Differential absorption spectra of insulated MAPbI$_3$ films. **Yellow line**: Transient absorbance (TA) spectrum (U = 0, λ_{pump} = 545 nm, probed 300ps after pump excitation). **Red line**: Electroabsorption (EA) spectrum (U = 6.0 V, no pump pulse). **Black line**: Electromodulated differential absorbance (EDA) spectrum (U = 6.0 V, λ_{pump} = 545 nm, probed 300 ps after pump excitation). **Inset**: Dependence of the differential electro-absorption (EA) signal measured at λ_{probe} = 762 nm upon the applied voltage (forward and reverse bias). The red curve drawn through the experimental points is the best fit to a parabolic function.

The change in the absorption band shape, $\Delta A(\nu)$, of molecular and excitonic species subjected to an electric field E can be described as the sum of first and second derivatives of the absorption spectrum $A(\nu)$:[28,29]

$$\Delta A(\lambda) = -\frac{\partial A(\lambda)}{\partial \lambda} \bullet \vec{m}_{0k} \vec{E} - \frac{1}{2} \frac{\partial A(\lambda)}{\partial \lambda} \bullet \vec{p}_{0k} \vec{E}^2 + \frac{1}{2} \frac{\partial^2 A(\lambda)}{\partial \lambda^2} \bullet (\vec{m}_{0k} \vec{E})^2 \quad \textbf{Eq. 4.4}$$

where E is the electric field exerted on the sample, m_{0k} is the change in the permanent dipole moment, and p_{0k} is the difference in polarizability between the ground (0) and transition state (k) connected by the optical transition that is being probed.

The linear and quadratic terms in Eq. 4.4 can be distinguished by measuring the electroabsorption as a function of the applied bias voltage. The inset of Figure 4.2 shows the field dependence of the change in electroabsorption amplitude at the wavelength λ_{probe} = 762 nm. A parabolic dependence of the EA signal on the applied voltage is observed. In our case, EA measured at the absorption edge seems to be primarily due to a shift and broadening of the Gaussian excitonic band component of the perovskite absorbance spectrum (Appendix 4.1 - Figure A4.1, A4.2)[30], which is expected to produce a quadratic Stark effect if the polarizability of the material is reasonably isotropic.[28,29] Electroabsorption spectra of insulated MAPbI$_3$ films were recently shown to also be compatible with low-field Franz−Keldysh−Aspnes (FKA) model, according to which relative transmittance or reflectance changes also scale quadratically with the electric field.[31]

The symmetrical responses of the EA signals (Inset, Fig. 4.2) observed at both forward and reverse applied biases confirm that the insulating layers effectively prevent carrier injection at the electrodes. Any interfacial charge transfer occurring at a particular junction would produce a decrease of the effective electric field exerted on the material and dramatically reduce the observed electroabsorption upon reaching a critical voltage value under normal bias.

The EA spectrum in Figure 4.2 shows a negative absorbance change at λ_{probe} = 745−775 nm, with a maximum at 762 nm along with a weaker positive ΔA feature at λ_{probe} = 718−745 nm, an additional positive band above 775 nm is also visible. The shape of the EA spectrum is indicative of a blue shift of the excitonic band of $MAPbI_3$ upon application of the external electric field and is typical of quadratic Stark or FKA effects, where the differential absorbance appears as a mixture of the first and second derivatives of the absorption spectrum. The TA spectrum recorded at a delay time of 300 ps after the pump excitation shows a negative band between 720 and 780 nm with a peak at 757 nm. This feature is associated with the ground-state bleaching of the perovskite, whereas the broad positive absorption band spanning 550−720 nm is due to charge carriers generated in the photoexcited material.[32-34] A shift of 6 nm is observed between the negative peaks of the EA and TA spectra with full width at half-maximum (FWHM) values of 20 and 30 nm, respectively. The EDA spectrum recorded 300 ps after pump excitation is also shown in Figure 4.2. The negative band at 751 nm is slightly blue-shifted relative to the ground-state bleaching observed in the TA spectrum. Whereas a positive band at 680−720 nm is observed, the transient absorption feature due to photogenerated carriers appearing in the TA spectrum at shorter wavelengths (λ_{probe} < 660 nm) is absent here, because it was subtracted in the calculation of the differential spectrum (Eq. 4.3).

4.3.3 EDA spectra and dynamics

The EDA spectra at selected times after pump excitation are shown in Figure 4.3. At a delay time of $\leq$ 0 ps, the pump pulse has not yet generated charge carriers, and therefore, the EDA and steady-state EA spectra are identical. The inset of Figure 4.3 shows the EDA
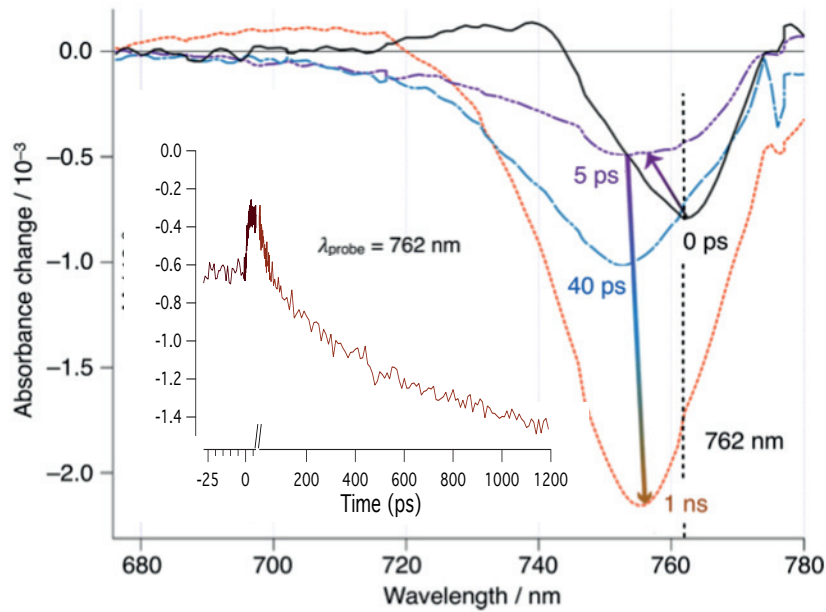
Figure 4.3 -. Time evolution of the electromodulated differential absorption (EDA) spectra of insulated MAPbI$_3$ films excited at λ_{pump} = 545 nm and subjected to an external electric field $|E|_0$ = 9.4 × 10^4 V cm^{-1} (U = 6 V). Inset: Time dependence of the differential absorbance change recorded under the same conditions at λ_{probe} = 762 nm.

dynamics monitored at 762 nm. We observe flat dynamics between – 30 to 0 ps, which is prior to the arrival of the pump pulse but the externally applied field is still present over this time period. This indicates that there are no spectral changes occurring due to the applied field occurring over these time scales. If ion migration is induced by the applied electric field, causing a change in the absorption of the material, this must take place on a time scale that exceeds the 100-μs period during which the electric field is applied to the sample. Hence, any effect of ionic migration is not significant for our measured EDA dynamics over the investigated 1ns timescale.

After pump excitation, the photogenerated electrons and holes in the perovskite layer drift toward the oppositely biased electrodes. The carrier separation produces a space

charge and a transient electric field E_s that opposes the steady field E_0 applied between the electrodes. It reduces the effective field strength, $|E_{eff}| = |E_0| - |E_s|$, exerted on the MAPbI$_3$ film and consequently decreases the amplitude of the electroabsorption. The EDA signal dynamics depends on the carrier's drift velocity and hence on their mobility. EDA dynamics monitored at the peak of the negative band associated with the Stark shift (inset of Figure 4.3) shows a decrease of the signal amplitude by approximately one-half at early times (< 5 ps) that can be attributed to the field-induced charge separation and the ensuing screening of the applied electric field exerted on the perovskite film. This initial carrier motion step is completed within 3 ps, at which point the EDA signal flattens out, indicating that there is no further rapid change in the effective field experienced by the material.

On a longer timescale, we observe that, after the initial decrease on the picosecond range, the amplitude of the transient negative signal increases with a half-reaction time of ca. 0.4 ns. The ingrowth in the bleaching band extends far beyond the initial amplitude at time zero resulting from the initially observed Stark effect and is accompanied by a 7 – 9 nm blue shift. This indicates that the slowly growing negative signal peaking at $\lambda_{probe} = 755$ nm is unrelated to the field-induced electroabsorption of the perovskite. This phenomenon, however, is observed only when the external electric field is applied and will be discussed in the following section.

Figure 4.4 compares TA and EDA signals obtained under similar conditions. Because no charge extraction from the insulated perovskite film is possible, the time evolution of the TA dynamics must result from carrier recombination. In the absence of an applied
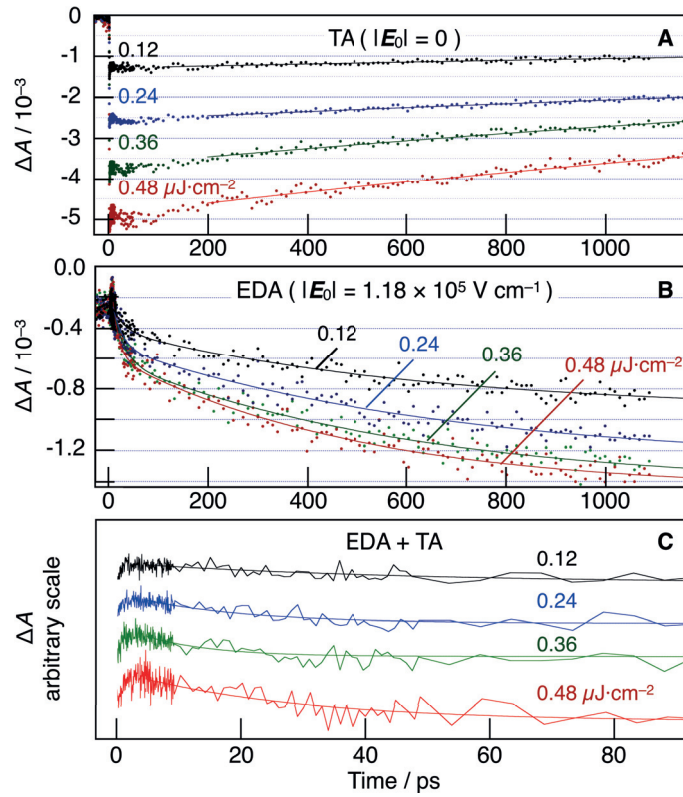
Figure 4.4 -Subnanosecond time evolution of the transient absorption (TA) and electromodulated differential absorption (EDA) signals recorded for increasing values of the energy fluences at λ_{pump} = 545 nm. (A) TA dynamics of carrier recombination in the absence of a field. (B) EDA dynamics obtained upon application of an external field of $|E|_0 = 6.2 \times 10^4$ V cm^{-1} (U = 4.0 V). (C) EDA dynamics after subtraction of the carrier recombination contribution (eq 4.5). The vertical positioning of the traces is arbitrary. All measured absorbance changes (TA and EDA) were averaged on the probe wavelength interval 749 nm $< \lambda_{probe} <$ 757 nm.

electric field, a decay of the ground-state bleaching is indeed observed, whose kinetics depends on the excitation pulse fluence and the resulting initial photogenerated carrier density (Figure 4.4A). Single-exponential fitting of the recombination dynamics yields time constants of τ_r = 5.2, 4.8, 3.4, and 3.4 ± 0.2 ns for pump energy fluences of Ψ = 0.12, 0.24, 0.36, and 0.48 µJ cm^{-2} per pulse, respectively. The energy fluence per excitation

pulse used in our experiments was kept at low values corresponding at most (Ψ = 0.48 $\mu J \cdot cm^{-2}$) to < 1 Sun[35] and an initial impulsive photocarrier density of $n_0 = 4.2 \times 10^{16}\,cm^{-3}$.

Rather than decaying, the EDA ground-state bleaching signal increases markedly after the initial 5 ps period with apparent biphasic dynamics (Figure 4.4B). Fitting of the slower kinetic component yields time constants quite similar to those extracted from the TA signals for carrier recombination. When the external electric field is applied, charge migration in opposite directions indeed prevents electron−hole recombination to a large extent. The suppression of the carrier recombination and the associated ground-state absorption recovery must result in a growing negative differential absorption in the EDA response that mirrors the decay of the TA, in terms of both kinetics and amplitude. This slow contribution is subtracted in Figure 4.4C by plotting:

EDA − (−TA)

$$\Delta A(t, \lambda) = A_{E+pump}(t, \lambda) - A(\lambda) \quad \textbf{Eq. 4.5}$$

The results reveal a fast kinetic component with a first-order time constant of τ = 24 ± 4 ps that is decoupled from both the initial signal growth assigned to the screening of the Stark effect at time delays shorter than 5 ps and the slow decay due to carrier recombination on the nanosecond time scale. This 24 ps component is attributed to the migration of carriers and accumulation at the two opposite film surfaces. Further charge separation should screen the electroabsorption more and thus produce an upward absorbance change signal. This contribution, however, is apparently overcompensated here by an increase of the bleaching of the material at the probe wavelengths, which

credibly results from a Burstein−Moss blue shift of the absorption threshold.[34,36] Because the two phenomena are characterized by the same time evolution, the combination of their respective signals yields the same kinetic parameter.

A closer look at the sum of the TA and EDA signals (appendix 4.2 – Figure A4.4) shows that the recombination dynamics is indeed completely suppressed for initial photocarrier densities of $n_0 \leq 2 \times 10^{16}$ cm^{-3}. At higher pump energy fluences ($n_0 \geq 3 \times 10^{16}$ cm^{-3}), however, a residual slow recovery of the ground-state absorption is still observed. This suggests that a portion of the more deeply trapped carriers were not separated by the electric field within the first tens of picoseconds and eventually recombined on a nanosecond time scale.

The interpretation of these results is schematized in Figure 4.5. Band-gap irradiation of MAPbI$_3$ perovskite at a pump wavelength of 545 nm generates out-of-equilibrium charge carriers. The application of an external field $|E|_0$ quickly separates charges over an initial distance corresponding to the size of crystal grains. Typical dimensions of such domains range from 5 to 100 nm (Figure 4.1). An average value of the grain length in the transverse direction was determined from several cross-sectional SEM images to be d = 40 nm. The initial decay of the electric field exerted on the material, as probed optically by the screening of the electroabsorption response, shows that the initial charge separation takes
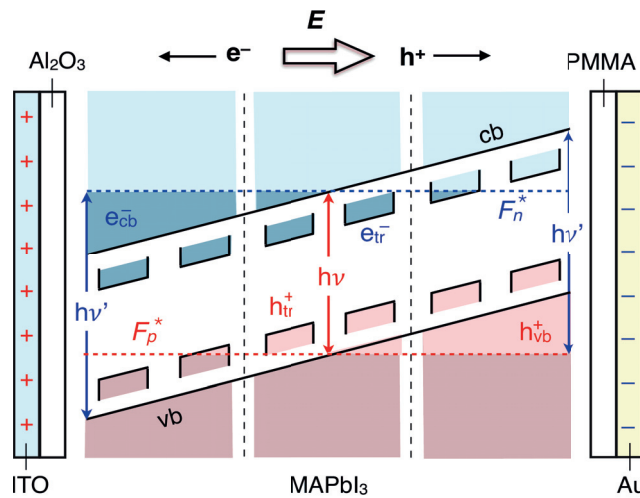

Figure 4.5 -Schematic showing how photogenerated charge carriers can accumulate at both surfaces of an insulated perovskite thin film within an externally applied electric field. Populated electronic states appear in dark blue for the conduction band (cb) and electron traps and dark pink for the valence band (vb) and hole traps. F_n^* and F_p^* are quasi-Fermi levels for electrons and holes, respectively, in the material under illumination. Accumulation of carriers causes a blue shift (hv' > hv) of the absorption threshold of the material.

place with a time constant of $\tau_1 = 0.94 \pm 0.1$ ps. (see Figure 4.6 (which zooms in on the short timescale dynamics shown in the inset of Figure 4.3)).

4.3.4 Evaluating the carrier drift mobility

The mobility μ of a charged particle migrating in an electric field is defined by:
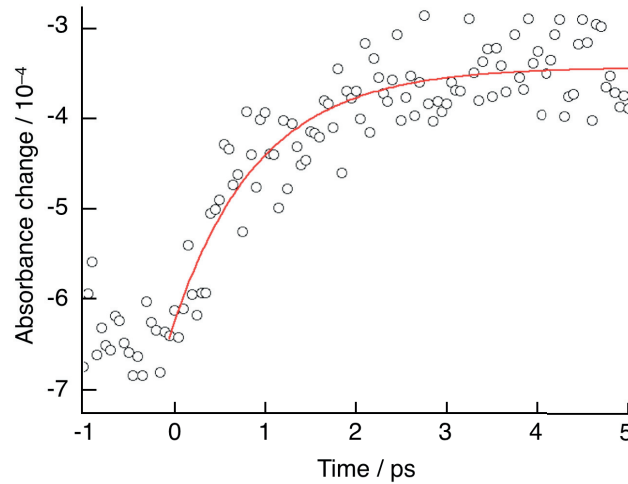
Figure 4.6 - Time-evolution of the electromodulated differential absorbance (EDA) signal recorded at λ_{probe} = 765 nm for a MAPbI$_3$ perovskite film submitted to an external electric field $|E|_0 = 9.4 \times 10^4$ V cm^{-1} upon ultrashort pulse irradiation at λ_{pump} = 545 nm. The red line drawn through the experimental points is the result of an exponential fit with a time constant of $\tau_1 = 0.94$ ps ± 0.1.

$$\mu \;=\; v \,/\, |E|_0 \qquad \textbf{Eq. 4.6}$$

where v is the drift velocity of the particle and $|\mathbf{E}|_0$ the electric field modulus. The drift velocity $v = L / \tau$ could in principle be estimated directly from the average transit distance L and time τ.

Absorbance changes resulting from the screening of the quadratic Stark effect by drifting charges or from the Burstein-Moss shift induced by the accumulation of carriers at the interfaces were shown to scale linearly with the pump energy fluence (appendix 4.2 – Figure A4.4). The time evolution of ΔA signals should then reflect the rate at which carriers reach the boundaries of the grain or of the entire film they moved across. The carrier transit time is spread by the initial spatial distribution of the carriers, as well as by possible dispersive transport and charge trapping processes. Figures 4.6 and 4.4C showed that the transient absorbance signal could be fitted in both cases by a single exponential of the form $\Delta A = b \cdot \exp(-kt) + c$, from which an average carrier transit time $\tau_1 = L / k$ was estimated. Assuming that the drift velocity is constant, $v = L / \tau$ can be calculated, provided a reasonably accurate average transit distance (L) is evaluated.

4.3.4.1   Effective external field

The model for the electric field drop across the perovskite layer was developed in collaboration with Dr. Guido Rothenberger. The three-layered insulated perovskite film Al_2O_3 (30 nm)| $MAPbI_3$ (280 nm) | PMMA (30 nm) can be modelled as three capacitors in series. A detailed description of the calculation of the field drop across the perovskite layer is presented in appendix 4.3. Taking into account the permittivity of the $MAPbI_3$

film as well as those of the two insulating layers, the magnitude of the electric field experienced by the perovskite material was calculated to be $|E|_0 = 0.44*U/d$, where U is the voltage applied between the ITO and gold electrodes and $d = 280 \pm 20$ nm is the perovskite film thickness (Eq. A4.6, appendix 4.3). A voltage of $U = 6.0$ V applied across the whole device would hence corresponds to an electric field intensity of $|E|_0 = 9.4 \pm 0.8 \times 10^4$ V cm^{-1}.

4.3.4.2   Average transit distance of carriers

Contrary to the conventional time-of-flight method, where the penetration depth of the pump light is generally small compared to the thickness of the sample and the initial photocarrier distribution can be considered as a quasi-two-dimensional sheet, the extended absorption profile within the perovskite material results in an initial gradient of carrier concentration in the depth of the irradiated film. The average transit distance for electrons and holes can be estimated from the coordinate of the centre of mass of carriers generated by the excitation laser pulse.

Let us consider a film of perovskite of thickness L, irradiated through the ITO glass substrate and the Al_2O_3 insulating layer from the left. The light transmittance profile across the material is given by Lambert's law:

$$I(x) = I_0 . \exp(-\alpha x) \qquad \textbf{Eq. 4.7}$$

where $I(x)$ is the light intensity transmitted at a depth x and α the absorption constant of the material. An absorption constant $\alpha = 6.4 \times 10^4$ cm^{-1} at $\lambda = 545$ nm was obtained

from the measured transmittance spectrum of a film of MAPbI$_3$ of known thickness. Based on eq. 4.7 The transmittance profile through the 280nm MAPbI$_3$ layer is given in Figure 4.7A.

Details for the calculation of the centre of mass for carriers generated by the laser pulse are given in Appendix 4.4. Using $\alpha = 6.4 \times 10^4 \text{ cm}^{-1}$ and L = 280 nm, the abscissa of the centre of mass of the carriers initially generated by light in the perovskite is determined from Eq. A 4.11(appendix 4.4) as being $\bar{x}$ = 82 nm. The average transit distance of electrons to the interface with Al$_2$O$_3$, therefore, is $l_n = \bar{x} - 0 = 82$ nm, while that of holes to the interface with PMMA is $l_p = L - \bar{x} = 198$ nm (Figure 4.7B). The initial drift of charge carriers upon ultrafast pulsed photogeneration takes place within individual crystal grains of the perovskite film, whose average length in the transverse direction is 40 nm. Using the same value of α and L = 40nm, the light transmittance of one grain is found to be 0.77. Equation Eq. A 4.11 returns an average transit distance for electrons and holes to the grain boundaries of 18 nm and 22 nm, respectively (Figure 4.8).

4.3.4.3 Calculating the carrier mobility
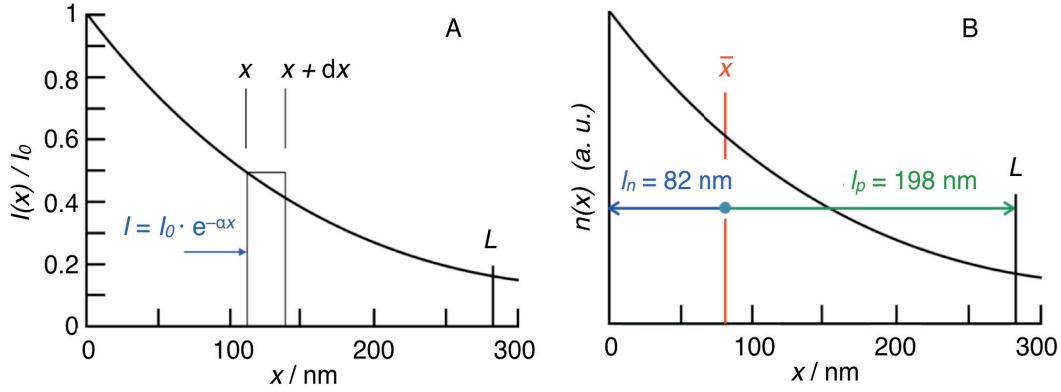
Figure 4.7 - A) Calculated light transmittance profile of a 280 nm-thick MAPbI$_3$ film with α = 6.4×10^4 cm^{-1} at λ = 545 nm. B) The abscissa of the center of mass of photogenerated carriers yielded by Eq. A 4.11 is $\bar{x}$ = 82 nm.

A time constant τ = 0.94 ps was determined for intragrain carrier separation under a reverse bias U = 6.0 V. On the average, this corresponds to the time necessary for
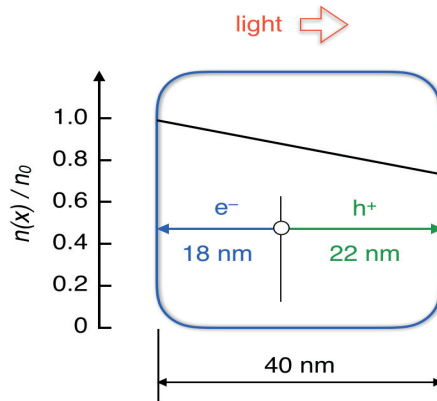
Figure 4.8 -Carrier density profile within a 40-nm MAPbI$_3$ crystal grain irradiated from the left with α = 6.4×10^4 cm^{-1}. The calculated average transit distance of electrons to the grain's surface is l_e = 18 nm, while that of holes is l_h = 22 nm.

photogenerated carriers to reach the grain boundaries from a position corresponding to their center of mass. Since there is no way to distinguish between electrons and holes, the transit distance to be used in the calculation of the drift velocity must be averaged over negative and positive charge carriers: $L_{\pm} = (L_n + L_p)/2 = 20$nm, leading to a drift velocity $v_{\pm} = L_{\pm}/\tau = 2.13 \times 10^6$ cm s^{-1} and an intragrain average mobility $\mu_{\pm} = v_{\pm}/|E|_0 = 22.6$ cm^2 V^{-1} s^{-1}. A relative uncertainty of the order of 10 % is estimated for the magnitude of the electric field and at most of 20% for the drift velocity. Consequently, the determined value of $\mu_{\pm}$ is marred by a maximum absolute error of ± 4 cm^2 V^{-1} s^{-1}.

As the photogenerated charge carriers further migrate toward the oppositely biased electrodes, they accumulate at the interface with insulating layers, forming n- and p-doped regions at the surface of the perovskite film. A Burstein−Moss blue shift of the MAPbI$_3$ absorption spectrum owing to the carriers' accumulation was observed to build up with a time constant $\tau_2 = 24 \pm 4$ ps under a bias voltage of 4.0 V. Because the observed Burstein−Moss shift of the absorption edge of the semi- conductor can result from the accumulation of only one specific type of carrier (Figure 4.5), the transit time measured in this case must be related to the type of carrier that is the first to reach an interface. Assuming that the accumulation of electrons in MAPbI$_3$ at the proximity of the alumina layer is responsible for the growing in of the bleaching signal, a value for the mobility of the negative charge carriers of $\mu_n = L_n/(\tau|E|_0) = 5.5 \pm 1$ cm^2 V^{-1} s^{-1} is calculated. Alternatively, if holes are the first to accumulate at the interface between the perovskite film and PMMA, their mobility would be determined as $\mu_p = 13.3 \pm 2$ cm^2 V^{-1} s^{-1}. In the latter hypothesis, the mobility of the electrons, $\mu_n < 5.5$ cm^2 V^{-1} s^{-1}, would be ca. 3 times

smaller than that of the holes. Retention of negative carriers in deeper traps could provide a rationale for this difference. However, if the first assumption is true, namely, that electrons are the first to accumulate and cause the bleaching signal, a value of $\mu_p < 13$ $cm^2 V^{-1} s^{-1}$ would be implied, which is compatible with an electron-to-hole mobility ratio of ~2 ($\mu_p \approx 3$ $cm^2 V^{-1} s^{-1}$) determined by terahertz and microwave photoconductivity measurements[37,38] and predicted by computational calculations.[39,40] In both cases, if a mobility averaged over electrons and holes of $\mu_{\pm} = (\mu_n + \mu_p) / 2 = L / (2\tau |E|_0) = 9.4 \pm 2$ $cm^2 V^{-1} s^{-1}$ is considered, one observes that the drift mobility of carriers along their path across the multigrain film is reduced at least by a factor of 2−4 compared to the intragrain, averaged mobility. This indicates the significant limitation of the drift velocity of carriers across the polycrystalline film by scattering at grain boundaries.[41,42]

To quickly summarize our calculated mobility values so that we can bring them together with the THz mobility calculated in chapter 3: with the EDA measurements we calculated an intragrain mobility of 22.6 ± 4 $cm^2 V^{-1} s^{-1}$, along with a film and carrier averaged mobility of 9.4 ± 2 $cm^2 V^{-1} s^{-1}$. Our calculated OP-THz probe mobility for the MAPbI$_3$ film was 41 ± 3 $cm^2 V^{-1} s^{-1}$. For a quick recap, due to the high frequency of the THz probe we calculate the carrier mobilities over very short distances. Hence the values we calculate using THz spectroscopy would be near the intrinsic values for the material. Taking this into account, we see that the granular film morphology and poor quality of the perovskite crystals that form the perovskite film substantially reduces the long range carrier mobility. Not taking into account grain boundaries, we see that scattering of carriers through defects present within the 40nm large grains already takes a toll on the

mobility, with the intragrain mobility being reduced by $\approx 1/2$ relative to the calculated THz mobility. While average mobility of carriers traversing the length film being $\approx 1/4$ of the intrinsic value. We see that the effective mobility of carriers being transported across the polycrystalline film is drastically affected by the presence of grain boundaries and defects, which act as scattering and recombination centers of mobile charge carriers.

4.3.5 Accumulation of electrons at the MAPbI$_3$ | mp-TiO$_2$ junction

In an attempt to discriminate between the respective contributions of electrons and holes, we carried out preliminary EDA measurements of thin films of evaporated MAPbI$_3$ in an architecture that would allow charge extraction at both electrodes. The measurement of the uninsulated perovskite sample was conducted by Vytenis Pranculis. The investigated sample had the alumina insulator replaced by a thin mesoporous nanocrystalline TiO$_2$ layer between the ITO conductive glass substrate and the perovskite. On the cathode side, the PMMA insulating layer was omitted, and gold was evaporated directly on top of the MAPbI$_3$ film. The U = 4.0 V reverse bias applied in this case was expected to make the TiO$_2$ act as an effective electron-transport layer, whereas holes would be readily extracted at the gold electrode. Similarly, to the case of the insulated perovskite film, screening of the externally applied electric field by intragrain carrier separation was observed to take place within a few picoseconds (see Figure 4.6).
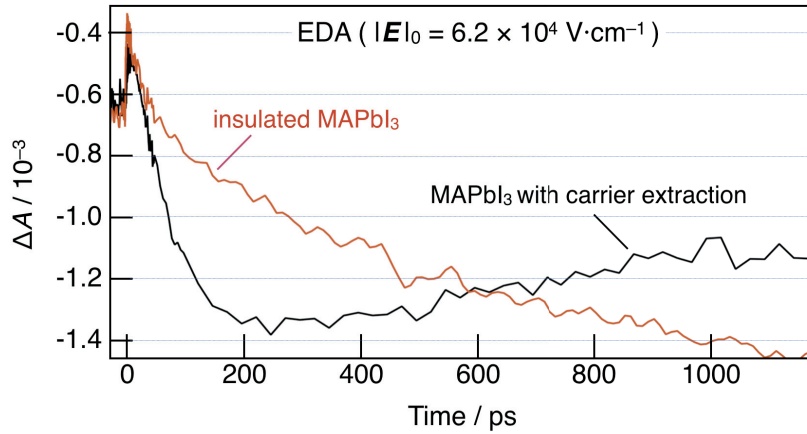
Figure 4.9 - Sub-nanosecond time-evolution of the electromodulated differential absorption (EDA) dynamics obtained upon application of an external electric field $|E|_0 = 6.2\times 10^4$ V· cm^{-1} (U = 4.0 V, reverse bias) on an insulated MAPbI$_3$ perovskite film (red trace) and a solar cell constituted of the same material in contact with a mesoporous TiO$_2$ layer on one side and evaporated gold on the other side (black trace).

Following this early decrease of the electroabsorption response, a growing bleaching signal with time constant of ~20 − 50 ps was monitored again, which was indicative of carrier accumulation at one or both interfaces. A slow recovery of the ground-state absorption of the perovskite was finally observed with a half-reaction time of $t_{1/2} \approx 300$ ps. The latter kinetic component was absent in insulated devices and is therefore assigned to the slow injection of accumulated carriers through one of the interfaces. A poor junction between the mesoporous titania and the polycrystalline vapor-deposited perovskite is expected, owing to rather sparse punctual contacts between the TiO$_2$ spherical particles and the nanometer-sized angular grains of the perovskite. On the contrary, the evaporated gold film forms a conformal junction with the active layer. It is, therefore, very likely that the observed carrier accumulation and delayed extraction

concerns electrons at the $MAPbI_3|TiO_2$ interface. These observations highlight the importance considering the efficiency of carrier injection at the contacts. Which provides direction for future measurements that investigate the efficiency and rates of carrier extraction using different electron and hole acceptor materials.

4.4 Conclusion

We successfully applied the time-resolved electroabsorption spectroscopy (TREAS) technique to probe long range carrier transport dynamics in methylammonium lead triiodide perovskite films. The active material was prepared by vapor deposition and was demonstrated to be polycrystalline with an average grain size of 40 nm. On the application of an external electric field on the order of 10 MV m^{-1}, the $MAPbI_3$ films displayed a blue shift of their absorption edge at 780 nm, corresponding to a quadratic electroabsorption response compatible with both Stark and Franz−Keldysh−Aspnes models. The observed electroabsorption signal was leveraged to optically probe the time evolution of the local electric field experienced by the perovskite due to photogenerated charge carriers.

Electron−hole pairs were formed on above band-gap excitation of the perovskite using a monochromatic pump pulse at 545nm. Their initial spatial separation was observed from the EDA signal dynamics to take place with a time constant of 0.94 ± 0.1 ps, until charges were trapped at grain boundaries. An average intragrain dc mobility of the carriers of $\mu_{\pm} = 23 \pm 4$ cm^2 V^{-1} s^{-1} was extracted from this result, in good agreement with terahertz spectroscopy measurements.[38,40,43,44] A second charge separation step was observed optically with a time constant of 24 ± 4 ps. This kinetic component was assigned

to the de-trapping of carriers and their migration to the opposite insulated film surfaces, where they accumulated, producing a Burstein−Moss blue shift of the absorption spectrum of the MAPbI$_3$ material. A value of the mobility, limited by trapping−detrapping processes at grain boundaries, of $\mu_n = 5.5 \pm 1$ cm^2 V^{-1} s^{-1} was estimated for electrons drifting across the entire film thickness. A carrier averaged value of 9.4 ± 2 cm^2 V^{-1} s^{-1}. was calculated for the transport of electrons and holes across the film. In all cases the mobilities we obtained were lower than the intrinsic mobility calculated using THz spectroscopy by a factor of $2 - 4$. Using the TREAS technique we were able link the reduction in the intrinsic mobility value to the film morphology. This was achieved by monitoring the evolution of the carrier's mobility in the picosecond regime and identifying the spectral signatures associated with carrier screening of the externally applied field, the de-trapping of carriers and their accumulation at the perovskite interface.

The TREAS technique also allowed for the initial characterization of the kinetics of the carrier transfer between the perovskite absorber material and carrier-extracting layers in fully operational photovoltaic devices. In particular, electron accumulation at the junction between the vapor-deposited MAPbI$_3$ film and a mesoporous nanocrystalline TiO$_2$ layer was observed before the charge extraction could take place at the subnanosecond time scale. Efficient carrier extraction at the interface would have a large dependence on the quality of the physical contact at the interface and the energetics of the materials in contact. With poorly matched energetics or physical interconnectivity between at the interfaces resulting in the hindered extraction of one or both carriers, leading to their

accumulation and possible unbalanced carrier extraction from the perovskite. Our observations, in particular suggest that future work using TREAS to investigate the carrier transfer dynamics at the electron and hole accepting interfaces, with a variety of acceptor materials, are warranted.

4.5 Appendix

Appendix 4.1
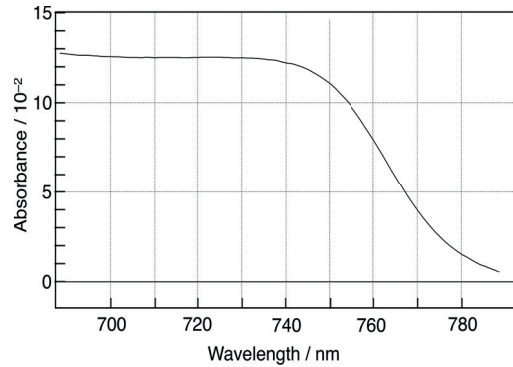
Figure A 4.2 - Absorbance spectrum near the absorption edge of a 280-nm-thick vapor-deposited MAPbI$_3$ film sandwiched between alumina and PMMA insulating layers (before thermal evaporation of gold on PMMA). Absorbance between 750 and 790 nm is due primarily to an excitonic absorption band.[30]
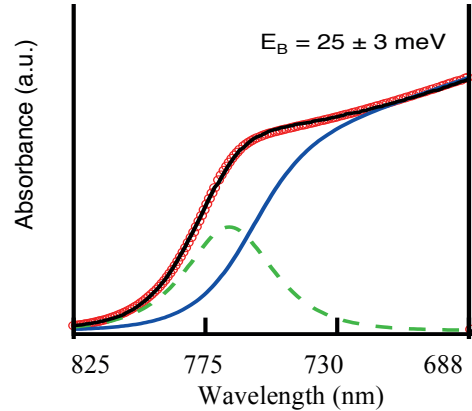

Figure A 4.2 –Taken from the chapter by Cadelano et al. in ref 30. The figure describes the contributions to the band edge absorption spectra in MAPbI$_3$ perovskite films. The red empty circles represent the theoretical fits to the experimental data (continuous black lines). The contributions to the absorption due to both excitonic and band-to-band transitions are modelled. The dotted green lines are relative to excitonic transitions, while the continuous blue lines are relative to band-to-band contributions with the inclusion of Coulomb interactions between electrons and holes.

Appendix 4.2
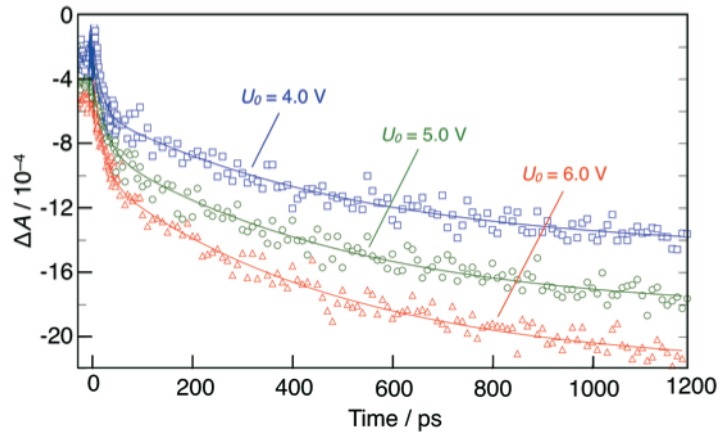
Figure A 4.3 -Time-evolution of EDA recorded for increasing values of the applied voltage U_0. Measured absorbance changes were averaged on a probe wavelength interval 749 nm $\leq$ $\lambda_{probe} \leq$ 757 nm. The pump excitation was at λ = 545 nm, with a constant energy fluence 0.48 μJ cm^{-2}. Continuous curves drawn through experimental points are the result of the fit of a double exponential function.
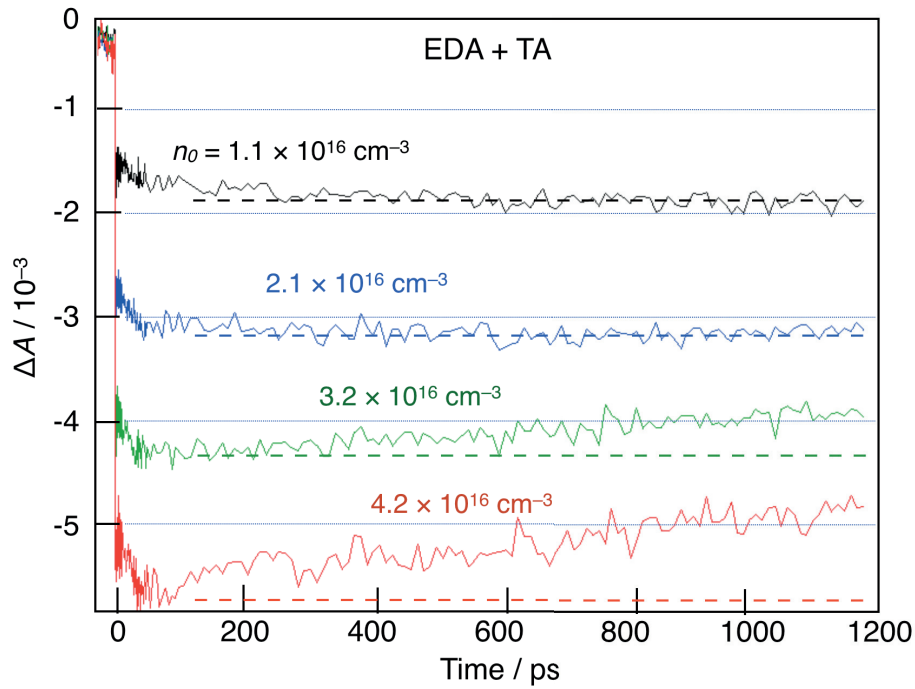
Figure A 4.4 -Summation of the electromodulated differential absorption (EDA, $U_0 = 4.0$ V) and transient absorption (TA) signals recorded for increasing values of the pump energy fluences. Labels above the traces correspond to the initial photocarrier densities n_0 achieved by each pump pulse. All measured absorbance changes (TA and EDA) were averaged on a probe wavelength interval 749 nm $\leq \lambda_{probe} \leq$ 757 nm.

Figure A4.4 displays the dependence of the summation of the electromodulated differential absorption (EDA) and transient absorption (TA) signals $\Delta A = \Delta A$ (EDA) − { $-\Delta A$ (TA) } upon the pump energy fluence. The slow dynamics observed in Figure A4.4 with $\tau_r = 500$ ps is only partially perceptible at high fluences, showing that the carrier recombination is entirely suppressed for $n_o \leq 2 \times 10^{16}$ cm^{-3}.

Appendix 4.3
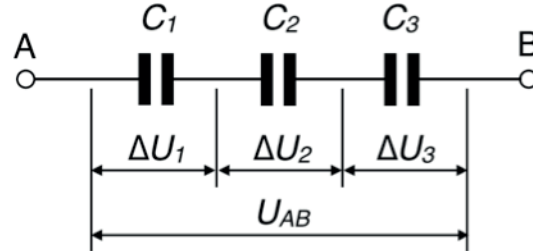
Figure A 4.5 - Equivalent circuit of the MAPbI$_3$ film in the dark (C_2), sandwiched between alumina (C_1) and PMMA (C_3) dielectric layers.

Capacitance in a parallel plate capacitor is governed by the following equation:

$$C = \varepsilon_0 \cdot \varepsilon \cdot S / d \qquad \textbf{Eq. A 4.1}$$

where ε_0 is the vacuum permittivity constant, ε the real part of the relative permittivity of the dielectric medium, S the area of the parallel plates and d the distance between them.

The voltage drop, ΔU, across each capacitor depends on the values of the individual capacitances. By applying Kirchoff's voltage law to the above circuit, it comes:

$$U_{ab} = \Delta U_1 + \Delta U_2 + \Delta U_3 \qquad \textbf{Eq. A 4.2}$$

$$\Delta U_1 = \frac{Q}{C_1} \quad \Delta U_2 = \frac{Q}{C_2} \quad \Delta U_3 = \frac{Q}{C_3} \qquad \textbf{Eq. A 4.3}$$

where Q is the charge stored in each capacitor. Since the total charge stored in the group of three capacitors in series is also Q, one gets:

$$Q = C_{tot} \cdot U_{ab} = C_i \cdot \Delta U_i \qquad \textbf{Eq. A 4.4}$$

$$\frac{1}{C_{tot}} = \frac{U_{AB}}{Q} = \frac{1}{C_1} + \frac{1}{C_2} + \frac{1}{C_3} \qquad \textbf{Eq. A 4.5}$$

$$\Delta U_i = U_{AB} \cdot \frac{C_{tot}}{C_i} = U_{AB} \cdot \frac{1}{C_i} \cdot \frac{1}{\sum_i \frac{1}{C_i}} = U_{AB} \cdot \frac{d_i}{\varepsilon_i} \cdot \frac{1}{\sum_i \frac{d_i}{\varepsilon_i}} \qquad \textbf{Eq. A 4.6}$$

The thickness of each layer was measured by taking several cross-sectional SEM images, yielding on the average $d_1 = d_3 = 30$ nm and $d_2 = 280$ nm. The relative permittivity of each of the three dielectric materials was more difficult to assess, as a rather broad distribution of values can be found in the literature. $MAPbI_3$ was shown to be characterized by a large static relative permittivity, due in particular to ionic movement and molecular dipole contributions from the organic cation.[45,46] In our case, though, the field is applied in the form of a square pulse voltage for only 100 μs, preventing the slow polarization of the material by ion migration. A moderate isotropic average dielectric constant in the range of 20-30 at a frequency of 10^4-10^5 Hz is believed to better describe the material in conditions prevailing in our experiments. In the following, we will then assume a relative permittivity $\varepsilon_2 = 25$.[46] For ALD-coated alumina, $\varepsilon_1 = 9$ measured at a frequency of 1 MHz was taken from reference.[47] PMMA, like numerous organic solids, has a relative permittivity ranging between 2.5 and 3. A value $\varepsilon_3 = 2.7$, measured at a frequency of 1 MHz, was used for our calculation.[48]

Inserting the above numerical values in equation Eq. A4.6, the voltage drop across the respective Al_2O_3, perovskite, and PMMA films was calculated as being $\Delta U_1 = 0.13 \cdot U_{AB}$,

147

$\Delta U_2 = 0.44 \cdot U_{AB}$, and $\Delta U_3 = 0.43 \cdot U_{AB}$ (see Figure S3). Hence, for voltage biases $U = 6.0$ V and $U = 4.0$ V applied onto the triple-layer system, the effective external electric field exerted onto the perovskite film in the dark was:

$|E|_0 = 0.44 \cdot U / d_2 = 0.44 \cdot 6.0 \text{ V} / 280 \times 10^{-7} \text{ cm} = 9.4 \times 10^4 \text{ V cm}^{-1}$ and

$|E|_0 = 0.44 \cdot U / d_2 = 0.45 \cdot 4.0 \text{ V} / 280 \times 10^{-7} \text{ cm} = 6.2 \times 10^4 \text{ V cm}^{-1}$, respectively.

Appendix 4.4

Let us consider a film of perovskite of thickness L, irradiated through the ITO glass substrate and the Al_2O_3 insulating layer from the left. The light transmittance profile across the material is given by the Lambert's law:

$$I(x) = I_0 . \exp(-\alpha x) \qquad \textbf{Eq. A 4.7}$$

The density of carriers $dn(x)$ photogenerated within a slice of infinitesimal thickness dx between the coordinates x and $x + dx$ can be written:

$$dn(x) = I(x) - I(x+dx) = I(x).[1 - \exp(-\alpha.dx) \qquad \textbf{Eq. A 4.8}$$

The latter expression can be simplified by using the first two terms of the Maclaurin series expansion:

$$\exp(-\alpha.dx) \approx 1 - \alpha.dx \longrightarrow dn(x) = I(x). \alpha.dx \qquad \textbf{Eq. A 4.9}$$

Applying again the Lambert's law, the carrier density at the coordinate x can be expressed by:

$$dn(x) = \alpha.I_0 . \exp(-\alpha.x) \, dx \qquad \textbf{Eq. A 4.10}$$

The abscissa x of the centre of mass of photogenerated carriers is finally provided by the expression:

$$\bar{x} = \frac{\displaystyle\int_0^L x \cdot \exp(-\alpha x)\,dx}{\displaystyle\int_0^L \exp(-\alpha x)\,dx} = \frac{\dfrac{1}{\alpha} - \left(L + \dfrac{1}{\alpha}\right)\cdot\exp(-\alpha L)}{1 - \exp(-\alpha L)} \qquad \textbf{Eq. A 4.11}$$

An absorption constant $\alpha = 6.4\times10^4$ cm^{-1} at $\lambda = 545$ nm was obtained from the measured transmittance spectrum of a film of MAPbI$_3$ of known thickness deposited on a quartz substrate. Using the latter value and $L = 280$ nm, the abscissa of the center of mass of the carriers initially generated by light in the perovskite is determined from Eq A4.11 as being $x = 82$ nm. The average transit distance of electrons to the interface with Al$_2$O$_3$, therefore, is $l_n = x - 0 = 82$ nm, while that of holes to the interface with PMMA is $l_p = L - x = 198$ nm. (Figure 4.7B)

The initial drift of charge carriers upon ultrafast pulsed photogeneration takes place within individual crystal grains of the perovskite film, whose average length in the transverse direction is 40 nm. Using again $\alpha = 6.4\times10^4$ cm^{-1} at $\lambda = 545$ nm, the light transmittance of one grain is found to be 0.77. Equation 4.11 returns an average transit distance for electrons and holes to the grain boundaries of 18 nm and 22 nm, respectively (Figure 4.8).

4.6 Bibliography

1.   Tress, W. Understanding the rate-dependent J – V hysteresis, slow time component, and aging in CH3NH3PbI3 perovskite solar cells: the role of a compensated electric field. *Energy & Environmental Science* **8,** 995–1004 (2015).

2.   Snaith, H. J. *et al.* Anomalous Hysteresis in Perovskite Solar Cells. *J. Phys. Chem. Lett.* **5,** 1511–1515 (2014).

3.   Kim, H.-S. & Park, N.-G. Parameters affecting I–V hysteresis of CH3NH3PbI3 perovskite solar cells: effects of perovskite crystal size and mesoporous TiO2 layer. *J. Phys. Chem. Lett.* **5,** 2927–2934 (2014).

4.   Meloni, S. *et al.* Ionic polarization-induced current-voltage hysteresis in CH3NH3PbX3 perovskite solar cells. *Nat Comms* **7,** 10334 (2016).

5.   Eames, C. *et al.* Ionic transport in hybrid lead iodide perovskite solar cells. *Nat Comms* **6,** (2015).

6.   Yang, T. Y., Gregori, G., Pellet, N., Grätzel, M. & Maier, J. The Significance of Ion Conduction in a Hybrid Organic–Inorganic Lead-Iodide-Based Perovskite Photosensitizer. *Angewandte Chemie* **127,** 8016–8021 (2015).

7.   Kim, J., Lee, S.-H., Lee, J. H. & Hong, K.-H. The Role of Intrinsic Defects in Methylammonium Lead Iodide Perovskite. *J. Phys. Chem. Lett.* **5,** 1312–1317 (2014).

8.   Azpiroz, J. M., Mosconi, E., Bisquert, J. & De Angelis, F. Defect migration in methylammonium lead iodide and its role in perovskite solar cell operation. *Energy & Environmental Science* **8,** 2118–2127 (2015).

9.   Du, M. H. Efficient carrier transport in halide perovskites: theoretical perspectives. *Journal of Materials Chemistry A* **2,** 9091–9098 (2014).

10.   Wu, X. *et al.* Trap States in lead iodide perovskites. *J. Am. Chem. Soc.* **137,** 2089–2096 (2015).

11.   Wang, L., McCleese, C., Kovalsky, A., Zhao, Y. & Burda, C. Femtosecond Time-Resolved Transient Absorption Spectroscopy of CH3NH3PbI3 Perovskite Films: Evidence for Passivation Effect of PbI2. *J. Am. Chem. Soc.* **136,** 12205–12208

(2014).

12. deQuilettes, D. W. *et al.* Impact of microstructure on local carrier lifetime in perovskite solar cells. *Science* **348,** 683–686 (2015).

13. Guo, Z., Manser, J. S., Wan, Y., Kamat, P. V. & Huang, L. Spatial and temporal imaging of long-range charge transport in perovskite thin films by ultrafast microscopy. *Nat Comms* **6,** 7471 (2015).

14. Draguta, S. *et al.* Spatially Non-uniform Trap State Densities in Solution-Processed Hybrid Perovskite Thin Films. *J. Phys. Chem. Lett.* **7,** 715–721 (2016).

15. Katayama, T., Jinno, A., Takeuchi, E., Ito, S. & Endo, M. Inhomogeneous Deactivation with UV Excitation in Submicron Grains of Lead Iodide Perovskite-based Solar Cell as Revealed by Femtosecond Transient Absorption *J. Phys. Chem. Lett.* (2014).

16. Salim, T. *et al.* Perovskite-based solar cells: impact of morphology and device architecture on device performance. *Journal of Materials Chemistry A* **3,** 8943–8969 (2015).

17. Nie, W. *et al.* Solar cells. High-efficiency solution-processed perovskite solar cells with millimeter-scale grains. *Science* **347,** 522–525 (2015).

18. Srimath Kandada, A. R. & Petrozza, A. Photophysics of Hybrid Lead Halide Perovskites: The Role of Microstructure. *Acc. Chem. Res.* **49,** 536–544 (2016).

19. Chen, Y., Peng, J., Su, D., Chen, X. & Liang, Z. Efficient and balanced charge transport revealed in planar perovskite solar cells. *ACS Appl Mater Interfaces* **7,** 4471–4475 (2015).

20. Shi, D. *et al.* Solar cells. Low trap-state density and long carrier diffusion in organolead trihalide perovskite single crystals. *Science* **347,** 519–522 (2015).

21. Vithanage, D. A. *et al.* Visualizing charge separation in bulk heterojunction organic solar cells. *Nat Comms* **4,** (2013).

22. Gélinas, S. *et al.* Ultrafast Long-Range Charge Separation in Organic Semiconductor Photovoltaic Diodes. *Science* **343,** 512–516 (2014).

23. Devižis, A. *et al.* Dissociation of Charge Transfer States and Carrier Separation in Bilayer Organic Solar Cells: A Time-Resolved Electroabsorption Spectroscopy

Study. *J. Am. Chem. Soc.* **137,** 8192–8198 (2015).

24.   Tétreault, N. *et al.* (Invited) Atomic Layer Deposition for Novel Dye-Sensitized Solar Cells. *ECS Trans.* **41,** 303–314 (2011).

25.   Im, J.-H., Lee, C.-R., Lee, J.-W., Park, S.-W. & Park, N.-G. 6.5% efficient perovskite quantum-dot-sensitized solar cell. *Nanoscale* **3,** 4088–4093 (2011).

26.   Teuscher, J., Ulianov, A., Müntener, O., Grätzel, M. & Tétreault, N. Control and Study of the Stoichiometry in Evaporated Perovskite Solar Cells. *ChemSusChem* **8,** 3847–3852 (2015).

27.   Liu, M., Johnston, M. B. & Snaith, H. J. Efficient planar heterojunction perovskite solar cells by vapour deposition. *Nature* **501,** 395–398 (2013).

28.   Roiati, V. *et al.* Stark Effect in Perovskite/TiO$_2$ Solar Cells: Evidence of Local Interfacial Order. *Nano Lett.* **14,** 2168–2174 (2014).

29.   Trinh, M. T., Wu, X., Niesner, D. & Zhu, X.-Y. Many-body interactions in photo-excited lead iodide perovskite. *Journal of Materials Chemistry A* **3,** 9285–9290 (2015).

30.   Cadelano, M. *et al.* in *Perovskite Materials - Synthesis, Characterisation, Properties, and Applications* (InTech, 2016). 1–24

31.   Ziffer, M. E., Mohammed, J. C. & Ginger, D. S. Electroabsorption Spectroscopy Measurements of the Exciton Binding Energy, Electron–Hole Reduced Effective Mass, and Band Gap in the Perovskite CH$_3$NH$_3$PbI$_3$. *ACS Photonics* **3,** 1060–1068 (2016).

32.   Marchioro, A. *et al.* Unravelling the mechanism of photoinduced charge transfer processes in lead iodide perovskite solar cells. *Nature Photonics* **8,** 250–255 (2014).

33.   Sum, T. C. *et al.* Spectral Features and Charge Dynamics of Lead Halide Perovskites: Origins and Interpretations. *Acc. Chem. Res.* **49,** 294–302 (2016).

34.   Anand, B. *et al.* Broadband transient absorption study of photoexcitations in lead halide perovskites: Towards a multiband picture. *Phys. Rev. B* **93,** 161205 (2016).

35.   Azarhoosh, P., Frost, J. M., McKechnie, S., Walsh, A. & van Schilfgaarde, M. Relativistic origin of slow electron-hole recombination in hybrid halide perovskite

solar cells. *APL Materials* **4,** 091501 (2016).

36. Manser, J. S. & Kamat, P. V. Band filling with free charge carriers in organometal halide perovskites. *Nature Photonics* **8,** 737–743 (2014).

37. Ponseca, C. S. *et al.* Organometal halide perovskite solar cell materials rationalized: ultrafast charge generation, high and microsecond-long balanced mobilities, and slow recombination. *J. Am. Chem. Soc.* **136,** 5189–5192 (2014).

38. Ponseca, C. S., Jr & Sundström, V. Revealing the ultrafast charge carrier dynamics in organo metal halide perovskite solar cell materials using time resolved THz spectroscopy. *Nanoscale* **8,** 6249–6257 (2016).

39. Umari, P., Mosconi, E. & De Angelis, F. Relativistic GW calculations on CH3NH3PbI3 and CH3NH3SnI3 Perovskites for Solar Cell Applications. *Sci Rep* **4,** 4467 (2014).

40. Chen, Q. *et al.* Under the spotlight: The organic-inorganic hybrid halide perovskite for optoelectronic applications. *Nano Today* **10,** 355–396 (2015).

41. Stranks, S. D. *et al.* Recombination Kinetics in Organic-Inorganic Perovskites: Excitons, Free Charge, and Subgap States. *Physical Review Applied* **2,** (2014).

42. Trap States in Lead Iodide Perovskites. **137,** 2089–2096 (2015).

43. Karakus, M. *et al.* Phonon–Electron Scattering Limits Free Charge Mobility in Methylammonium Lead Iodide Perovskites. *J. Phys. Chem. Lett.* **6,** 4991–4996 (2015).

44. Shi, D. Low trap-state density and long carrier diffusion in organolead trihalide perovskite single crystals. *Science* **347,** 519–522 (2015).

45. Lin, Q., Armin, A., Nagiri, R. C. R., Burn, P. L. & Meredith, P. Electro-optics of perovskite solar cells. *Nature Photonics* **9,** 106–112 (2015).

46. Juarez-Perez, E. J. *et al.* Photoinduced Giant Dielectric Constant in Lead Halide Perovskite Solar Cells. *J. Phys. Chem. Lett.* **5,** 2390–2394 (2014).

47. Lin, Q., Armin, A., Nagiri, R. C. R., Burn, P. L. & Meredith, P. Electro-optics of perovskite solar cells. *Nature Photonics* **9,** 106–112 (2015).

48. Shekar, B. C., Sathish, S. & Sengoden, R. Spin coated nano scale PMMA films for organic thin film transistors. *Physics Procedia 2 ,* (2013).

5. Time-Resolved Electroabsorption Spectroscopy of Perovskite Solar Cells

5.1 Introduction

In this chapter we apply the TREAS technique to investigate state-of-the-art planar perovskite photovoltaic devices. The mixed perovskite, $(FAPbI_3)_{0.85}(MAPbBr_3)_{0.15}$, serves as the active photovoltaic layer and thin films of the material were previously investigated using THz spectroscopy in chapter 3. A short recap of the relevant results from chapter 3: carrier mobilities of $22 \pm 4 \ cm^2 \ V^{-1} \ s^{-1}$ at THz frequencies were extracted and Drude-like photoconductivity was observed. The improved morphology of the mixed perovskite film meant that there was significantly less carrier scattering at grain boundaries and defects relative to the $MAPbI_3$ film. As the next step, we use time resolved electroabsorption measurements to investigate carrier dynamics under applied electric fields in fully functional devices. We observe two distinct components in the field screening dynamics allowing us to distinguish between electron and hole transport to the interfaces. Our calculated macroscopic carrier mobilities are quite close to the high frequency mobility we calculate using THz spectroscopy, with the macroscopic mobility being diminished by a factor of 2, at most. This allows us to conclude that the significant improvements in morphology and crystal quality of the mixed perovskite film, results in similar macro and microscale carrier transport properties. Unlike the $MAPbI_3$ film investigated in chapter 4, where the high density of defects and grain boundaries resulted

in a reduction of the THz mobility by a factor of ≈ 4 for carrier transport across the polycrystalline film.

We are also able to directly compare the femtosecond transient absorption spectrum with the steady state electroabsorption spectrum. Our results indicate the presence of a photo-induced electroabsorption signal within 500 fs after pump absorption in TA measurements. This arises from the disassociation of a neutral excitonic species formed immediately after photoexcitation, into a free electron and hole. The electrostatic force between these point charges shifts the absorption of the surrounding material, resulting in a transient EA signal while the charges are in proximity.

5.2   Experimental

5.2.1   Sample preparation and device characterization

Devices used in this chapter were fabricated by Dr. Juan-Pablo Correa-Baena and Mahboubeh Hadadian. The mixed perovskite films were deposited according to the procedure described in chapter 3.2.1. The device architecture used is as follows - FTO | SnO_2 or mp-TiO_2 | perovskite | spiro-MeOTAD | Au. For the electron transport layer, either a thin 15nm SnO_2 layer deposited by ALD or a 200nm mp-TiO_2 layer deposited through spin coating on FTO coated glass were used. After the deposition of the perovskite layer, 220nm of spiro-MeOTAD was deposited on the perovskite by spin coating, finally 80nm of gold was evaporated. Further details of the fabrication procedure can be found in ref[1]. The morphology of the device was characterized using cross-sectional SEM measurements taken by Dr. Correa-Baena.

5.3   Results

### 5.3.1   Device characterization
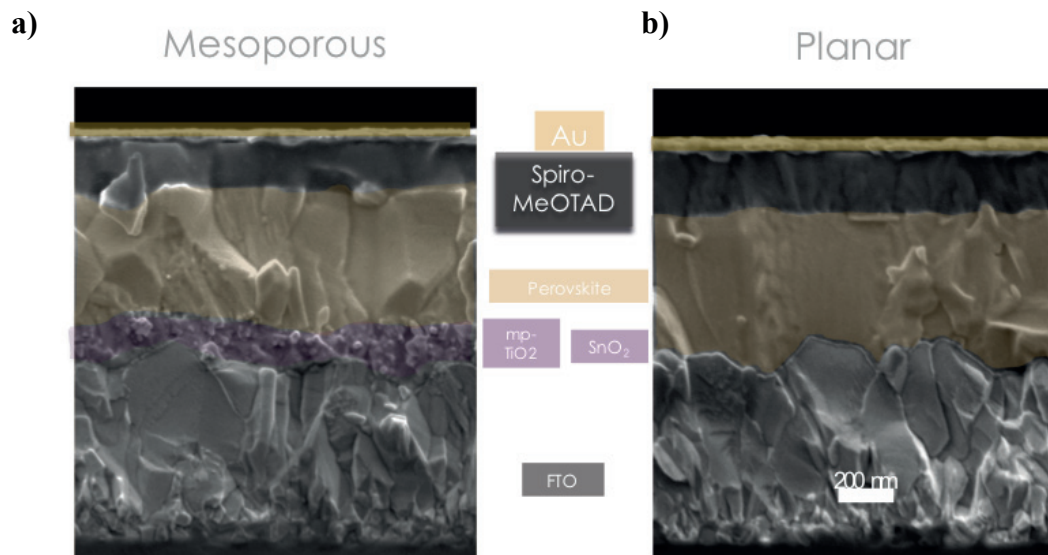
Figure 5.1 - Cross-sectional Scanning Electron Microscopy (SEM) image of a planar perovskite device with the respective layers from bottom to top: FTO | SnO_2 or TiO_2| perovskite | spiro-MeOTAD | Au (shaded in colour and annotated) The SnO_2 and TiO_2 acts as the electron selective layer (ESL).

An extensive study on devices based on the mixed perovskites has been published by Correa Banea *et al*.[1] The morphology and solar cell performance of our investigated devices were characterized prior to beginning the study. Cross sectional SEM images of the complete devices are presented in figure 5.1. Our investigations focused primarily on the completely planar devices that used a thin film of ALD deposited SnO_2 as the electron accepting layer (Figure 5.1b) and IV curves in the forward and reverse direction are presented in Figure 3.2b. The thickness of the perovskite layer estimated from the cross-sectional SEM images is 485 $\pm$ 50 nm. The device has a 15 nm thick SnO_2 electron

selective layer (ESL) that was deposited by ALD on a FTO coated substrate. A 220 nm spin coated, spiro-MeOTAD layer that acts as the hole transport layer. The entire device thickness is 715 ± 50 nm. Preliminary measurements on devices employing mp-TiO$_2$ as the electron transport layer were carried out and cross sectional SEM images of the device are presented in Figure 5.1b. The majority of the perovskite in the device exists as a ~ 500 nm perovskite layer which caps the 200 nm mp-TiO$_2$ layer with a small fraction of the total perovskite volume infiltrated within the pores of the mp-TiO$_2$.

5.3.2 Electroabsorption spectra
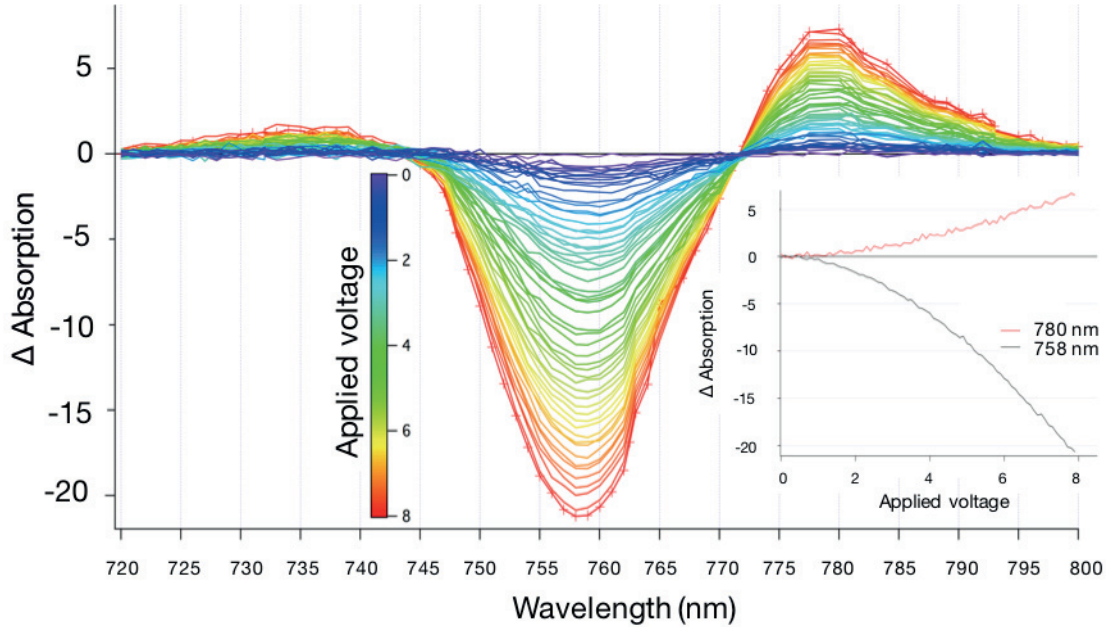
Figure 5.2 - Steady state electro-absorption (EA) spectra of the perovskite active layer in a planar SnO_2 photovoltaic device for applied voltages ranging from 0 to 8 V in reverse bias. Inset: Quadratic dependence of the differential absorbance measured at $\lambda_{probe} = 758$ and 780nm upon application of an external electric field (E).

The steady-state EA spectra of the perovskite layer in a working solar cell are shown in Figure 5.2 for a range of voltages from 0 V to 8 V in reverse bias. The voltage was applied across the FTO and gold electrodes using a function generator, setup to give square voltage pulses with 100 µs duration. Based on the measured thickness, we calculate the external electric field strength for an applied bias of 1 V across the device is $|\boldsymbol{E}|_0 = V / d = 1.4 \pm 0.1 \times 10^4$ V cm^{-1}. The voltage pulses were applied in reverse bias, in these conditions photo-generated carriers are efficiently extracted and carrier injection is negligible. EA spectra are obtained by calculating the differential absorption of the

broadband probe by modulating the applied field in a planar PSC and our observed absorbance change (ΔA) can be defined by Eq.4.2.

We observe on Figure 5.2 a negative ΔA at λ_{probe} = 745 - 772 nm, with a maximum amplitude at 758 nm along with a positive ΔA feature at λ_{probe} = 772 - 800nm and a weaker positive feature between 718 - 745 nm. The inset in Fig 5.2 shows the dependence of the EA amplitude with the applied voltage for the peaks at 758 nm and 780 nm. A quadratic dependence of the EA amplitude with the applied field was observed. With a good fit $\Delta A_{(758nm)} = -0.35E^2$ for the peak at 758nm. This dependence indicates that no permanent dipole exists within the sample and that the polarizability of the material is reasonably isotropic. The quadratic nature of the of EA response confirms that we probe the bulk perovskite material and that the EA signal we observe is not dominated by oriented dipoles at interfaces with SnO_2 that would lead to a linear dependence.[2,3] The sample with mp-TiO_2 could not be fit with a simple E^2 term and required a fit $\Delta A_{(762nm)} = -0.32E^{1.6}$ (Figure A5.1- appendix 5.1), indicating that there is a non-negligible linear contribution and that the EA shift is not predominantly quadratic in nature in the mp-TiO_2 sample. This behavior is due to the mix of oriented dipoles at the interface between mp-TiO_2 | perovskite and the bulk perovskite.[2]

5.3.3   Evaluating the carrier drift mobility

The absorbance change for the EDA spectra is defined by equation 4.3. The evolution of the EDA spectra as a function of time is presented in Figure 5.3. We excited the sample with a monochromatic pump pulse at a low excitation fluence of 0.1 μJ cm^{-2} (carrier density – $3x10^{15}$ cm^{-3}). Prior to the arrival of the pump excitation pulse the observed spectra (time = 0 ps, black trace) can be attributed entirely to the steady-state EA of the perovskite layer. Since charge carriers have not yet been created by the pump pulse they have no contribution to the screening and hence the EA and EDA spectra are identical. Photo-excitation by a short pump pulse with a wavelength of 600 nm generates electrons and holes within the perovskite layer. The photo-generated carriers subsequently drift to the oppositely charged electrodes. Carrier motion towards the electron and hole acceptor interfaces generates a transient electric field ΔE that opposes to the steady field E applied between the electrodes. It reduces the effective field $E_{eff} = |E| - |\Delta E|$ experienced by the
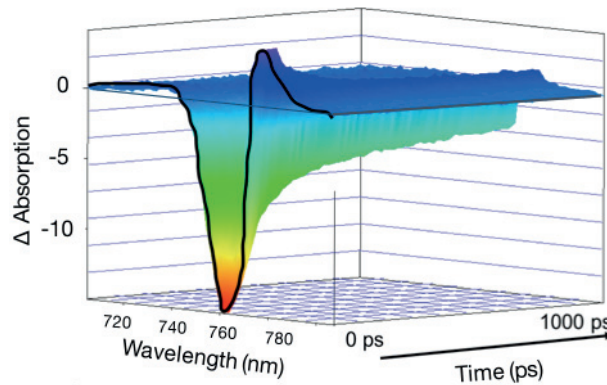

Figure 5.3 – Time-evolution of EDA spectra of perovskite cells excited at λ_{pump} = 600 nm, fluence = 0.2 μJ cm^{-2} and under application of an external electric field E = 4.9×10^4 V cm^{-1} (V_0 = 3.5 V).

perovskite film and consequently decreases the amplitude of the optical EA of the absorbance.[4] Therefore a decrease in the effective field experienced by the perovskite layer translates into a reduction of the EA signal with a time component that depends on both carrier motions to the interfaces.

The applied voltage pulses have a 100 μs duration which is shorter than the time scales for any significant ionic motion over the film thickness.[5] There is a 1.9 ms gap between each 100 μs voltage pulse which allows the system to completely recover to its ground state. We confirmed this by carrying out multiple temporal scans with the pump pulse at each applied voltage. The sequential scans overlapped indicating that there was no build-up of the perturbations caused by the applied electric field and optical pump between pulses. In the EDA measurements, prior to the arrival of the pump pulse (t = − 40 ps to t = 0 ps) we do not observe time dependence of the signal. This indicates that there is no measurable contribution of ionic motion on our measured time scales to the observed spectral dynamics.

By observing the dynamics of the EDA spectrum monitored at its peak amplitude (758 nm) we can extract the time taken for both carriers to reach their respective acceptor interfaces, since the EDA signal in time is due to the diminishing E_{eff} caused by carrier screening. These dynamics are shown in Figure 5.4 for three applied voltages. Increasing the applied bias from 1 to 3.5 V results in carriers within the perovskite layer travelling
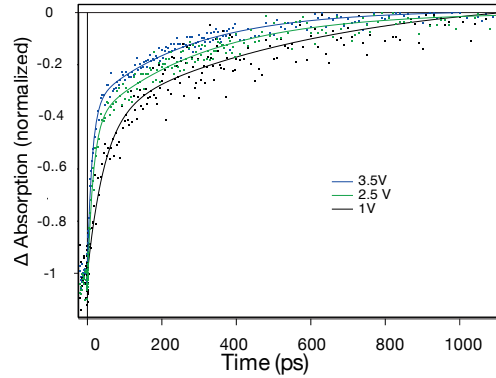
Figure 5.4 - Time-dependence of the differential absorbance change recorded for applied voltages of 3.5, 2.5 and 1 V, and probed at the peak of the EA signal at λ_{probe} = 758 nm, *fluence* = 0.1 $\mu J/cm^2$.

to the electrodes with a higher velocity, which is proportional to the increase of the field. The carrier drift velocity (υ_d) can in principle be estimated directly from the average transit distance of electrons and holes ($L_{e/h}$) and their transit time $\tau_{e/h}$. The drift velocity is directly proportional to the mobility (μ) and electric field ($\upsilon_d = \mu E$), hence υ_d increases with the applied voltage. This results in a more rapid screening of the applied electric field, as can be seen in Figure 5.4 through the faster signal decay at higher voltages. The dynamics have two separated time components. A first fast decay component, which takes between 13 (at 3.5V) – 47 ps (at 1V) and a second slower decay that takes between 261 (at 3.5V) – 782ps (at 1V) until a plateau of the signal amplitude after all the carriers reach the interface. We observe that an increase in the applied voltage results in an acceleration in the rate of decay for both the fast and slow components, with a change that is nearly proportional to the increase in voltage. We also carried out EDA measurements on samples with mp-TiO$_2$ as the electron acceptor (Appendix 5.3). The dynamics were

broadly similar to the those of the planar devices, however detailed mobility calculations are not carried out due to the convolution of carrier transport within the mp-TiO$_2$ and the bulk capping layer, which means we cannot reliably calculate the transport distance of carriers to the electrodes.

Samples are excited from the transparent FTO side and we measured an absorbance of 1.4 by the perovskite layer at the 600 nm pump excitation wavelength, meaning complete absorption of the excitation pulse (Appendix 5.1 - absorbance spectrum). Therefore the high absorbance of the perovskite layer results in an inhomogeneous distribution of photo-generated carriers that can be modelled with a beer-lambert profile.[6] The majority of the photo-generated carriers are formed in higher proximity to the transparent FTO electrode than at the gold back electrode. Assuming each absorbed photon forms a pair of free charge carriers (electron and hole) we calculated the weighted average distance that electrons (d_e) and holes (d_h) have to travel to reach their acceptor interfaces using the absorption profile modelled with the beer-lambert law (as previously outlined in appendix 4.4). Using $\alpha = 6.6$ x 10^4 cm^{-1} and a film thickness (L) of 485 nm, the average transit distance (calculated using Eq. A4.11 in appendix 4.4) of electrons travel is 131 nm to reach the SnO$_2$ interface, while holes travel an average of 354 nm to the spiro-MeOTAD interface. We assign the fast component to screening by electrons due to the higher proximity of their generation to their acceptor (SnO$_2$) interface, and the slower component to screening by holes travelling towards the spiro-OMeTAD interface. We consider this assumption to be reasonable, considering that the inverse (i.e. assigning the holes to the faster component and electrons to the slower one) would result in holes having a mobility ≈ 50 times larger than electrons. This would not fit with the significant number of

theoretical and experimental studies that demonstrate carrier mobilities that are more closely balanced. We used a biexponential function to fit the dynamics of the EA signal decay and extract time constants associated with the slow and fast components, for holes and electrons, respectively. Our model assumes that the electron and hole screening components are completely separated between the two time components. The presence of selective carrier traps would shift the total electric field screening contribution of the electrons or holes, in addition diffusive carrier transport could contribute to screening of the applied field. Table 1 compiles the rates extracted from the dynamics in Figure 5.4. The fitting amplitude of the fast component is 60%, which is near the 50% expected for equal screening contributions from electrons and holes.[7] We also note that the measurement with the lowest applied voltage has a slow component close to the investigated time window and therefore does not allow for precise determination of the associated time constant. This is further reflected in the uncertainty in the calculated value for hole mobility.

Carrier mobility is calculated using the weighted average distance, d_e and d_h, travelled by electrons and holes, the fitted time constants (t) and the applied electric field (E) using $\mu_{e/h} = d_{e/h} / (t * E)$. In order to calculate the effective external electric field exerted on the perovskite layer we model our device as three capacitors in series according to the analysis presented in Appendix 4.3. In order to calculate the voltage drop (ΔU) across each capacitor we require knowledge of the applied voltage (U), the thickness of the individual layers (L) and the relative permitivity (ε). U and L are easily obtained using the known applied voltage and the layer thickness (L) from the cross sectional SEM. The relative permittivity of the materials is harder to asses and range of values can be found

in literature. At higher frequencies, the electronic polarizability and reorientation of dipoles have the largest contributions, where the slower migration of ions and hopping charges do not play a significant role. For the ALD coated SnO_2 layer, the thickness d_1 = 15nm and the dielectric constant SnO_2 is taken as ε_1 = 10 from ref[8]. The perovskite layer had an average thickness d_2 = 485nm and a moderate relative permittivity of ε_2 = 25 which has been identified at frequencies of $10^4 - 10^5$ has been used.[9] The voltage pulse we apply is of 100 μs in duration and would be much shorter than the timescales associated with the slow polarization of the perovskite. The hole transport material (HTM), spiro-MeOTAD had an estimated layer thickness of d_3 = 220 nm, with a reported dielectric constant of ε_3 = 3 for pristine films. However, the composition of the hole conducting layer in state-of-the-art devices is a mixture of spiro-MeOTAD with additives, which in our case were Li-TFSI, FK209, and TBP[1]. The presence of additives would likely increase the effective dielectric constant of the hole transport layer, resulting in a larger effective external electric field exerted on the perovskite layer (according to Eq A4.6 in appendix 4.3).

To investigate the consequences of having a larger relative permittivity for the HTM, we consider two situations using ε_3 = 3 and a larger ε_3 = 8. The effective field experienced by the perovskite ($|E|_0$) using a ε_3 = 3 would be given by $|E|_0 = 0.20 \cdot U / d_2$ (U being the

---

[1] **Li-TFSI** - bis(trifluoromethylsulfonyl)- imide lithium salt
  FK209 -tris(2-(1H-pyrazol-1-yl)- 4-tert-butylpyridine)–cobalt(III) tris(bis(trifluoromethylsulfonyl)imide)
  TBP - 4-tert-butylpyridine

total externally applied voltage to the device). The value of 0.20 in the equation implies that the field strength experienced by the perovskite layer is 20% of the total field applied across the 715 nm thick device. Using $\varepsilon_3 = 3$, values for $|E|_0$ at different applied voltages, along with the calculated electron and hole mobilities are presented in table 1. For this case, the average electron mobility $\mu_n = 75 \pm 15$ cm^2 V^{-1} s^{-1} and $\mu_p = 11 \pm 3$ cm^2 V^{-1} s^{-1} for holes, the carrier averaged values for electrons and holes is $\mu_\pm = 43 \pm 9$ cm^2 V^{-1} s^{-1}. The uncertainty is associated with the roughness of the substrate (which results in an estimated perovskite thickness of $\pm$ 50nm) and the fitted time constants. The error propagation in our calculations results in the mobility values having an uncertainty of $\approx$ 20%.

voltage (V)	Applied field strength (E) x10^4 (V cm^{-1})	Fitted time constant (ps)		mobility cm^2 / (V.s)	
		Holes	*Electrons*	*Holes*	*Electrons*
1	0.4 ± 0.1	782 ± 337	47 ± 6	11 ± 6	68 ± 20
2.5	1 ± 0.1	310± 22	16 ± 1	12 ± 2	85 ± 13
3.5	1.4 ± 0.1	261 ± 15	13 ± 1	10 ± 2	74 ± 10

Table 1 – Mobility determination of holes and electrons at different applied field strengths and associated time constants for the hole and electron contributions of the field screening.

Using the higher relative permittivity $\varepsilon_3 = 8$ for the HTM, we obtain a much larger $|E|_0$, the calculated effective field experienced by the perovskite layer is 40% of the field applied across the entire device (i.e. $\approx$ x 2 relative to that for $\varepsilon_3 = 3$). The resulting

calculated mobilities would be $\mu_n = 37 \pm 7 \, cm^2 \, V^{-1} \, s^{-1}$ and $\mu_p = 6 \pm 2 \, cm^2 \, V^{-1} \, s^{-1}$ for holes, with $\mu_\pm = 22 \pm 5 \, cm^2 \, V^{-1} \, s^{-1}$. As we see, the value for the relative permittivity of the HTM does affect the calculated mobilities quite significantly. From our THz measurements, the mobility values we obtained were $\mu_\pm = 22 \pm 4 \, cm^2 \, V^{-1} \, s^{-1}$, the high frequency mobilities are near the intrinsic values for this film. The value of $\mu_\pm = 43 \pm 9 \, cm^2 \, V^{-1} \, s^{-1}$ that we calculated using $\varepsilon_3 = 3$, is the averaged mobility for transit across the length of the film and is significantly higher than the THz mobility and hence not compatible. Which indicates that the relative permittivity of the HTM is indeed higher. Using the larger value of $\varepsilon_3 = 8$, we obtain $\mu_\pm = 22 \, cm^2 \, V^{-1} \, s^{-1}$, which correlates between the THz and TREAS techniques and in this manner we can assign the lower bounds of the permittivity for the HTM as $\varepsilon_3 = 8$ and set the upper limit of $\mu_\pm$. The lower limit for $\mu_\pm$ can be determined by setting $\varepsilon_3 = \infty$ (which is of course not realistic, but allows us to define a limit for the mobility range), this results in $\mu_\pm = 10 \pm 2 \, cm^2 \, V^{-1} \, s^{-1}$. From this analysis we observe that the averaged mobility of carriers over their transit across the thickness of the film is at most reduced by a factor ≈ 2 relative to the THz mobility, with an intermediate value for $\mu_\pm$ between 10 to 22 $cm^2 \, V^{-1} \, s^{-1}$ being a reasonable assumption.

We see that the significant improvement in the morphological quality of the mixed perovskite films results in carrier mobilities that are near the intrinsic values obtained using THz spectroscopy. In the multigrain $MAPbI_3$ film that we previously investigated, the carrier mobility diminished by a factor of ≈ 4 over a transport distance of 280 nm. In the mixed perovskite however, the large grains are comparable in size to the layer thickness. This facilitates carrier transport across the film due to the lack of grain

boundaries and is reflected in the carrier's mobility that is retained near their high frequency values over the 485 nm thick film. Defining the lower and upper bounds for the average carrier mobility ($\mu_\pm$) with the aid of our THz measurements allows us to calculate the individual electron and hole mobilities within these limits. The resulting mobilities are μ_p = 2.4 to 6 cm^2 V^{-1} s^{-1} and μ_n = 16 to 37 cm^2 V^{-1} s^{-1}, which corresponds to $\mu_\pm$ between 10 to 22 cm^2 V^{-1} s^{-1}. Our calculated mobilities are supported by theoretical calculations by Motta et al.[10] where they obtained comparable values of μ_p = 1 to 5 cm^2 V^{-1} s^{-1} and slightly lower values for μ_n = 5 to 10 cm^2 V^{-1} s^{-1}. We also find that the mobilities of electrons are $\approx$ 6 times larger than their positively charged counterparts. Our findings are in line with the observations of Ponseca et al. [11] that demonstrated μ_n / μ_p ratio of $\approx$ 2 and theoretical work by Umari et al. [12] using SOC-DFT that calculated higher effective masses for holes than electrons. These observations have implications for the design and fabrication of photovoltaic devices. Holes have a longer total transport distance to the HTM interface, due to photon absorption occurring in higher proximity to the SnO$_2$ interface. The combination of lower mobility and longer transport distances for the positive charge carriers means that there is an imbalance in the rate at which photogenerated electrons and holes arrive at their respective extracting interfaces and should be a consideration in device engineering. Inverted device architectures where holes are generated in higher proximity to their accepting interface or compositional engineering of the perovskites with the goal of enhancing hole mobilities are possible avenues to achieve balanced electron and hole transport to the acceptor interface.

5.3.4 Comparison of EA and TA spectra
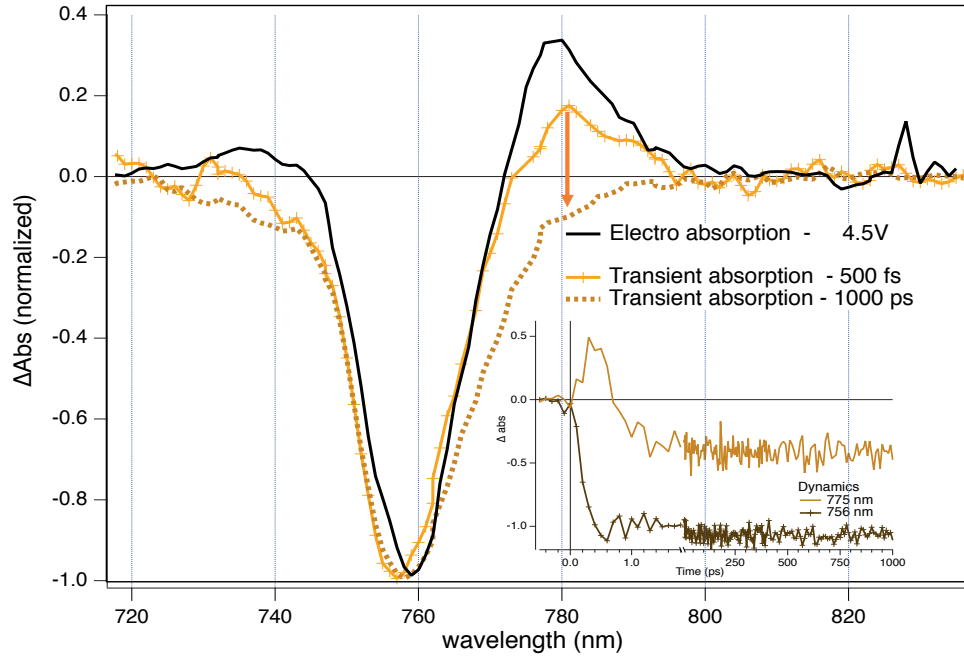
Figure 5.5 - Differential absorption spectra of perovskite solar cells. **Yellow curve (solid):** Transient absorbance (TA) spectrum at 500 fs after photo-excitation ($V = 0$ V, λ_{pump} = 600 nm, fluence = 0.4 μJ $\cdot$ cm^{-2}), **Yellow curve (dashed):** TA spectrum at 1000 ps after photo-excitation ($V = 0$ V, λ_{pump} = 600 nm, fluence = 0.4 μJ $\cdot$ cm^{-2}). **Black curve**: Electro-absorption (EA) spectrum ($V = 4.5$ V). **Inset**: TA dynamics monitored at λ_{probe} = 756 nm and 775 nm.

Our experimental setup also allowed us to carry out transient absorption (TA) measurements with the same sample configuration as the EDA measurements. The absorbance change (ΔA) for the TA measurements are defined by equation 4.1. TA measurements were carried out in specular reflectance mode, sequentially after EA and EDA measurements. Figure 5.5 shows that the TA spectrum at 500 fs has a shape that is similar to the steady state EA spectra under the application of a 4.5 V bias. At time delays > 800 fs, the positive absorbance change at 775 nm is not present anymore. On the contrary, one can observe a long lived bleaching at this wavelength that merges with the

ground state bleaching observed at 756 nm. Inset of Figure 5.5 compares the TA dynamics observed at 775 nm with the bleaching dynamics at 756 nm.

Our optical-pump THz probe measurements showed that subsequent to photoexcitation the early signal dynamics has a rise with a $t_{1/2} = 600$ fs. Since THz directly probes the formation of charge carriers, our dynamics could be associated with the formation of free charge carriers through dissociation of a bound exciton. We can extend our observations using THz spectroscopy to help in the analysis of our TA and EA spectra. In this situation, the disassociation of the neutral exciton results in an electric field between the electron and hole while they are in proximity. This field induces a shift in the absorption spectrum (electroabsorption) of the surrounding material that we are able to optically probe. The steady state EA spectra allow us to confirm that the spectral features we observe at $\approx$ 500 fs using TA can be attributed to an electroabsorption signal. Hence, by probing the features associated with the EA shift and the time for their onset in our TA measurements, we identify that exciton disassociation takes place within 500 fs and we converge on this value using three different spectroscopic techniques.

Trinh et al.[13] also observed such transient photoinduced EA features in their TA measurements of $CH_3NH_3PbI_3$ films. But they attributed their observations to the electric field created by hot carriers formed at photoexcitation, which affects the subsequent absorption of the material and results in a transient Stark shift. However, as we saw from THz measurements the rise in photoconductivity occurs with a $t_{1/2} = 600$ fs. This implies that free charge carriers are formed over this period and not directly after photoexcitation, so the observed EA can be associated with free carrier formation.

5.4   Conclusion

In conclusion, we carried out ultrafast time resolved electro-modulated absorption spectroscopy (TREAS) on mixed ion perovskites and this represents the first application of this technique to the investigation of complete perovskite photovoltaic devices. We observed electroabsorption in the devices under externally applied voltages as low as 1 V. The observed EA signal allowed investigation of the electric field screening dynamics by photogenerated charge carriers formed at a low excitation density of 3×10^{15} cm^{-3} for a range of voltages. The dynamics allowed us to directly visualize the motion of electrons and holes to the perovskite | acceptor interface. Combining THz and TREAS measurements we calculated the upper and lower bounds for each carrier's mobility - $\mu_p = 2.4$ to 6 $cm^2\,V^{-1}\,s^{-1}$ for holes and $\mu_n = 16$ to 37 $cm^2\,V^{-1}\,s^{-1}$ for electrons. The lower mobility and longer transport distances for the positive charge carriers means that there is an imbalance in the rate at which photogenerated electrons and holes arrive at their respective extracting interfaces and should be a consideration in device engineering. Transient absorption measurements revealed that the electric field between a free electron and hole exerted on the surrounding material produces an EA signature that is visible in the TA spectra. This was verified using steady state EA measurements that monitor the change in the absorption spectrum on the application of a field. THz measurements allowed us to conclude that these free charge carriers are formed through the dissociation of a transient excitonic species and this process has a $t_{1/2} = 500$ fs.
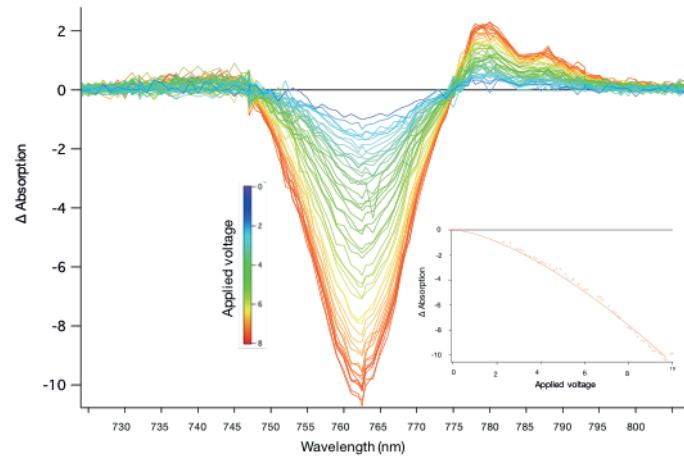
5.5   Appendix

Appendix 5.1
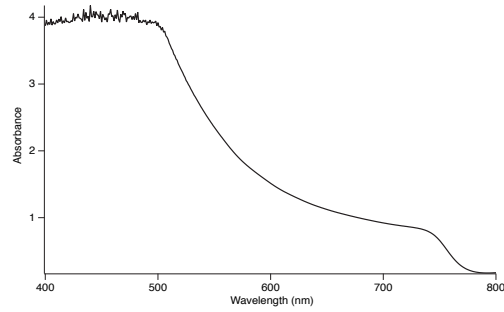
Figure A 5.1 – Absorption spectrum of the measured mixed perovskite film

Appendix 5.2

Figure A 5.2 - Steady-state electro-absorption (EA) spectra of the perovskite active layer in a mp-TiO$_2$ photovoltaic device for applied voltages ranging from 0 to 10 V. Inset: dependence of the differential absorbance measured at λ_{probe} = 762 nm upon application of an external electric field (E).

Appendix 5.3
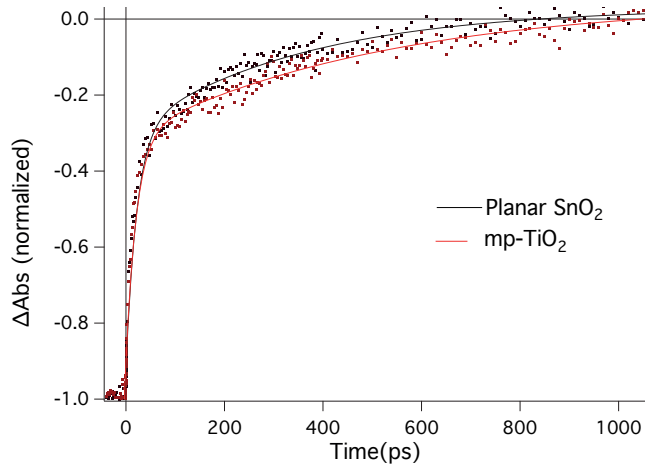
Figure A 5.3 - Time-dependence of the differential absorbance probed at the peak of the EA signal at for planar SnO_2 for mp-TiO_2 devices with λ_{probe} = 758 nm, pump *fluence* = 0.3μJ/cm^2 and submitted to an external electric field $E = 4.9 \times 10^4$ V·cm^{-1} (V_0 = 3.5 V).

5.6 Bibliography

1.   Baena, J. P. C. *et al.* Highly efficient planar perovskite solar cells through band alignment engineering. *Energy & Environmental Science* **8,** 2928–2934 (2015).

2.   Roiati, V. *et al.* Stark Effect in Perovskite/TiO2 Solar Cells: Evidence of Local Interfacial Order. *Nano Lett.* **14,** 2168–2174 (2014).

3.   Wu, X. *et al.* Composition-Dependent Light-Induced Dipole Moment Change in Organometal Halide Perovskites. *J. Phys. Chem. C* **119,** 1253–1259 (2015).

4.   Devižis, A. *et al.* Dissociation of Charge Transfer States and Carrier Separation in Bilayer Organic Solar Cells: A Time-Resolved Electroabsorption Spectroscopy Study. *Chemical Society* **137,** 8192–8198 (2015).

5.   Correa-Baena, J.-P. *et al.* Unbroken Perovskite: Interplay of Morphology, Electro-optical Properties, and Ionic Movement. *Adv. Mater. Weinheim* (2016). doi:10.1002/adma.201600624

6.   Zimmermann, P. D. H. in *Integrated Silicon Optoelectronics* **148,** 1–9 (Springer Berlin Heidelberg, 2009).

7.   Devižis, A., Hertel, D., Meerholz, K., Gulbinas, V. & Moser, J. E. Time-independent, high electron mobility in thin $PC_{61}BM$ films: Relevance to organic photovoltaics. *Organic Electronics* **15,** 3729–3734 (2014).

8.   Lin, Q., Armin, A., Nagiri, R. C. R., Burn, P. L. & Meredith, P. Electro-optics of perovskite solar cells. *Nature Photonics* **9,** 106–112 (2015).

9.   Cadelano, M. *et al.* in *Perovskite Materials - Synthesis, Characterisation, Properties, and Applications* 1–24 (InTech, 2016). doi:10.5772/61282

10.   Motta, C., El-Mellouhi, F. & Sanvito, S. Charge carrier mobility in hybrid halide perovskites. *Sci Rep* **5,** 12746 (2015).

11.   Ponseca, C. S. J. & Sundström, V. Revealing the ultrafast charge carrier dynamics in organo metal halide perovskite solar cell materials using time resolved THz spectroscopy. *Nanoscale* **8,** 6249–6257 (2016).

12.   Umari, P., Mosconi, E. & De Angelis, F. Relativistic GW calculations on $CH_3NH_3PbI_3$ and $CH_3NH_3SnI_3$ Perovskites for Solar Cell Applications. *Sci Rep* **4,**

4467 (2014).

13. Trinh, M. T., Wu, X., Niesner, D. & Zhu, X.-Y. Many-body interactions in photo-excited lead iodide perovskite. *Journal of Materials Chemistry A* **3,** 9285–9290 (2015).

6. Conclusion and outlook

Over the course of this thesis we investigated two compositions of hybrid organic-inorganic perovskites, $MAPbI_3$ and the mixed perovskite - $(FAPbI_3)_{0.85}(MAPbBr_3)_{0.15}$. The primary spectroscopic techniques used were time-resolved THz spectroscopy and time-resolved electroabsorption spectroscopy (TREAS). They served as powerful tools in revealing the short and long range transport properties of charge carriers, as well as their formation and recombination dynamics subsequent to photoexcitation.

In **chapter 3** we employed time-resolved THz spectroscopy towards the goal of understanding the fundamental process that occur after the photogeneration of charge carriers. By monitoring the rise in photoconductivity of the perovskite film, we observe the formation of free charge carriers through the dissociation of an excitonic species, the process occurring with a $t_{1/2} = 600$ fs. The high frequency THz mobilities of our $MAPbI_3$ films were determined to be 41 ± 3 cm^2 V^{-1} s^{-1} and 22 ± 4 cm^2 V^{-1} s^{-1} for the mixed perovskite sample. As the next step, we controlled the charge carrier density within the film by modulating the pump excitation fluence and monitored the photoconductivity dynamics between $1 - 1000$ ps. Combining the experimental results from the two perovskite films with distinct morphologies and compositions, we explain our observations using a band model that is composed of a direct as well as an indirect transition. At low excitation densities, carriers occupy and recombine from bands which are offset in k space. The resulting indirect transition is momentum forbidden and hence the carriers are long-lived. At higher excitation densities, carriers are divided between this indirect band and bands which overlap in k space, recombination through this direct

transition occurs more rapidly in ≈ 1 ns with the remaining carrier population being that of the indirect band.

Importantly, we observe that the mixed perovskites have an η_{onset} value for bimolecular recombination that is an order of magnitude larger than their $MAPbI_3$ counterparts. We experimentally show that alloying $MAPbI_3$ increases the carrier population that can be sustained prior to the onset of the fast direct band recombination. The ability to support large densities of carriers is a fundamental requirement for photovoltaic devices and we show that in the mixed perovskites, the η_{onset} values are comfortably away from the typical carrier densities experienced under operational conditions. Our observations provide direction for future work that focuses on compositional engineering to increase η_{onset} as a route towards improved device performance.

We also observed vibrational modes in the dark permittivity spectra. Further investigations that systematically vary the halide and cation composition can provide valuable information on the specific vibration modes that are visible over our accessible THz range. The insights gained can be combined with investigations of the conductivity spectrum and related to the photoinduced modulation of such modes.

Chapters 4 and **5** detail the first application of time-resolved electroabsorption spectroscopy to perovskite thin films and state-of-the-art photovoltaic devices. These measurements allowed us to visualize the evolution of carrier's mobility as they drift across the perovskite films. We see that the morphologies of the films play a large role in determining the effective macroscale charge carrier mobility. In our $MAPbI_3$ films we observe that the film is composed of small grains, with average dimensions of 40nm. This

results in photogenerated carriers having to traverse a large number of grain boundaries, diminishing the effective carrier mobility by a factor ≈ 4, relative to the high frequency mobility measured using THz spectroscopy. We also observed spectral signatures associated with carrier accumulation at the perovskite | acceptor interface. This leads to future work investigating the efficiency of carrier extraction at different electron and hole transport interfaces.

An electroabsorption signature in our transient absorption measurements was attributed to the electrostatic interaction between an electron and hole that shifts the absorption spectrum of the surrounding material. By optically probing this EA feature, we determine the dissociation of an exciton and subsequent formation of free carriers occurs $\approx 500\text{fs}$ after photoexcitation. Finally, we studied complete perovskite photovoltaic cells using TREAS. In the perovskite layer formed using the mixed composition, we identified that the average grain size is of comparable length to the film thickness. This facilitates the transport of electrons and holes to their acceptor interfaces and we observe that carriers retain their mobilities near their high frequency values. We are able to disentangle the contributions of the electrons and holes to the field screening dynamics and estimate electron mobilities between 16 to 37 $\text{cm}^2\,\text{V}^{-1}\,\text{s}^{-1}$ and hole mobilities between 2.4 to 6 $\text{cm}^2\,\text{V}^{-1}\,\text{s}^{-1}$. These results provide an approach to separately visualize the transport of electrons and holes in complete photovoltaic devices. Future work should investigate carrier transport properties of alternative compositions that have been engineered for higher hole mobilities or inverted device architectures, where positive charge carriers are generated in higher proximity to their accepting interface.

Acknowledgements

I cannot properly thank the many people that helped me start and finish this thesis in the space of a few pages, but this work would not have been possible without their help over the last years and in these last pages I would like to express my gratitude in a few inadequate words.

Prof. Jacques-E Moser for giving me the opportunity to do my master project in the group and then continue with my PhD. He has always been a source of great ideas and projects, while giving me the freedom and autonomy to pursue these projects but always being there for discussions and help when there were problems, for all of this I would like to express my deepest gratitude. I would also like to thank Dr. Ahmad Oskouei for his supervision at the start of my thesis, for teaching me about the THz setup and always being a friendly presence in the lab. As well as Prof. Natalie Banerji who supervised my master project and was a continual source of motivation and knowledge throughout this period.

I would also like to thank all the people I had the chance work with and meet over the last few years. Marine, I will never understand how a single carrot can provide all the energy you have…Thank you for all the coffee and many, many other things. And Andres, thank you for sharing your collection of sweaters/jackets with us, my life would have been less interesting without it. Mariateresa, for all the interesting questions, discussions and comments. Dr. Andrius Devižis, for building the EDA setup and more importantly the spare bicycle parts. Mateusz for helping everyone not take life too seriously. Jöel for

Arun ABY PARAECATTIL

arun.aby@gmail.com

arun.aby.

EDUCATION AND TRAINING

Swiss Federal Institute of Technology at Lausanne (EPFL), Switzerland *Mar. 2013* **– present**
PhD candidate, Group of Photochemical Dynamics
Title: A Time-resolved Photophysical Study of Organic-Inorganic Perovskite Photovoltaic Materials

Swiss Confederation CTI – Business Concept Training (64 hours) *Sept. 2016* – Dec. 2016
Program on business project development and entrepreneurship for scientists.

Swiss Federal Institute of Technology at Lausanne (EPFL), Switzerland *Sept. 2011 – Feb. 2013*
M.Sc. in Molecular and Biological chemistry

University of Toronto, Canada *Sept. 2007 – July 2011*
Honors B.Sc. in Materials Science: Chemistry and Engineering
    Summer program: **University of Kassel, Germany** *June 2008 – Aug. 2008*
    Environmental Science and Cultural Studies

Bachelor thesis – (University of Toronto, Canada) *Sept. 2010 – July 2011*
Honors bachelor thesis, Sargent group
Title: Synthesis and Optical Characterization of Colloidal Nanoparticles for application in photovoltaics and biosensors.

St. Mary's, Dubai, United Arab Emirates *Sept. 1995 – July 2007*
Secondary school – British GCSE / A Levels

PUBLICATIONS

- A. Paraecattil, J. De Jonghe-Risse, V. Pranculis, J. Teuscher and J.-E. Moser. ***Dynamics of Photocarrier Separation in MAPbI₃ Perovskite Multigrain Films under a Quasistatic Electric Field***, in The Journal of Physical Chemistry C, vol. 120, num. 35, p. 19595-19602, 2016.
- J. C. Brauer, A. Marchioro, A. A. Paraecattil, A. A. Oskouei and J.-E. Moser. ***Dynamics of Interfacial Charge Transfer States and Carriers Separation in Dye-Sensitized Solar Cells: A Time-Resolved Terahertz Spectroscopy Study***, in The Journal of Physical Chemistry C, vol. 119, num. 47, p. 26266-26274, 2015.
- M. Scarongella, A. A. Paraecattil, E. Buchaca-Domingo, J. D. Douglas and S. Beaupré et al. ***The influence of microstructure on charge separation dynamics in organic bulk heterojunction materials for solar cell applications***, in Journal of Materials Chemistry A, vol. 2, p. 6218-6230, 2014.
- A. A. Paraecattil and N. Banerji. ***Charge Separation Pathways in a Highly Efficient Polymer:Fullerene Solar Cell Material***, in Journal of the American Chemical Society, vol. 136, num. 4, p. 1472–1482, 2014.

- A. A. Paraecattil, S. Beaupré, M. Leclerc, J.-E. Moser and N. Banerji. *Intensity Dependent Femtosecond Dynamics in a PBDTTPD-Based Solar Cell Material*, in The Journal of Physical Chemistry Letters, vol. 3, p. 2952-2958, 2012.
- A. Schaarschmidt, A. A. Farah, A. Aby, A. S. Helmy. **Influence of Non-Adiabatic Annealing on Morphology and Molecular Structure of PEDOT-PSS Films** in ACS J. Phys. Chem. B, vol. 113, 9352-9355 (2009)

Organized Conferences

Co-chair – Doctoral school in photonics (Gstaad, Switzerland)   *20 July 2016 – 27 July 2016*
Title: Perspectives on photonics: Investigating the route from materials to devices

TECHNICAL SKILLS

Matlab, Python, Igor pro, Labview (Core 1 & 2 Certification)

LANGUAGES

English – Native language
French – Intermediate Spoken (B1)
Malayalam – Native spoken